Models of Technological Polymers

A dissertation presented by

Nicola Molinari

to

The Department of Physics

in partial fulfilment of the requirements
for the degree of
Doctor of Philosophy.

Imperial College London

January 2018

Thesis advisors:
Dr. Arash A. Mostofi
Prof. Adrian P. Sutton FRS

Nicola Molinari

Models of Technological Polymers

Abstract

Polymers are widely adopted in many industrial sectors, where they usually constitute small but crucial technological components. In the oil and gas industry, polymer seals should act as impermeable barriers to protect sophisticated downhole equipment from corrosion. Additionally, their mechanical properties play an important role in communicating information from the bottom of the well to the surface. However, costly permeation-driven failures are observed. In the energy storage sector, polymers are promising candidates for safer electrolytes that do not suffer from safety issues related to leakage, shorting and combustible reactions. However, cation mobility in polymer-based electrolytes must be improved to attain commercial viability. Finally, nanoparticles have been recently suggested as universal and inexpensive polymer adhesives, possibly solving the century-old problem of adhering soft matter together. The common thread is that significant insight can be gained through a molecular-level understanding of the underlying mechanisms.

Using a molecular-simulation-based approach, I have investigated the trends in, and the fundamental drivers of, the properties of these three technology-relevant polymer systems. In the oil and gas industry, hydrogenated nitrile butadiene rubber is widely adopted, and I have developed and validated a molecular model for it based on the OPLS-AA force-field. I have also studied the mechanical properties of filled elastomers using a coarse-grained model, and have uncovered important connections between filler loading, polymer-fillers network, and the stress-strain response of the material. In battery technology, poly(ethylene)oxide/Li/bis(trifluoromethane)sulfonimide is a promising electrolyte system, and I have demonstrated the central role of the anion in coordinating lithium atoms and the appearance of asymmetrical cation/anion clusters. Finally, I have investigated the use of nanoparticles as universal glue by studying the effects on the stress-strain response of nanoparticles' size, nanoparticle-polymer interaction strength and density. The latter influences the organisation of the nanoparticles at the interface, which results in a non-monotonous mechanical reinforcement.

The research constituting this thesis is my own, and it was carried out at Imperial College London under the supervision of Dr. Arash A. Mostofi and Prof. Adrian P. Sutton. Wherever the work of other authors is referenced, it has been duly acknowledged and appropriately cited within the text.

The copyright of this thesis rests with the author and is made available under a Creative Commons Attribution Non-Commercial No Derivatives licence. Researchers are free to copy, distribute or transmit the thesis on the condition that they attribute it, that they do not use it for commercial purposes and that they do not alter, transform or build upon it. For any reuse or redistribution, researchers must make clear to others the licence terms of this work.

Nicola Molinari
London, January 2018

Contents

List of Figures 6

List of Tables 8

Acronyms 9

1 Introduction 13
1.1 Thesis outline . . . 20
1.2 Publications . . . 22

2 A Molecular Model for Hydrogenated Nitrile Butadiene Rubber 23
2.1 Introduction . . . 23
2.1.1 nitrile butadiene rubber (NBR) and hydrogenated nitrile butadiene rubber (HNBR) . . . 27
2.2 The model . . . 29
2.2.1 Inter- & intra-molecular interactions . . . 29
2.2.2 A model for NBR . . . 32
2.2.3 HNBR structure generation . . . 34
2.2.4 Equilibration . . . 39
2.2.5 Assumption of the HNBR model . . . 40
2.2.6 Computational details . . . 42
2.3 HNBR bulk properties . . . 47
2.3.1 Density . . . 48
2.3.2 Bulk modulus . . . 50
2.3.3 Glass transition temperature . . . 52
2.4 Summary . . . 58

3 Polymer Nanocomposites Reinforcement 60
3.1 Introduction . . . 60
3.2 The model . . . 62
3.2.1 Inter- and intra-molecular interactions . . . 63
3.2.2 Structure generation . . . 66
3.2.3 Further details . . . 68
3.3 Results & discussion . . . 73
3.3.1 Validation of the model . . . 73

3.3.2 Stress-strain response and filler volume fraction (FVF) 74
3.3.3 Polymer-filler network at equilibrium (0 % strain) 77
3.3.4 Coordination during straining 81
3.4 Summary 89

4 Nanoparticles as Universal Soft Matter Glue **91**
4.1 Introduction 91
4.2 The model 93
4.3 Results & Discussion 96
4.3.1 nanoparticles (NPs) profile 96
4.3.2 Polymer bead–NP interaction and NP size 99
4.3.3 High NPs concentrations 103
4.4 Summary 107

5 Li-Bis(trifluoromethane)sulfonimide in Poly(ethylene)oxide **109**
5.1 Introduction 110
5.1.1 Libis(trifluoromethane)sulfonimide (TFSI) and poly(ethylene)oxide (PEO) 113
5.2 The model 115
5.3 Results & Discussion 120
5.3.1 Concentration and coordination 120
5.3.2 Concentration and Mobility 125
5.3.3 Clustering 126
5.3.4 Modifications 130
5.4 Summary 133

6 Conclusions **135**
6.1 Future efforts 138

Bibliography **142**

Appendix A The optimised potential for liquid simulation - all atom (OPLS-AA) force-field **163**

Appendix B The PCFF+ functional form **166**

Appendix C Additional persistence maps **168**

Appendix D Re-use permissions **170**

List of Figures

1.0.1 General molecular dynamics (MD) workflow 19

2.1.1 Temperature and pressure of oil wells drilled between 2007 and 2010 . . 24
2.1.2 Mud-pulse telemetry 25
2.1.3 NBR monomers: acrylonitrile (ACN) and butadiene 28
2.1.4 General chemical structure of NBR 28
2.1.5 NBR and HNBR comparison on key attributes 29
2.2.1 OPLS-AA molecules used to derive NBR parameters 32
2.2.2 Chain packing into an amorphous structure. 34
2.2.3 HNBR saturation procedure workflow 37
2.2.4 Outcome of the saturation procedure 38
2.2.5 Butadiene isomers 41
2.2.6 Possible cross-links ignored 42
2.2.7 Parallel efficiency 47
2.3.1 HNBR density vs cross-link fraction 48
2.3.2 Example of the compression routine to compute the bulk modulus . . . 52
2.3.3 Example of pressure/volume curve for HNBR 53
2.3.4 HNBR bulk modulus vs cross-link fraction 54
2.3.5 Example volume-temperature plot to compute glass transition temperature (T_g) 56
2.3.6 HNBR T_g vs cross-link fraction 57

3.2.1 Bonded potential for coarse-grained (CG) model 64
3.2.2 truncated and shifted Lennard-Jones (TSLJ) potential for filler–filler interaction 65
3.2.3 Pre- and post-equilibration snapshots of a CG example structure 68
3.2.4 Range of fillers investigated and the relative FVF 71
3.2.5 $NTL_z\sigma_{xx}\sigma_{yy}$ ensemble 72
3.3.1 Qualitative different mechanical response for structures with different FVF 75
3.3.2 Reinforced mechanical response at low FVFs 76
3.3.3 Stress-strain response for three FVFs with qualitative different behaviour 77
3.3.4 Example of radial distribution functions (RDFs) at 27 % and 40 % FVF 78
3.3.5 Coordination families prevalence at different FVF 79
3.3.6 Evolution of the coordination family as a function of strain 82
3.3.7 Persistence at for all fillers for a 47 % FVF structure. 84

3.3.8 Averaged persistence at different FVFs as a function of straining. 85
3.3.9 Total beads coordinating a filler at different FVFs as a function of straining. 86
3.3.10 Stress at 10 % strain versus total filler coordination 87
3.3.11 Total bond energy at different FVFs versus strain 88

4.2.1 Preparation of the polymer with a filler-reinforced interface 94
4.2.2 Straining of a structure with filler-reinforced interface 95
4.3.1 NPs ($R_{NP} = 1\sigma$) and polymer beads density profiles along the z axis. . . 97
4.3.2 NPs ($R_{NP} = 4\sigma$) and polymer beads density profiles along the z axis. . . 98
4.3.3 Polymer chain loop in the polymer network 99
4.3.4 Stress-strain response for different polymer–NP interactions and NP radii 100
4.3.5 "Reinforcement phase diagram" 102
4.3.6 Interfacial reinforcement for different NPs densities 104
4.3.7 Total coordination and persistence for $R_{NP} = 4\sigma$ and $\varepsilon_{NP\text{-}bead} = 5$ . . . 106

5.1.1 Total emission (2015) in CO_2 equivalent 111
5.1.2 Sketch of rechargeable lithium-ion battery 113
5.1.3 Molecular structure of TFSI and PEO 114
5.2.1 Experimental vs computed Li conductivity for different salt concentrations 119
5.3.1 Example of lithium hopping matrix 121
5.3.2 Stable Li cage percentage contribution to total number of cages 122
5.3.3 Lithium oxygen coordination 123
5.3.4 Different possible Li cages at high salt concentrations 124
5.3.5 Unique PEO chains coordinating Li atoms 125
5.3.6 Li mobility for different coordination families 126
5.3.7 LiTFSI cluster analysis 128
5.3.8 Modifications to the structure and their implication on Li mobility . . . 131
5.3.9 Li-TFSI cluster analysis after charge modifications 133

6.1.1 Sketch of a star polymer 141

C.0.1 Persistence for each filler for the 47 % FVF structures 169

D.0.1 Publishing permission for chapter 2 170

List of Tables

2.1.1 ACN dependence of some NBR key properties 28
2.2.1 NBR and HNBR equilibration procedure. 40
2.2.2 Timestep and energy conservation 46
2.3.1 HNBR mass density at different temperatures 49

3.2.1 TSLJ parameters for bead-bead, bead-filler, and filler-filler interaction . . 65
3.2.2 CG equilibration routine 69

5.1.1 Specific energy density for different storage materials 112
5.2.1 Point charges assigned to the atoms constituting TFSI 116
5.2.2 Equilibration procedure for the Li-TFSI-PEO systems 117
5.3.1 Percentage appearance of small asymmetric clusters 129

A.0.1 OPLS-AA force-field atom types for NBR and HNBR 164
A.0.2 OPLS-AA force-field bond types for NBR and HNBR 164
A.0.3 OPLS-AA force-field angle types for NBR and HNBR 165
A.0.4 OPLS-AA force-field dihedral types for NBR and HNBR 165

Acronyms

NBR nitrile butadiene rubber, 4, 6, 8, 20, 22, 27–29, 31–35, 37, 39–41, 48–52, 54, 55, 57–59, 136, 138, 163–165

HNBR hydrogenated nitrile butadiene rubber, 4, 6, 8, 20, 22, 23, 27–32, 34, 35, 37–41, 46–59, 69, 74, 136, 138, 163–165

FVF filler volume fraction, 5–7, 20, 21, 60, 62, 70, 71, 73–90, 136, 137, 139, 169

NP nanoparticle, 5, 7, 15, 16, 20, 21, 60–62, 65–67, 91–93, 95–108, 137, 139–141

TFSI bis(trifluoromethane)sulfonimide, 5, 7, 8, 21, 109, 113–117, 119, 123–128, 130–134, 137, 138

PEO poly(ethylene)oxide, 5, 7, 8, 21, 109, 113–117, 120, 121, 123–125, 127, 130–132, 134, 137, 138

OPLS-AA optimised potential for liquid simulation - all atom, 5, 6, 8, 20, 31–33, 36, 47, 49, 58, 69, 136, 163–165

MD molecular dynamics, 6, 17–19, 21, 31–33, 39, 42, 46, 51, 58, 61, 62, 69, 71, 72, 91–94, 96–98, 104, 105, 107, 115, 116, 118, 120, 135–139

ACN acrylonitrile, 6, 8, 27, 28, 32–35, 40, 41, 48, 49, 51, 53–57

T_g glass transition temperature, 6, 20, 26, 30, 40, 52–58, 74, 136

CG coarse-grained, 6, 8, 20, 21, 30, 61, 62, 69, 91, 92, 107, 108, 135–137

TSLJ truncated and shifted Lennard-Jones, 6, 8, 63–66

RDF radial distribution function, 6, 77–79, 81, 82

PNC polymer nanocomposite, 13, 20, 61, 62, 77, 80, 89, 90

BCPM bi-directional communication and power module, 14, 25, 27

DFT density functional theory, 17, 18, 29–32, 135

vdW van der Waals, 17, 30, 50, 167

HPHT high-pressure and high-temperature (in the context of oil and gas wells), 23

COMPASS condensed-phase optimized molecular potentials for atomistic simulation studies, 31, 33, 34, 115

LJ Lennard-Jones, 31, 32, 36, 63, 64, 66, 80, 163

LAMMPS large-scale atomic/molecular massively parallel simulator, 39, 68, 69, 94, 115, 116

HPC high performance computing, 46

SATP standard ambient temperature and pressure (298 K and 0.1 MPa), 48

FENE finite extensible nonlinear elastic (potential), 63

To my mum.

Acknowledgements

The work presented in this dissertation as well as the personal and professional development I achieved during my PhD would not have been possible without the support and guidance of several people I consider important that now I want to acknowledge officially.

First and foremost, I am grateful to my supervisors, Arash Mostofi and Adrian Sutton. From the continuous and deep trust to the tough love required to improve my writing skills: your efforts and support have been, and will always be, greatly valued by me.

I thank Georgy Samsonidze, Jonathan Mailoa, and Eric Fadel from the Bosch research centre in Cambridge, MA, for treating me as a member of the team from day one. A particular thank you is for Boris Kozinsky: aside from the obvious direct impact you had on my development and future, despite your busy schedule, you always found the time to discuss and chat with me, and I found every conversation enlightening.

I am also grateful to Stefano Angioletti-Uberti, for the time you invested in our collaboration and in helping me as well as the laughs at the various Christmas parties, Grazie!

It would be remiss of me not to thank John Stevens, Jimmy Eason, David Curry, Helmut Benning, and Michael Gaither, at Baker Hughes, for their financial support, engagement, contributions, and stimulating conversations.

Finally, to my friends and family, thank you.

1

Introduction

Polymers are ubiquitous in our lives. Both manufactured and natural polymers owe their central importance in our society to the vast range of properties that they can exhibit [1, 2]. The corner stone of this variety resides in the immense freedom in the choice of number, type and arrangement of the monomers, the building blocks of polymers. Furthermore, the insertion of (nano-)particles dispersed within the polymer matrix extends the applicability of the so-called polymer nanocomposite (PNC) even further. A high surface-to-volume ratio of the inserted particles combined with the properties of the base polymer culminates in the ability to control properties ranging from flammability [3, 4], to erosion resistance [5, 6], stiffness [7–9], and glass transition temperature [10–12].

As a result, polymers have played a role of prime importance in numerous advancements in modern technology. For instance, in medical and biomedical applications, polymers such as poly(ethylene), poly(propylene), poly(sulfone), poly(tetrafluoroethylene), and many others have been adopted to supplement or entirely replace body parts such as hip, knee, breast and dental structures, as well as for drug delivery [13–16]. The energy and energy storage sectors readily embraced the potential of polymer science and leveraged it. Energy efficient and safe fuel cells [17–19], and organic photovoltaics [20–22] are momentous examples. Buildings as well as monuments of historical importance can be restored using fiber-reinforced

polymers [23–25]. A remarkable example is the restoration of *la Basilica di San Francesco d'Assisi* following the devastating 1997 earthquake in central Italy, proving polymers can also help us preserve our cultural heritage [26]. These, along with space [27, 28], agricultural [29, 30] and automotive [31, 32] applications, are just examples of the profound positive changes that polymers have brought to our society. The following three paragraphs report the specific areas of application of polymers in technology that are relevant to the work presented in this thesis in later chapters.

Gaskets, O-rings, hoses and other widespread sealing components are amongst the beneficiaries of the diversity of polymer science [33]. In the oil and gas industry, sensitive monitoring equipment requires protection from contamination by the variety of fluids found in downhole operations, and polymers play a key role in this. During excavation and extraction operations, temperature and pressure can reach 600 K and 200 MPa, respectively [34–36], and, under these conditions, two permeation-driven modes of failure are observed. First, the ingress, diffusion and desorption of gases through seals leads to the swelling of the polymer and the threat of corrosion of the monitoring apparatus. Second, the gases trapped inside the seals experience a relatively quick pressure reduction when resurfaced, leading to swelling, tearing and rupture, a process known as explosive decompression [37, 38]. During the time spent downhole, gases permeate into the seals and partially occupy the voids that characterise an amorphous rubber [39]. In addition, the mechanical properties of rubber seals are critical to the bi-directional communication and power module (BCPM) operations, where the polymer helps modulate the pulses of mud used to transfer information between the bottom of the well and the surface in the technology known as mud-pulse telemetry. Despite the low rate of data transfer [40], this communication system is vital to extraction operations since standard electronic solutions are unpracticable due to the harsh oil-well conditions as well as the additional infrastructure that would be required. Seal-related failures lead to costs beyond just the replacement cost since the entire operation has to be stopped and, therefore, they pose interesting and urgent technological challenges to oil and gas companies such as Baker Hughes[*] [41], the industrial sponsor of my PhD.

[*]Towards the end of my PhD (July 2017), Baker Hughes merged with the oil and gas business division of General Electric to create the second biggest oilfield services company after Schlumberger. They are now

Another important and widespread area of the application of polymers is the energy sector. Historically, polymers were first adopted in the energy sector thanks to their electric insulation properties, but from the middle of the last century, they started to be tailored to act as semiconductors or even metals in regard of electronic conduction [42–47]. More recently, ionic conductive polymers gained considerable interest in both academia and industry as, in conjunction with lithium salts dissolved in the polymer matrix, they are seen as attractive candidates to substitute conventional electrolytes in batteries [48, 49]. Lithium-ion batteries commonly adopted in portable electronics use liquid electrolytes that possess good ionic conductivity even at low temperatures [50, 51]. However, they suffer safety disadvantages such as risk of leakage, combustible reaction products at the interface with the electrodes, and internal shorting [52–58]. While the threat posed by liquid electrolytes is considered acceptable for small devices*, for larger batteries that are able to store 100 kW h, such as the one installed on the Tesla model S [59], the risk becomes unacceptable. Ceramic and glass materials are under investigation thanks to their safety and ionic conductivity in the range of 10^{-3} S cm^{-1} to 10^{-1} S cm^{-1} [60–62], however, they lack the mechanical properties to withstand the swelling of the electrodes under normal operational conditions [63]. Polymers address most of the safety concerns associated with large-scale and high-energy rechargeable batteries, but their ionic conductivity in a temperature range of −20 °C to 60 °C is currently insufficient [64]. Solid polymer electrolyte materials are therefore of high interest in both the academic and industrial world, and they are the focus of the Robert Bosch Research and Technology Center in Cambridge, MA, where I did my nine-month internship.

Finally, polymers are the primary adhesive choice for various materials mainly thanks to their low manufacturing costs and ability to adapt to different surface morphologies [65, 66]. On the other hand, gluing polymers together proves to be a more challenging task to tackle, which requires adhesives with complex and ad-hoc designs [67, 68]. Rose *et alia* showed that the ability of nanoparticles (NPs) to form

named “Baker Hughes, a GE company”.

*The risk is concrete, especially when deploying a high number of these batteries, for instance, as in the recent accident that happened to a product produced by a leading smartphone manufacturer.

multiple and reversible bonds with the polymer could result in a possible universal solution to the centuries-old problem of sticking soft matter together [69]. As this is a relatively recent development, there are open questions on the interplay of important parameters, such as NP size, NP-polymer strength of the interaction, and NP density. Very recently, Kim *et alia* reported a non-monotonous adhesion energy as a function of NP density, effectively hinting at the existence of an optimal density for mechanical reinforcement of the glued interface [70]. The potency of NPs as universal glue for polymers is the focus of the investigation performed in collaboration with Stefano Angioletti-Uberti from the Department of Materials at Imperial College London.

The many and varied technological challenges described above can be addressed with a so-called "top-down" approach. In such investigations, chemical and physical intuition along with experience are the principal guidances in the choice of alternative materials and material combinations. Whilst this approach has led to major breakthroughs throughout the history of human discoveries, it has some drawbacks. Firstly, there are costs and uncertainties associated with what is, essentially, a trial-and-error approach. The countless multitude of alternatives that translates into the widespread use of polymers in almost every aspect of human life is a double-edged sword, becoming a curse in the absence of insightful guidance. Secondly, some of the experiments required to verify hypotheses and innovative components might be, at best, impracticable, if not impossible. Real-world conditions, for instance those experienced by elastomer seals at the bottom of an oil well, are difficult to reproduce in a controlled manner in a laboratory, where the effect of a single variable at a time is investigated. This aggravates the first point since, in combination, they can result in prohibitively long, expensive and unreliable studies. Last but not least, lack of understanding. While from an industrial point of view this might not be a major disadvantage[*], as scientists it is our duty and pleasure to understand the deep and fundamental origin and implications of different choices, and not only the change that they bring to the properties of the materials.

The drawbacks of top-down investigations can be mitigated by bottom-up approaches, where the use of computer experiments can help us develop a

[*] The main objective is often to create a technologically-improved and cheaper component.

molecular-level understanding[*]. Furthermore, this approach enables the effect of parameters that would be impossible to control experimentally to be investigated, thus helping to provide mechanistic understanding and suggestions for new experiments. The majority of the limitations associated with bottom-up methodologies can be related back to size of the system under investigation. For instance, the nature of the interactions between atoms, whether of a gas molecule permeating through an elastomer seal or of a lithium atom diffusing in a polymer electrolyte, is governed by quantum mechanics, therefore, fundamental approximations such as density functional theory (DFT)[†] would be required to capture the physics of these problems. The polymer chains investigated in this work are composed of tens of thousands of atoms, have a shallow energy landscape, and posses an amorphous nature, making studies on their dynamics an insurmountable challenge to methods such as DFT[‡]. The amorphous nature translates to a lack of order in the structure, as opposed to crystalline materials. Methods such as DFT heavily rely on the symmetry features of the problem under investigation to reduce the computational burden. As a result, amorphous materials cannot be efficiently simulated, and large models would be required to capture the local structural differences that characterise polymers. Consequently, the number of atoms required in the simulation increases far beyond what is deemed computationally feasible for methods such as DFT. To further exacerbate the problem, polymers often possess an energy landscape with no well-defined energy minimum, but rather a large number of shallow minima, making the convergence of DFT calculation quite tricky.

Instead, I decided to utilise classical MD to provide a molecular-level understanding of the aforementioned polymer-related problems and to help ameliorate them[§]. From protein folding [80] to fluid dynamics [81], MD computer simulations are a powerful and

[*]Whilst a powerful tool, it is important to realise that computer experiments do not constitute the holy grail of polymer physics and, more generally, material science, as they should be interpreted as a complementary tool to experiments, which are and remain the ultimate judge.

[†]A DFT approach would still have limitations, for instance, the poor description of van der Waals (vdW) interactions, for which improvements based on non-local dispersion-corrected functionals [71, 72] and *post-hoc* correction to ordinary DFT [73–76] have only recently been developed.

[‡]It is worth clarifying that DFT only provides the energy landscape used to evolve the system over one timestep in so-called *ab initio* molecular dynamics (MD) simulations.

[§]In this thesis, I only briefly touch on technical details on the method as numerous excellent books are focused on the topic, for instance [77–79].

widely-used approach implemented with success in various fields of research.

First introduced by Fermi in 1955 [82], classical MD computer simulations are used to study the dynamics of interacting and classical many body systems. More specifically, the trajectories of the atoms are determined via integration of the Newton's classical equations of motion

$$\vec{f}_i = m_i \frac{\partial^2 \vec{r}_i}{\partial t^2}, \tag{1.1}$$

$$\vec{f}_i = -\frac{\partial}{\partial \vec{r}_i} \mathcal{U}, \tag{1.2}$$

where i is a particle having mass m_i, position $\vec{r}_i$, and subject to the force $\vec{f}_i$. $\mathcal{U}$ refers to the potential energy, which is normally a function of all the atoms in the system, $\mathcal{U} = \mathcal{U}(\vec{r}^N)$, where N is the total number of atoms. Both the scientific and computational challenges of the method are hidden in $\mathcal{U}$. For the former, the accuracy of the results obtained heavily rely on how faithfully $\mathcal{U}$ reproduces the real energy landscape of the system. For the latter, the complex nature of $\mathcal{U}$ prohibits an analytical solution to the equations of motion, forcing the use of algorithmic integrators. The general workflow of classical molecular dynamics is presented in Figure 1.0.1. In classical MD, the interatomic interactions among atoms are described with "force-fields", which are approximated analytical formulations of the potential energy surface fitted to information obtained from a combination of ab initio methods such as DFT, normally for the terms involving chemical bonds, and experiments. The knowledge of electrons is lost in favour of static values for charges*, equilibrium distance for bonds, etc, effectively sacrificing accuracy† in exchange for the ability to simulate processes that would otherwise be impossible to investigate. Within the realm of force-fields there exist different levels of approximation‡, from all-atoms where every single atom in the system has its own set of parameters, to multiple levels of coarse graining. The choice is made depending on the application and

*In fact, efforts have been spent in trying to partially relax this constraint by introducing so-called polarisable force-fields [83].

†And also physics. For instance, a common analytical approximation for the bond term is a second order polynomial, hence, by stretching the bond the energy of it keeps increasing without resulting in bond breaking.

‡With different levels of sophistication of the analytical form of the interactions.

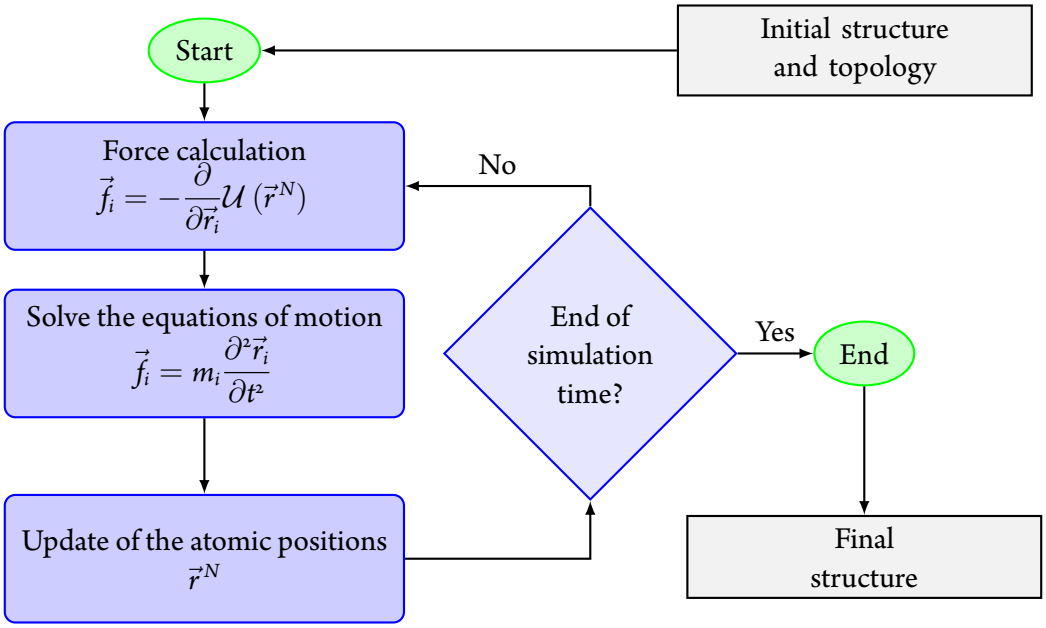


Figure 1.0.1: General structure of a MD computer simulation.

properties of interest, since, for example, grouping together chemical residues such as CH_n (n ranging from 1 to 4) as in [84] results in less computationally costly simulations at the expenses of the accuracy of the model. Moreover, even all-atoms force-fields very rarely are parametrised to the specific molecule under investigation, instead, more commonly they are parametrised to a class of compounds sharing similar chemistry. As a result, the use of off the shelf force-fields requires care, in particular, the transferability of the parameters should be verified by comparing computed properties to experiment.

Ultimately, I believe it is important to realise that no method comes without compromises. From the experiences I have been exposed to throughout my PhD, I think every approach has its own unique weaknesses and strengths, and it is vital to realise this in order to perform meaningful science. In my work, I try to adopt the method I deem to be the most suited to the investigation I want to perform.

1.1 Thesis outline

My PhD work has been motivated by developing atomistic and coarse-grained (CG) models of polymers that have specific applications in technology, and obtaining physically-based mechanistic understanding of their properties to help with the furtherance of these technologies. The three main applications that have been the focus of my interest are, superficially, very varied: elastomers for seals used in the oil & gas industry; polymer electrolytes for Li-ion batteries; and NPs as universal polymer glue. The underlying scientific approach to understanding behaviour and molecular mechanisms in technological polymers via computer simulation is the same and provides the unifying thread through this thesis.

In chapter 2, I develop a chemically-inspired molecular model for one of the most commonly-used elastomers in the oil and gas field, hydrogenated nitrile butadiene rubber (HNBR). The model has tunable cross-link density, it is obtained via a procedure that mimics the real process to produce HNBR starting from its unsaturated predecessor, nitrile butadiene rubber (NBR)[*], and the atomic interactions are described using the optimised potential for liquid simulation - all atom (OPLS-AA) force-field. I test the atomistic description of HNBR by computing bulk properties, namely mass density, bulk modulus and glass transition temperature (T_g), and comparing the obtained values to experiments.

Since polymers are often reinforced with the inclusion of nanoparticles within their matrix to enhance their mechanical, rheological and chemical properties, in chapter 3 I investigate the mechanical response of PNC at different filler volume fractions (FVFs) using coarse-grained molecular dynamics computer simulations. The sacrifice in terms of chemical accuracy of the polymer model allows me to overcome the length- and time-scale limitations associated with an all-atom description of a filled polymer. I observe that different filler loadings lead to qualitatively different stress-strain responses of the PNC to uniaxial strain. In particular, going from structures with low to high filler volume fraction (FVF): firstly, a yield drop appears in the stress-strain curve; then, as the FVF increases further, there is a reduction in plastic hardening; finally, at still higher filler

[*] The NBR model was previously developed and tested by Khawaja [85].

loadings, failure via necking occurs. I demonstrate that this behaviour is the result of the network formed by the polymer chains and filler particles, which is composed of three distinct types of local polymer-filler molecular structure motifs. The relative prevalence of these three motifs in the filled elastomer strongly depends on the FVF of the polymer and from the level of straining. Furthermore, the observed qualitative changes in the mechanical response can be understood microscopically in terms of changes in the relative population of the three motifs.

In chapter 4, the CG model described in chapter 3 is revisited with the aim to study the potential of spherical particles, which can be interpreted as NPs, as universal adhesives for polymer melts. With the use of MD simulations, I shine light onto the interplay of three key properties, namely NP size, NP-polymer interaction strength, and NP density. The main result shows a non-monotonous strengthening of the stress-strain response depending on the NP size and concentration at the interface. Furthermore, the findings are in good qualitative agreement with a simple analytical model of the melt adhesive energy that has been developed.

In chapter 5, I model the solid amorphous polymer electrolyte system comprising poly(ethylene)oxide (PEO), lithium, and bis(trifluoromethane)sulfonimide (TFSI) anion, exploring effects of high salt concentrations relevant for battery applications. By studying the ions' distribution and transport, I shine light onto the significant effect that salt concentration has on ion mobility. I observe a previously undetected ensemble of Li-TFSI clusters emerging, where lithium ions have significantly lower oxygen atom coordination by the PEO polymer, and this results in their significantly lower mobility compared to the fraction of cations coordinated by the polymer. I report the remarkable tendency for cation-anion clusters to be asymmetrical, in other words, with the anions in greater number than Li cations, which may contribute to the low transference number of this material.

Ultimately, in chapter 6, I summarise the main findings and results, followed by considerations on how to fruitfully extend my work.

1.2 Publications

To date, my work has been patented, published, submitted for publication, or is in the final stages for submission as follows:

- "Molecular Model for HNBR with Tunable Cross-Link Density", **N. Molinari**, M. Khawaja, A. P. Sutton and A. A. Mostofi. J. Phys. Chem. B, 2016, 120 (49), pp 12700–12707[*†]. This constitutes part of chapter 2.
- "Insights on the microscopic origin of polymer nanocomposites reinforcement.", **N. Molinari**, A. P. Sutton and A. A. Mostofi. (In preparation). This constitutes part of chapter 3.
- "Effect of High Salt Concentration on Ion Clustering and Transport in Polymer Solid Electrolytes: a Molecular Dynamics Study of PEO-LiTFSI.", **N. Molinari**, J. P. Mailoa and B. Kozinsky. (Submitted). This constitutes part of chapter 5.
- "Nanoparticles Organization Controls Their Potency as Universal Glues for Gels.", **N. Molinari** and S. Angioletti-Uberti. (Submitted). This constitutes part of chapter 4.
- (Patent) "Substituted Imidazole Lithium Salts.", J. Yang, H. B. Eitouni, M. Azagarsamy, B. Kozinsky, G. Samsonidze, and **N. Molinari**. Docket Numbers SE-092US and SE-092PCT.
- "Effects of solvent-salt charge-transfer complexes on oxidative stability of Li-ion battery electrolytes.". E. R. Fadel, F. Faglioni, B. V. Merinov, W. A. Goddard III, B. Kozinsky, G. Samsonidze, **N. Molinari** and J. P. Mailoa. (In preparation).

[*] http://pubs.acs.org/doi/abs/10.1021%2Facs.jpcb.6b07841

[†] Since this is a collaborative publication, it is worth clarifying the attribution of the work. The entire work on HNBR is done by myself as are all the results presented in chapter 2. The HNBR model has been built on the shoulders of the NBR model developed and validated by Khawaja. In chapter 2, I make comparisons between the two elastomers and wherever this is done I duly highlight that the NBR results are obtained by Khawaja.

2

A Molecular Model for Hydrogenated Nitrile Butadiene Rubber

Nitrile rubbers are widely used in the oil and gas field as elastomer seals, however, permeation of chemicals undermines their efficacy as impermeable membranes. Molecular simulations can be used to understand the fundamental origins of these effects, but a suitable model, able to capture all the relevant degrees of freedom, has to be developed first. This chapter introduces a chemically inspired, fully atomistic description of the widely-adopted hydrogenated nitrile butadiene rubber (HNBR) elastomer and assess its performance by computing mass density, bulk modulus and glass transition temperature as a function of the cross-link density in the structure.

2.1 Introduction

The first appearance of a drilled oil well can be traced back to nearly 2000 years ago, where bamboo pipes were used in China to create wells up to a depth of 200 m [86]. Whilst the technology used has much progressed, the overall principles remain the same nowadays. Present day oil wells can be required to reach far greater depths, pushing the materials challenges to the extreme. An example of the environmental conditions to be expected is shown in Figure 2.1.1, which presents the summary of the oil wells drilled between 2007 and 2010 as a function of temperature and pressure [35]. High-pressure high-temperature

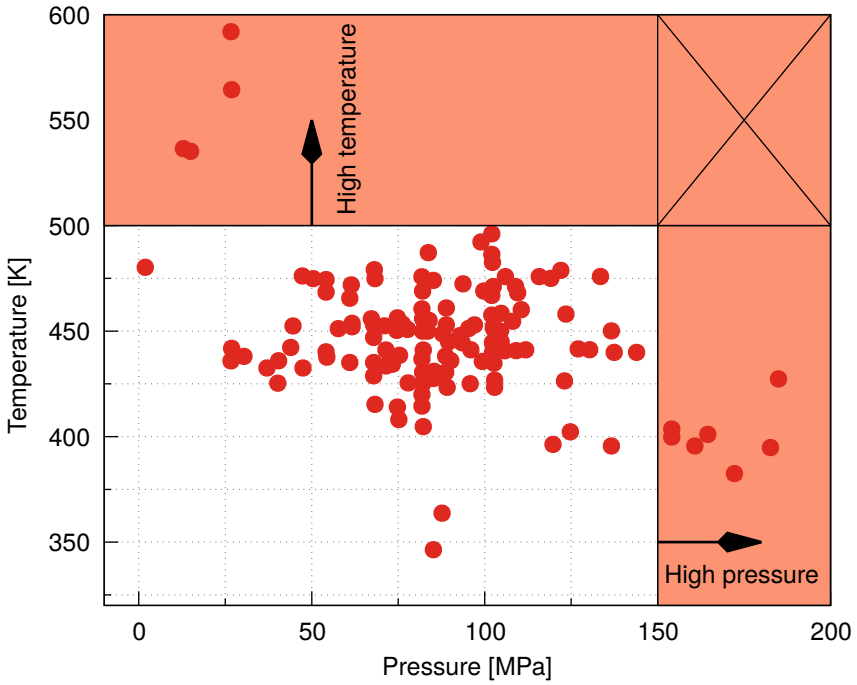


Figure 2.1.1: Oil wells drilled between 2007 and 2010 worldwide as a function of the temperature and pressure of the installation. The data are taken from [35], and extracted with WebPlotDigitizer [87].

(HPHT) conditions, where temperature and pressure exceed 500 K and 150 MPa respectively, are rare, but not absent[*]. While the source of the high temperature is obvious[†], there are three main sources of high pressure inside a well: 1. lithostatic, or overburden, pressure – in other words, the stress that is imposed on a layer of soil by the weight of the overlying material; 2. hydrostatic pressure exercised by the overlying body of water, if any, and 3. the pressure from fluids such as the drilling mud[‡] and released hydrocarbons. On top of these static sources of pressure, the stress built up during the drilling process is relieved all at once when the rock is broken, leading to shocks as high as

[*] Also, most wells demonstrate either one or the other extreme condition, but not both.

[†] There are essentially two sources of heat: the geothermal gradient and the drilling process.

[‡] The drilling mud, or drilling fluid, is critical to the entire drilling process. Often made of a suspension of bentonite clay in water [88, 89], it is used to remove cuttings, lubricate and cool the cutting tools, and to create the so-called "mud cake", which is built up around the completed well to structurally consolidate the hole as well as to prevent contamination from other fluids [90, 91].

100 g [92], where g is the acceleration due to gravity.

During the drilling and extraction processes, there is the need for exchanging information between the equipment at the bottom of the well and the head of operation on the surface*. Standard hardwired electronics solutions are not practical due to the required number of special pipes and the harsh environmental condition under which the electronics components would have to operate. The so-called mud-pulse telemetry is the workaround to this problem. Pressure waves of drilling fluid are exchanged through the drilling pipe from the surface to the bi-directional communication and power module (BCPM) Figure 2.1.2. This ingenious solution is characterised by a low data transfer rate,

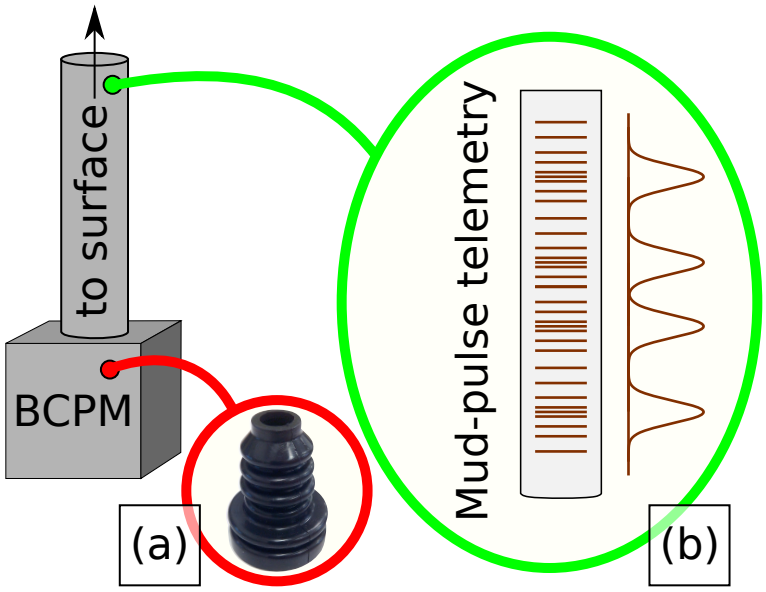


Figure 2.1.2: Pressure waves are sent along the drill pipe to the surface from the BCPM, where the elastomer seals, (a), plays a crucial role in creating the mud-pulses, (b). Image created with Inkscape 0.92.

around 10 bit/s [40], since the noise in the signal, sent through kilometres of fluid, is the limiting factor.

Critical to the BCPM operations are the elastomer† seals used to modulate the

*For instance, knowing the type of rock formation drilled can lead to the decision of altering the drilling direction with the scope to more efficiently reach the oil reservoir.

†The terms elastomer and rubber are interchangeable [93].

mud-pulse and to protect the module from the ingress of fluids, which would undermine its reliability. An elastomer is a loosely cross-linked polymer above its glass transition temperature (T_g) [94]. A key characteristic of any type of elastomer is a highly elastic behaviour [95]. The driving factor of this elasticity is entropy. In other words, there is a purely entropic negative tension, proportional to the stretching of the chain, that tries to bring the polymer chain back to a state with a higher number of possible configurations [95]. A simple demonstration of this can be derived from the ideal, or Gaussian, model for polymer chains. Fixing one end of the polymer chain to the origin of the Cartesian axis, in the limit of long chains the probability of finding the other end at a distance r is [96]

$$P(r) \propto \exp\left[-\frac{3r^2}{2Nb^2}\right], \tag{2.1}$$

where N is the total number of bonds of length b, and the proportionality constant accounts for the normalisation to one of the probability. Let $\Omega(r)$ be the total number of possible configurations of the ideal chain when the free end is at a distance r, then [97]

$$\Omega(r) \propto \exp\left[-\frac{3r^2}{2Nb^2}\right]. \tag{2.2}$$

Using the Boltzmann relation, the configurational entropy is

$$S = k_B \ln \Omega, \tag{2.3}$$

$$\propto -\frac{3k_B}{2Nb^2} r^2 + \text{constant}, \tag{2.4}$$

Where k_B is the Boltzmann constant. Hence, the free energy F at a temperature T is

$$F = U - TS, \tag{2.5}$$

$$\propto U + \frac{3k_B T}{2Nb^2} r^2 + \text{constant}. \tag{2.6}$$

At constant internal energy U, the tension acting on the chain, f, is

$$f = -\frac{\partial F}{\partial r} \tag{2.7}$$

$$= -\frac{3k_B T}{Nb^2} r. \tag{2.8}$$

It is worth stressing that this result is obtained at constant internal energy U. In other words, a stretched polymer chains experience a purely entropic restoration force, which tries to bring the polymer back to a state where more possible configurations, and hence higher entropy, are available [95]. This characteristic property makes elastomers invaluable for sealing applications, since they can adapt to the changes in the surroundings. Baker Hughes reported failures in the BCPM component that can be traced back to the swelling and/or lack of impermeability to fluids of the nitrile butadiene rubber (NBR) and HNBR elastomer seals. This failure mechanism costs millions of dollars from repairs and the loss from the stopped extraction operations, and it constitutes the motivation underlying this work. NBR and HNBR are now introduced before the modelling approach is described in section 2.2.

2.1.1 NBR and HNBR

Over the decades since its first synthesis in 1930 [98], NBR has been widely adopted for applications ranging from aeronautic and automotive to oil industries [99–103] The latter is of particular interest for this work, where its resistance to fuels [104–106] makes NBR a key candidate material for seals and grommets. From the polymerisation process between acrylonitrile (ACN) and butadiene, see Figure 2.1.3, the statistical copolymer* known as NBR is obtained, Figure 2.1.4. Various properties of the resulting elastomer are governed by the ratio between the two monomers in the chain once the polymerisation is completed, Table 2.1.1.

The hydrogenated version of NBR, or HNBR, is often the elastomer of choice in oil

*A polymer is called statistical if the distribution, or sequence, of its building blocks, or monomers, follows statistical laws. Note that to be called a true random polymer, the probability of finding a given monomer at a given point in the chain is flat, or, in other words, equal to the mole fraction of that monomer in the polymerisation chamber [107].



Figure 2.1.3: Monomers used in the polymerisation process that leads to NBR.

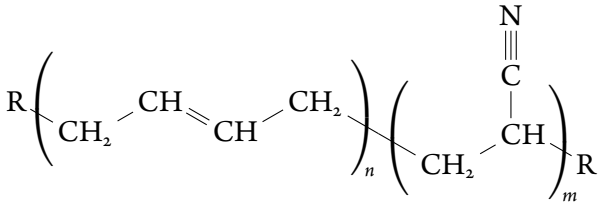


Figure 2.1.4: General chemical structure of an NBR chain after polymerisation.

Low ACN	Property	High ACN
	Hardness	$\longrightarrow$
	Tensile strength	$\longrightarrow$
	Abrasion resistance	$\longrightarrow$
	Heat resistance	$\longrightarrow$
	Oil/fuel Resistance	$\longrightarrow$
	Air/gas Impermeability	$\longrightarrow$
$\longleftarrow$	Resilience	
$\longleftarrow$	Low temperature flexibility	

Table 2.1.1: Dependency on the ACN grade of some key NBR properties [104, 105].

wells where relatively harsh environments characterise the installations. The catalyst-driven process that hydrogenates NBR results in a controlled saturation of the carbon-carbon double bonds present on the NBR backbone, Figure 2.1.4. HNBR inherits the NBR properties that make the latter an important elastomer for oil and gas applications, such as oil resistance and low temperature flexibility. In addition, the hydrogenated elastomer has enhanced resistance to heat, blistering, amine corrosion, and elongation to fracture compared to its unsaturated precursor [99, 100, 108]. A summary

of how HNBR and NBR compare on these properties is presented in Figure 2.1.5 (data from [99]).

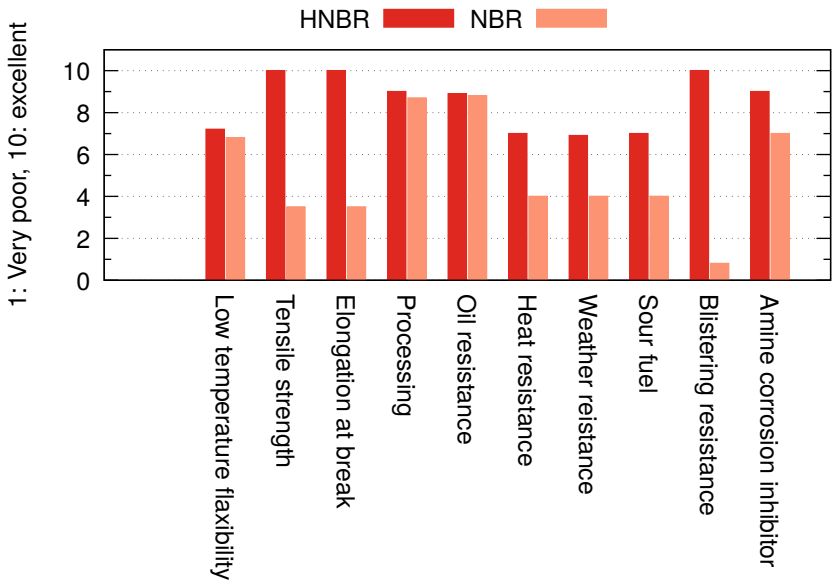


Figure 2.1.5: Comparison between NBR and HNBR on some key properties. The data are taken from [99].

2.2 The model

2.2.1 Inter- & intra-molecular interactions

Quantum-mechanical techniques such as density functional theory (DFT), which are able to capture the full electronic structure of HNBR, would prove ideal for describing the inter- and intra-molecular interactions of the polymer. In the literature, DFT has been successfully exploited to compute interaction energies between hydrocarbons and NBR * polymer chains up to three monomers long [109, 110]. The extension of such studies to a

*The HNBR precursor

number of monomers, temperatures and pressures more representative of real-world applications would prove computationally impractical. As a result properties such as mass density, T_g and bulk modulus are out of reach of DFT-based investigations. Furthermore, DFT is known to struggle to properly describe van der Waals (vdW) interactions [*] that are of central importance in holding the polymer together.

Consequently, approximations must be made to overcome the typical limitations imposed by a quantum-mechanical approach. When interested in the dynamics of a system the required simplification is often fulfilled with the implementation of a so-called force-field. This, slightly misleading, name refers to the description of the potential energy surface of the system that gives forces once its gradient is computed. Different levels of approximation are achieved by choosing different analytical formulations of the potential energy surface. For instance, Kremer and Grest proposed a bead-spring model where entire monomers are grouped into single beads connected via non-Hookean springs [111, 112]. Alternatively a finer description could be achieved with so-called united-atom models where "super atoms" with effective interactions are used to coarse-grain chemical residues such as CH_n (n ranging from 1 to 4) as in [84][†]. Finally, an all-atom approach describes every atoms in the system and their degrees of freedom, such as partial charges, 2(,3,4) body bonded interactions and non-bonded terms. In general, chemical specificity is progressively lost with coarser parametrisations but with the advantage of accessing greater length- and time-scales. It is important to recognise the relative strengths and weaknesses of each approach and choose a force-field accordingly. The ultimate goal of the HNBR model presented in this chapter is to investigate the solubility and diffusivity of small gases [‡], where chemical accuracy is required [120]; hence a fully atomistic approach is chosen.

There exist a variety of all-atom force-fields and care must be exercised in the selection of a particular one. To the best of my knowledge, no fully-atomistic HNBR

[*] This topic is of high interest in the DFT community and improvements have been made, see [71–76]

[†] It is worth highlighting that there is not a unique "correct" way of reducing the number of degrees of freedom of a specific system. Coordinates of the centres of the super atoms as well as the type and parameters of the effective interactions among them can vary greatly even when trying to coarse-grain the same chemistry. An example of this is given by the seven different coarse-grained (CG) models developed for polystyrene [113–118], with different merit depending on the application of interest [119].

[‡] Such as CO_2 and H_2O [85]

model is reported in the literature, however, previous fully-atomistic molecular dynamics (MD) simulations can be found on its precursor, NBR [121–124]. The vast majority implement the proprietary condensed-phase optimized molecular potentials for atomistic simulation studies (COMPASS) force-field [125] from Materials Studio [126]. Its commercial nature [*] results in the parameters being hidden in an encrypted database and therefore inaccessible even to a licensed end-user. Choosing the COMPASS force-field therefore has two major implications. First, comparison and tweaking of parameters becomes virtually impossible. Second, all simulations and a good portion of the analysis must be performed within the Materials Studio suite, which makes debugging difficult and limits what we can do to what is implemented in the software. For these reasons, I agree with the choice of the freely-available optimised potential for liquid simulation - all atom (OPLS-AA) force-field [†][127] made by Khawaja, a former member of the Mostofi group, for his NBR model [85]. Furthermore, having access to Khawaja's work means I can mimic the industrial process by which HNBR is obtained from hydrogenation of its precursor.

Full details on the analytic formulation of the OPLS-AA potential energy as well as the parameters used for NBR and HNBR can be found in Appendix A. In summary, the contributions to the total potential energy are split into two categories: bonded and non-bonded interactions, given in Equations 2.9, 2.10 and 2.11.

$$E = E_{\text{bonded}} + E_{\text{non-bonded}}, \tag{2.9}$$

$$E_{\text{bonded}} = E_{\text{bond}} + E_{\text{angle}} + E_{\text{dihedral}} + E_{\text{improper}}, \tag{2.10}$$

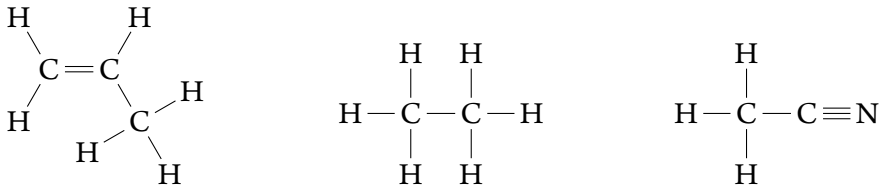
$$E_{\text{non-bonded}} = E_{\text{LJ}} + E_{\text{Coulomb}}. \tag{2.11}$$

The definitions of these terms can be found in Appendix A. DFT calculations on small molecules are used to parametrise the bonded terms. The parametrisation is performed by applying small distortions to the DFT geometry optimised structures, computing the non-equilibrium energy and fitting the functional form to the so-obtained energy

[*] The COMPASS force-field is in constant evolution thanks to the addition of new parameters over time. Some of the oldest versions are freely available, however, they lack completeness in the parameter space.

[†] The OPLS-AA force-field was initially developed in the 1990s and it is currently widely used in the polymer community thanks to the clarity of its formulation and completeness of parameters.

landscape*. Harmonic springs are used for bond lengths and angles, while a four-term harmonic expansion is used to map the dihedral angles. Due to the aforementioned DFT limitations, to parametrise the LJs and partial charges (non-bonded terms), MD calculations on bulk properties, such as mass density and heat of evaporation [127], are performed and the result fitted to experiment. For the NBR model used to derive the HNBR structure, the OPLS-AA parameters for ethane and propene are used for butadiene while acetonitrile is used to parametrise ACN, Figure 2.2.1. Therefore, bonded



(a) Propene **(b)** Ethane **(c)** Acetonitrile

Figure 2.2.1: Small molecules from which the parameters for NBR are taken. The first two are used to parametrise the butadiene monomer while the last is used for the ACN monomer.

terms spanning the two NBR monomers are not available within the OPLS-AA force-field and a sensitivity analysis on the missing parameters must be performed. While full details on the missing bonded terms can be found in Khawaja's PhD dissertation [85], in summary, the analysis showed differences in the mass density of less than 1 % when varying the missing dihedral parameters. The missing torsional terms are therefore set to zero.

2.2.2 A model for NBR

The HNBR model presented in this chapter is obtained via cross-linking and hydrogenation of Khawaja's NBR model. Here a summary of the general idea used to generate the NBR initial structure is presented – see [85] for a full discussion. While previous NBR simulations have not gone beyond a total of 164 monomers [121–124], it is experimentally known that a more representative polymer chain should be between

*To clarify, the parametrisation of the force-field is not performed by myself, and full details on the parameters used can be found in Appendix A.

400 to 20 000 monomers [128]. With the aim to maintain a balance between performance and a realistic model, a single chain comprising 1000 monomers is used*. The ordering choice of the monomers, and therefore also the post-polymerisation ratio between the two NBR monomers, is governed by the ACN and butadiene reactivity ratios [85]. While a higher ACN fraction is beneficial for many properties, in particular oil/fuel resistance and air/gas impermeability, Table 2.1.1, NBR ceases to be useful as an elastomer beyond 50 % ACN content due to the increase in its elastic modulus [129]. Once the sequence of monomers is stochastically determined, the next step is to choose the coordinates of each atom in the system. Liquids and short-chain polymer molecules possess fast relaxation times, meaning that the influence of the initial choice of atomic positions on the dynamics is minimal. The same is not true for long and amorphous polymers, where entanglement plays a central role in chain relaxation, which is governed by the snake-like movement known as reptation [96, 130]. Furthermore, the high degree of entanglement prevents the polymer from undergoing substantial conformational changes during typical MD simulation times. As a result, it is important to average the MD-computed properties over an ensemble of independently generated structures, especially the ones that show high sensitivity to free volume, such as solubility [131].

The 1000 NBR monomers are packed into a periodic cell using the rotational isomeric state method as implemented in the Amorphous Cell routine of Materials Studio [126]† and originally developed by Theodorou and Suter [132]. Figure 2.2.2 illustrates a sketch of the Monte Carlo routine adopted. Bond lengths and angles are fixed due to their stiffness and the chain is grown one backbone bond at a time once the first three backbone atoms are placed randomly in the cell. By varying the torsional angle, the energies of different potential next-atom sites are computed using the COMPASS‡

*The precise number of atoms depends on the ratio between the two NBR monomers. An approximate estimation is around 9000 atoms.

†Version 7.0

‡The reader might wonder why OPLS-AA was not used at this stage. Materials Studio does not allow the use of force-fields not included within the standard internal library, effectively forcing the use of COMPASS for the NBR amorphous cell generation. The rotational isomeric state method as implemented in the Amorphous Cell routine of BIOVIA (Materials Studio) is optimised for performances and reliability. Therefore it was used. However, care is required since the rest of the simulations are performed with OPLS-AA. It is worth highlighting that the only degrees of freedom in the outlined structure generation are the torsional angles that are derived from ab initio simulations for both OPLS-AA and COMPASS. Therefore, the same

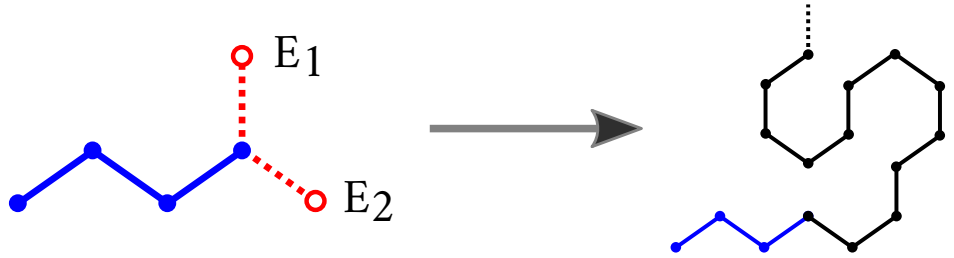


Figure 2.2.2: Sketch of the chain packing into an amorphous structure. Once the first three backbone atoms are placed randomly in the cell, all the others are grown one bond at a time keeping bonds and angles fixed and varying the torsional angle. The energy of different configurations is computed, E_1 and E_2 in the sketch, and a choice is made using a standard Metropolis-Hastings Monte Carlo selection criterion. To compute the energy cost of each configuration the COMPASS force-field is used. When all the backbone atoms are placed, the system is mapped back to the fully atomistic structure.

force-field and the choice is made with a standard Metropolis-Hastings Monte Carlo criteria based on the energies of the configurations. Once the entire backbone of the chain has been placed, the system is mapped back to the fully atomistic picture. Each configuration is first brought close to equilibrium following the procedure outlined in subsection 2.2.4 before the cross-linking and hydrogenation routine to generate HNBR from NBR is applied.

2.2.3 HNBR structure generation

To generate an HNBR structure, a single NBR chain comprising 1000 monomers, 39 % ACN content, and equilibrated (following the routine in subsection 2.2.4) is first produced via the procedure described above. Carbon atoms contributing to a carbon-carbon double bond are stochastically selected for cross-linking with a likelihood depending on a user-defined cross-link probability. If not cross-linked, the atom (and the other carbon atom taking part to the same double bond) is hydrogenated. The net result is that no carbon-carbon double bonds are present in the HNBR structure once the

dihedral energy landscape should be obtained effectively making the structure generation independent of the specific force-field adopted [133].

procedure is finished resulting in a 100 % saturated elastomer[*]. At this stage the polymer is re-equilibrated following the routine in subsection 2.2.4.

This method is applied to a frozen NBR structure, meaning no relaxation is performed between the applied structural modifications[†]. Similar static cross-linking methods have been used across the literature on different polymers (for instance [135–137]). However, I was the first to apply this technique to HNBR [133].

All the carbon atoms in a carbon-carbon double bond are put into a list, which is then shuffled[‡]. The actual procedure is primarily controlled by the cross-linking probability, p_{CL}, and the distance within which a cross-link partner has to be found, r_{CL}, that in turns determines a probability to find such partner, p_r. The user-defined p_{CL} determines the likelihood for a given sp^2[§] carbon atom to be chosen as a potential cross-linking site as opposed to being hydrogenated (with a probability $1 - p_{CL}$) during the saturation procedure. The total number of sp^2 carbon atoms depends on the ACN content since the carbon-carbon double bond is only present in the butadiene monomer. For this study the ACN content is fixed at 39 %, hence the list contains $1000 \cdot (1 - 0.39) \cdot 2 = 1220$ carbon atoms (N_{sp^2}). The value for r_{CL} is set to 0.5 nm to avoid the presence of chain segments between the two cross-linking candidates and at the same time to prevent unnecessarily overstretched bonds. The sp^2 carbon list is read one carbon atom at a time, and for each carbon atom a random number R_n is generated from a uniform distribution in the range $(0, 1]$. This leads to two possible scenarios.

1. $R_n > p_{CL}$. Both the selected carbon atom and its sp^2 carbon-carbon double bond partner are hydrogenated, and they are removed from the sp^2 carbon list. During

[*] The 100 % saturation obtained with my model is well justified by commercial HNBR formulations where total saturation is desirable for chemical inertness [134].

[†] An extension, based on this work, to take into account relaxation after every cross-link/hydrogenation step (dynamical cross-linking) has been tested by Khawaja [85]. The computed properties, that include mass density and cross-linked bonds length distribution, did not show significant differences between the static and dynamical method [133]. The static approach, however, is significantly more computationally efficient.

[‡] The idea behind the shuffling is to avoid biases in determining a cross-link partner. The list is originally ordered according to sequence of carbon atoms along the polymer backbone. Shuffling the list removes the possibility of cross-linking neighbouring atoms.

[§] A carbon atom participating in a carbon-carbon double bond.

hydrogenation, a hydrogen is placed randomly* on a sphere of radius 0.109 nm† centred on the carbon atom to saturate. All the force-field information has to be amended according to the change, i.e., the carbon atoms are converted to sp^3 carbons, and the bonded (bonds, angles and dihedral angles) and non bonded (partial charges and LJ parameters) interactions updated. These operations reduce the number of sp^2 carbon atoms in the system by two.

2. $R_n \leq p_{CL}$. In this case a cross-link is attempted, but is not guaranteed, however. To successfully cross-link the carbon atom, another sp^2 atom, different from the one participating in the same carbon-carbon double bond, has to be found within r_{CL}. If one or more such candidates exist, the cross-linking takes place between the closest pair and hydrogenation is performed on the sp^2 carbon atoms of the corresponding double bonds. If no suitable cross-linking partner is found, the carbon atom is hydrogenated as described above. Similarly to the previous case, the force-field information is updated accordingly. If the cross-link is successful, however, the total number of sp^2 carbons in reduced by four.

The entire process is outlined in Figure 2.2.3. Furthermore, it is worth noting that the cross-link fraction, p_{CL}, is only indicative of the final cross-link fraction, n_{CL}, due to the probabilistic nature of the implemented method. The probability of finding a cross-link partner within distance r_{CL} is a function of the number density of sp^2 carbon atoms in the system, which decreases during the procedure. In other words, the fewer unsaturated carbon-carbon double bonds left in the system the harder it is to find a suitable cross-link partner for a sp^2 carbon selected as a potential cross-link site. Effectively, there are two conditions that have to be met in order for cross-linking to happen, but while the first (p_{CL}) remains constant, the second (p_r) decreases throughout the procedure. Since the hydrogenation and the cross-linking operations deplete a different number of sp^2 carbon atoms, asking for higher p_{CL} results in a lower $\bar{p}_r$ ($\bar{p}_r$ being the average of p_r during the

*The expectation is that the equilibration following the cross-linking procedure will correct for steric overlap.

†This distance corresponds to the OPLS-AA equilibrium distance for a C(sp^3)-H bond.

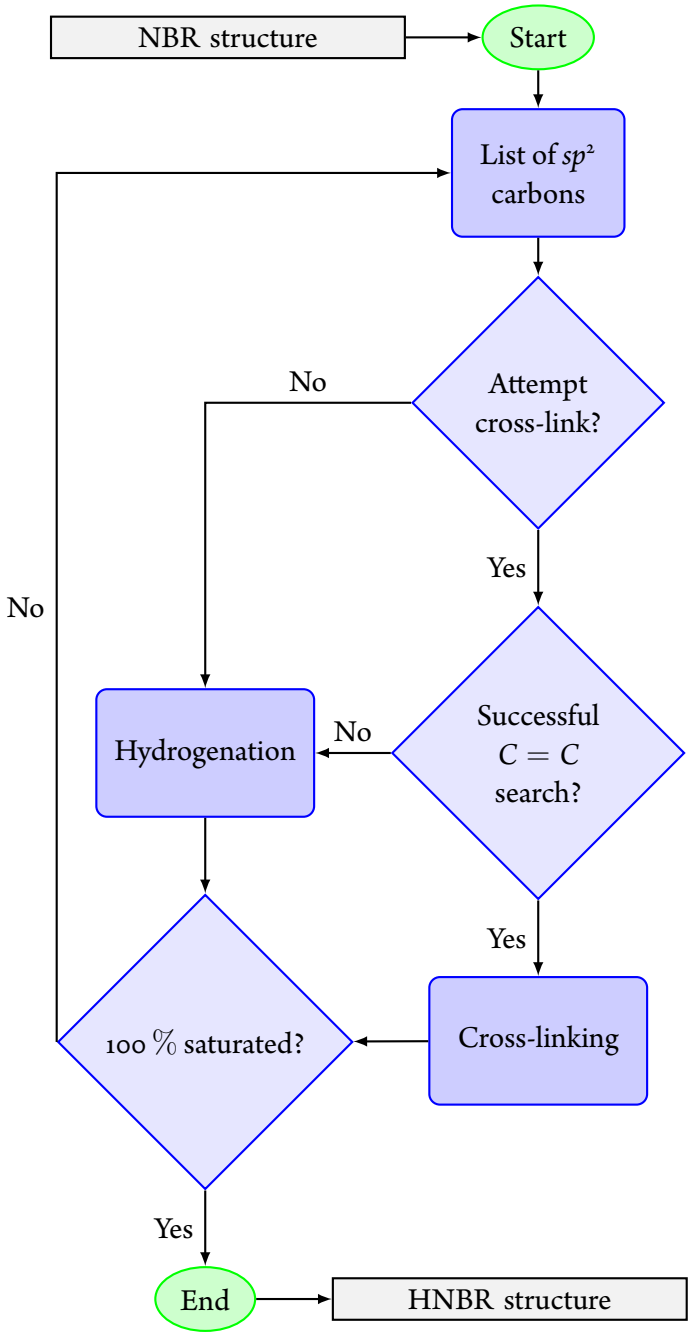


Figure 2.2.3: Static cross-link procedure to saturate NBR and obtain HNBR. The decision whether to attempt cross-linking or not is based on the user-defined cross-link probability while the search for a cross-link partner is performed within a distance of 0.5 nm from the carbon atom under investigation.

saturation procedure); see Equations 2.12, 2.13, 2.14 and 2.15.

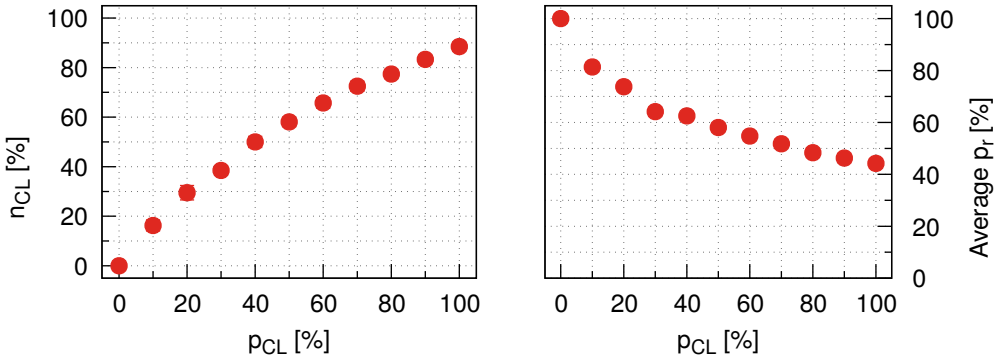
$$\text{Cross-linked carbon atoms} = 2 \cdot N_{sp^2} \cdot p_{CL} \cdot \bar{p}_r \tag{2.12}$$

$$n_{CL} = \frac{\text{Cross-linked carbon atoms}}{\text{Total } sp^2 \text{ carbon atoms}} \tag{2.13}$$

$$= \frac{2 \cdot N_{sp^2} \cdot p_{CL} \cdot \bar{p}_r}{N_{sp^2}} = 2 \cdot p_{CL} \cdot \bar{p}_r \tag{2.14}$$

$$\bar{p}_r = \frac{n_{CL}}{2 \cdot p_{CL}} \tag{2.15}$$

The true cross-link density, n_{CL}, and $\bar{p}_r$ as a function of the user-defined cross-link probability are presented in Figure 2.2.4. Note that $\bar{p}_r$ does not refer to the instantaneous



(a) n_{CL} vs p_{CL}.

(b) Average p_r vs p_{CL}.

Figure 2.2.4: True cross-link density, n_{CL}, and average of p_r during the saturation procedure as a function of the user-defined cross-link probability, p_{CL}. The data are the average results over an ensemble of eight independently generated structures. The standard deviations are also plotted, however, they are too small to be appreciated on the scale of this plot.

probability of finding a cross-link partner for a given sp^2 carbon atom, but to the average of that probability during the procedure. For this reason its value does not converge to zero in Figure 2.2.4. Once the initial structure is generated, the HNBR systems are equilibrated as described in the following section.

2.2.4 Equilibration

After both NBR and HNBR initial structure generations, an equilibration routine is necessary. For NBR, the Monte Carlo based structure generation quickly explores the immense phase space of the possible polymer configurations, while the equilibration explores the local phase space around the initial configurations. For HNBR, the cross-link procedure introduced non-equilibrium conformational changes, such as the added hydrogen atoms and the stretched cross-link bonds, and the relaxation is needed to correct such structural modifications.

The equilibration procedure comprises energy minimisation*, compression† and decompression, and annealing stages and it is broadly based on that used by Kucukpinar and Doruker used for their 164 monomer-long NBR simulations [121, 139]. The overall duration has been increased by over a factor of ten with the aim to reduce the spread of the mass densities [85]; the whole procedure is shown in Table 2.2.1 As the minimisation is performed with all the velocities set to zero, $\vec{v}^N = 0$, the velocities of all the atoms have to be reset after each minimisation. When doing so, the velocities are reset using a Maxwell-Boltzmann distribution, Equation 2.16, at the temperature T set to that of the stage following the minimisation.

$$P(|v_i|) = \sqrt{\left(\frac{m_i}{2\pi k_B T}\right)^3} 4\pi |v_i|^2 \exp\left[-\frac{m_i |v_i|^2}{2k_B T}\right]. \tag{2.16}$$

All the MD simulations are performed in the LAMMPS simulation package [140]; full details in subsection 2.2.6.

*The minimisation steps throughout this work used the FIRE algorithm [138] as implemented in the the large-scale atomic/molecular massively parallel simulator (LAMMPS) molecular dynamics package. The exit criteria for the minimisation are 1. energy fluctuations within 0.0001 % and 2. 50 000 steps, whichever occurs first.

†All the changes in pressure and temperature are performed at a constant rate over the time allocated at that specific stage.

Stage	Stage duration [ns]	Total time [ns]	Temperature [K]	Pressure [MPa]
Energy minimisation	-	-	-	-
NPT (compression)	0.25	0.25	298	0.1 → 500
NPT (decompression)	0.25	0.50	298	500 → 0.1
Energy minimisation	-	-	-	-
NPT (heating)	0.50	1.00	298 → 800	0.1
NPT (cooling)	0.50	1.50	800 → 298	0.1
NPT (compression)	0.25	1.75	298	0.1 → 500
NPT (decompression)	0.25	2.00	298	500 → 0.1
NVT	0.50	2.50	298	-
NPT	1.50	4.00	298	0.1

Table 2.2.1: Stages used to equilibrate NBR and HNBR initial structures.

2.2.5 Assumption of the HNBR model

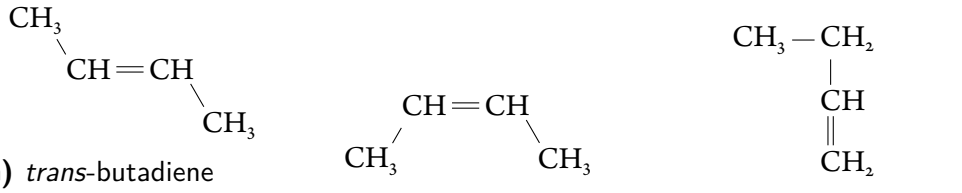
Butadiene isomers

This assumption originates from the NBR model. The butadiene monomer naturally occurs in three isomeric forms, two of which are ignored in the NBR initial structure generation. Out of the three isomers, shown in Figure 2.2.5, the *cis* and *vinyl* mole fractions are relatively small compared to the *trans*, which accounts for roughly 90 % of the total for NBR with 39 % ACN content [100]. Therefore only the *trans* form was used here.

Absence of fillers

With the general name of fillers I refer to particles, such as carbon black* and silica, which are normally inserted in the polymer matrix to tune material properties, and are a vital component of commercial elastomers. The wide range of tunable properties comprises elastic and bulk moduli [33, 34, 128], flammability [3, 4], erosion resistance [5, 6] as well as T_g [10–12]. The size of the filler particles can vary depending on the effect they are

*The name carbon black refers to amorphous carbon.



(a) *trans*-butadiene (90 %) **(b)** *cis*-butadiene (8 %) **(c)** *vinyl*-butadiene (2 %)

Figure 2.2.5: The butadiene isomers and their mole fractions that are found in NBR with 39 % ACN content [100]. While the entire work presented in this chapter is done at constant ACN content, it is worth highlighting that increasing the ACN fraction would lead to a decrease in the *cis* component while the *vinyl* stays constant [141].

meant to produce. For instance agglomerates of carbon black particles can range in size from 20 nm to 350 nm[*]. Such length-scales are quite prohibitive with a fully atomistic approach on current hardware. An ensemble of small filler particles immersed in a polymer might easily require a cubic simulation cell with 100 nm side length, which would translate to a simulation time 20 000 times longer than that of my current system[†].

A coarser description of the polymer is the widely-used workaround for this problem. However, it brings a loss of chemical specificity, at least partially. Whether to apply this technique or not depends on the particular objective of the work. For instance, in chapter 3 I am interested in the mechanical response of uniaxially strained elastomer nanocomposite, which required a distribution of fillers embedded in the polymer matrix, and hence a coarse-grained model based on the Kremer and Grest bead-spring model [111] is adopted. However, the ultimate goal of the HNBR model presented here is to study solubility and diffusion of small gases, for which a chemically-accurate approach is required [120]. Hence, filler particles are not included in this HNBR model[‡].

Cross-links Allowed

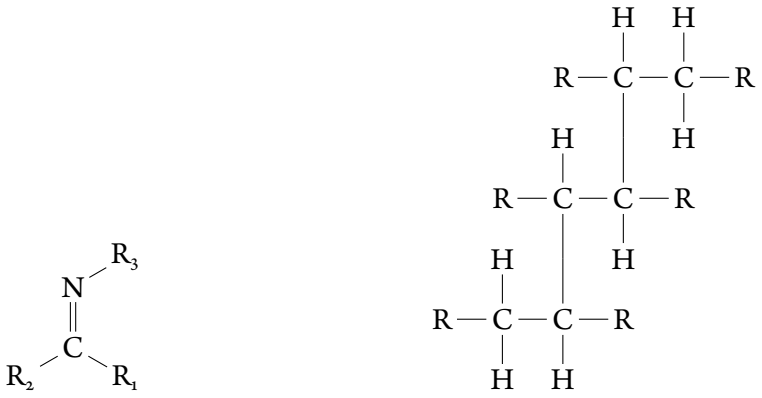
The procedure to obtain HNBR outlined in subsection 2.2.3 aims to saturate NBR while at the same time mimicking the peroxide-based curing process, which creates radical sites

[*] These boundaries are from the commercial formulations ASTM N_{110} and N_{990}, respectively.

[†] And this is applying perfect scaling. To put this into perspective, just the equilibration procedure would require 12 years.

[‡] The same is true for the NBR model [85].

that then covalently attach to one another [142]. In the saturation algorithm, only sp^2 carbon atoms can be cross-linked and only one cross-link per carbon-carbon double bond is allowed. While in principle not chemically impossible, other forms of covalent cross-linking such as the ones in Figure 2.2.6 are ignored in the present work.



(a) Imine **(b)** Multiple cross-links

Figure 2.2.6: Possible cross-links that are not included in the present work.

2.2.6 Computational details

By following the standard and most basic MD recipe outlined in chapter 1, the dynamics takes place in the so-called microcanonical ensemble, where the total number of particles N, volume V, and energy E^* are conserved. However, experiments in closed systems are complicated and rarely performed, and situations where temperature is controlled are more common. Such statistical ensemble is known as NVT, where the system can exchange energy with a heat bath kept at constant temperature T. Similarly, often the volume is required to fluctuate by controlling the pressure P of the system using a so-called isothermal-isobaric, or NPT ensemble. In MD these ensembles are obtained with the use of thermostats and barostats. A rescaling of the velocities of the particles is an unsophisticated method to control the temperature of the system. As the kinetic energy

*Due to the numerical integration of the equation of motion, in the actual implementation the energy conservation is never truly obtained, and an energy drift is expected.

of the system $\mathcal{K}$ is connected to temperature via the equipartition theorem

$$T = \frac{2\mathcal{K}}{3k_B N}, \tag{2.17}$$

the temperature of the system has the following time evolution

$$T(t) = \frac{\sum_{i=0}^{N} m_i \vec{v}_i(t) \cdot \vec{v}_i(t)}{3k_B N}, \tag{2.18}$$

and can be controlled by rescaling the velocities of the particles. This approach does not account for the presence of a heat bath typical of canonical ensembles and, moreover, does not guarantee the conservation of the total momentum as the velocities of the particles are constantly rescaled. To overcome these limitations, Nosé and Hoover [143, 144] modified the equations of motion by adding a term that explicitly model a thermal bath. The idea is to add a friction that slows or accelerate particles until the temperature of the system is equal to the desired value. The equations of motion are modified as follows

$$m_i \frac{\partial^2 \vec{r}_i}{\partial t^2} = \vec{f}_i - \zeta m_i \vec{v}_i, \tag{2.19}$$

$$\begin{aligned} \frac{\partial \zeta}{\partial t} &= \frac{1}{Q}\left[\sum_{i=1}^{N} \frac{1}{2} m_i \vec{v}_i(t) \cdot \vec{v}_i(t) - \frac{3N+1}{2} k_B T\right] \\ &= \frac{1}{Q}\left[\mathcal{K} - \frac{3Nk_B T}{2} - \frac{k_B T}{2}\right]. \end{aligned} \tag{2.20}$$

Notice the addition of the time evolution of the friction parameter ζ. The value of the parameter Q can be thought as an effective "heat bath mass". For instance, a high value of this mass results in a low coupling between the heat bath and the system.
In Equation 2.20, the extra $\frac{k_B T}{2}$ is due to the extra degree of freedom added by ζ. As required by the equipartition theorem, at equilibrium, i.e., $\frac{\partial \zeta}{\partial t} = 0$

$$\mathcal{K} = (3N+1)\frac{k_B T}{2}. \tag{2.21}$$

With the presence of a thermostat, the energy of the system is allowed to fluctuate, while it is the total energy (heat bath plus system) that is conserved. Similar considerations apply to the isothermal-isobaric ensemble, which allows volume fluctuation by controlling the pressure of the system. The second-order pressure tensor $\mathcal{P}$ can be computed according to the Clausius virial

$$\mathcal{P} = \frac{Nk_BT}{V} + \frac{1}{3V}\sum_{i<j}\vec{f}_{ij}\vec{r}_{ij}, \tag{2.22}$$

and the isotropic pressure P is defined as the trace of $\mathcal{P}$. The Nosé-Hoover barostat is based on the Andersen barostat, which mimics the action of a piston on the system [145, 146]. The Nosé-Hoover formulation for barostat and thermostat [143, 144, 146], as implemented in the LAMMPS code [140], is used throughout this dissertation to control pressure and temperature, respectively.

There exist several simulation algorithms able to evolve the equations of motion. The choice is a compromise between accuracy and efficient sampling of the phase space*. One of the widely-spread and most used method is a variation of the Verlet algorithm known as velocity-Verlet [147, 148]. For a particle i having mass m_i, position $\vec{r}_i$, velocity $\vec{v}_i$, and subject to the force $\vec{f}_i$, the evolution of such quantities after a timestep δt is

$$\vec{r}_i(t+\delta t) = \vec{r}_i(t) + \vec{v}_i(t)\delta t + \frac{1}{2m_i}\vec{f}_i(t)\delta t^2, \tag{2.23}$$

$$\vec{v}_i(t+\delta t/2) = \vec{v}_i(t) + \frac{1}{2m_i}\vec{f}_i(t)\delta t, \tag{2.24}$$

$$\vec{f}_i(t+\delta t) = -\frac{\partial}{\partial\vec{r}_i}\mathcal{U}\left(\vec{r}^N(t+\delta t)\right) \tag{2.25}$$

$$= \vec{f}_i(\vec{r}_i(t+\delta t)), \tag{2.26}$$

$$\vec{v}_i(t+\delta t) = \vec{v}_i(t+\delta t/2) + \frac{1}{2m_i}\vec{f}_i(t+\delta t)\delta t. \tag{2.27}$$

The velocity-Verlet algorithm, as implemented in LAMMPS [140], is used throughout

*As the latter is better achieved with greater timesteps, there is a bias towards low-order methods as they do not require the computation of high-order derivatives, which would significantly jeopardise the energy conservation for "large" timesteps.

this work to evolve the equations of motion.

It is clear from Equations 2.23, 2.24, 2.25 and 2.26 that the timestep δt plays a crucial role. The timestep used to integrate the equations of motion is a parameter that can help to sample the phase space more rapidly and save on computational expense. Any computer simulation should conserve the total energy of the system as Newton's equations of motion do. In fact, let $\mathcal{H}$ be the total energy of the system

$$\mathcal{H} = \mathcal{K} + \mathcal{U} = \sum_{i=1}^{N} \left[\mathcal{K}_i + \mathcal{U}\right]. \tag{2.28}$$

The time evolution of $\mathcal{H}$ is

$$\frac{\partial \mathcal{H}}{\partial t} = \frac{\partial}{\partial t} \sum_{i=1}^{N} \left[\frac{1}{2} m_i \left(\frac{\partial \vec{r}_i}{\partial t}\right)^2 + \mathcal{U}\right] \tag{2.29}$$

$$= \sum_{i=1}^{N} \left[m_i \frac{\partial \vec{r}_i}{\partial t} \frac{\partial^2 \vec{r}_i}{\partial t^2} + \frac{\partial}{\partial t} \frac{\partial \vec{r}_i}{\partial \vec{r}_i} \mathcal{U}\right] \tag{2.30}$$

$$= \sum_{i=1}^{N} \left[\frac{\partial \vec{r}_i}{\partial t} \left(m_i \frac{\partial^2 \vec{r}_i}{\partial t^2}\right) + \frac{\partial \vec{r}_i}{\partial t} \frac{\partial \mathcal{U}}{\partial \vec{r}_i}\right] \tag{2.31}$$

$$= \sum_{i=1}^{N} \left[\frac{\partial \vec{r}_i}{\partial t} \left(\vec{f}_i - \vec{f}_i\right)\right] = 0. \tag{2.32}$$

Hence Newtonian dynamics conserve the total energy $\mathcal{H}$. However, numerical approximations undermine this, see Table 2.2.2. For numerical stability as well as accuracy, the chosen timestep should be at least an order of magnitude smaller than the smallest timescale in the simulated systems*. For all-atom simulations the timescales needing extra care are usually found in the bond vibrations†. The smallest timescale in our system is the period of vibration of the carbon-hydrogen bond. It is estimated to be

*The appropriate timestep for a given simulation also depends on the integrator algorithm used since different integrators have different assumptions that need to be satisfied. Throughout my work I use the velocity-Verlet variation of the Verlet integrator [147, 148].

†Algorithms aimed to improve on this can be found in the literature. One of the most common approaches removes the fast C-H bond vibration by freezing it. The SHAKE algorithm [149] is an example of such methods.

Timestep [fs]	Total energy drift [$\%ns^{-1}$]	Relative speed-up
1.00	0.02(2)	1.00
1.25	0.03(0)	1.2(4)
1.50	0.07(2)	1.5(0)
1.75	0.1(4)	1.7(4)
2.00	0.7(2)	1.9(4)
2.25	Unstable	-

Table 2.2.2: Percentage change in total energy for different timesteps used to integrate the equation of motion. The values are averaged over five 0 % cross-linked HNBR structures runs with a NVE ensemble for a total of 2 000 000 timesteps (corresponding to 2 ns).

10^{-14} s = 10 fs[*]. For this work, a timestep of 1.50 fs is used for the equilibration procedure, while 1.00 fs is chosen to compute the bulk properties described in section 2.3.

Time- and length-scales are often the limiting factor in MD simulations[†] in the choice of which property to investigate and to what efficacy. Relatively cheap hardware has made the widespread use of high performance computing (HPC) facilities possible. However, it is important to understand how to make efficient use of the resources available. Improvements given by the use of multiple cores per simulation hit an efficiency plateau due to the overhead in communication necessary for particles crossing from the domain of one core to another. An example specific to my HNBR MD study is shown in Figure 2.2.7, which reports the number of CPU hours needed per nanosecond on two different node types as a function of the number of cores. Beyond eight cores, "A", the efficiency has already dropped significantly; doubling the number of cores to 16, "B", and doubling again to 32[‡], "C", does not lead to much improvement. Therefore, to increase the throughput while simulating a reasonable number of nanoseconds per day, in this work the MD simulations are performed using eight cores.

[*] A first approximation of the vibrational frequency can be estimated assuming the two masses connected via a Hookean spring.

[†] And, in fact, for basically all computational methods.

[‡] There are 16 cores per node and different nodes are interconnected with InfiniBand to minimise inter-node communication times.

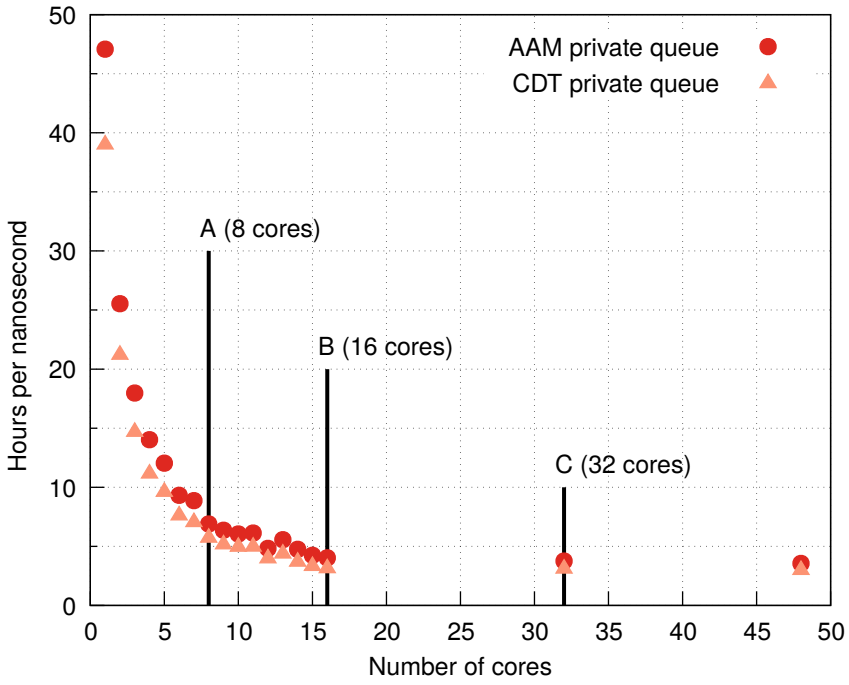


Figure 2.2.7: Hours per nanosecond obtainable on two different high performance computing queues as a function of different number of cores. The tested structure is a representative 0.0 % cross-linked HNBR structure (10 052 total atoms). The structure is simulated for 100 ps NPT (298 K and 0.1 MPa) with a timestep of 1.0 fs. The cores of the two queues belong to different generations and this explains the differences in the two curves.

2.3 HNBR BULK PROPERTIES

To demonstrate the applicability of the OPLS-AA force-field as well as to verify the proposed model, HNBR bulk properties are computed and presented here. Comparison to experiment is made wherever possible. However, there is a paucity of available experimental data. Most experimental results are in company data sheets, where fillers are normally included in the elastomer matrix*, making the comparison with this computational work challenging. Comparison is also made with the results obtained by

*Also, the exact filler composition is not known due to intellectual property reasons.

Khawaja on 41.3 % ACN content* and 0 % cross-linked NBR [85, 133].

2.3.1 Density

Figure 2.3.1 presents the standard ambient temperature and pressure (SATP) HNBR (39 % ACN content) density as a function of the cross-link fraction, as well as the density of NBR (41.3 % ACN content), the latter as computed by Khawaja [85, 133]. Once

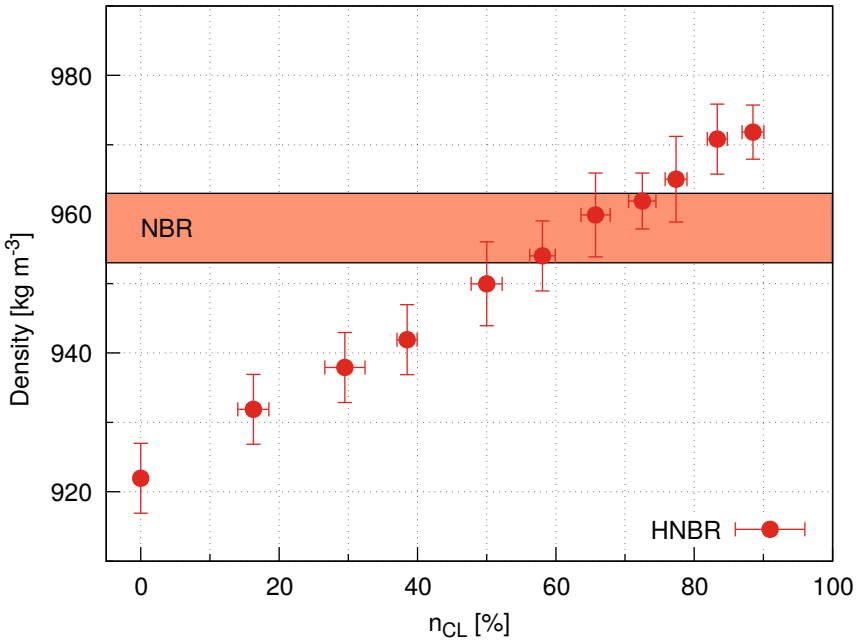


Figure 2.3.1: Computed densities for 39 % ACN content HNBR. The NBR has an ACN content of 41.3 %, its density was computed by Khawaja [85]. Temperature and pressure are fixed at 298 K and 0.1 MPa, respectively. The error bars (for HNBR) and the shaded area (for NBR) represent the standard deviation over eight independently generated structures.

equilibrated, each configuration is evolved for 2.0 ns at SATP within an NPT ensemble, and the density recorded every 0.2 ps to ensure sufficiently uncorrelated values. The final

*The small ACN content mismatch between HNBR (39 %) and NBR (41.3 %) produces small differences that can be ignored in the comparison of bulk properties between the two, especially since other sources of error play a major role.

numerical results reported are the ensemble average over eight independently generated configurations of the average mass density values across single trajectories. The volume of periodic and cubic box containing the uncross-linked structure is $99(1)$ nm^3, while for $n_{\mathrm{CL}} = 88(2)$ % is $93(1)$ nm^3. This values are ensemble averages over eight independently generated structure.

Focusing on the first point in Figure 2.3.1, the 0 % n_{CL} HNBR mass density is lower than the NBR one. Two effects contribute to this. First, the addition of hydrogen atoms in the structure increases the intra-chain separation due to their steric repulsion*. Second, carbon-carbon double bonds are replaced with less stiff and longer single bonds†. This observation is borne out by industrial data for HNBR before peroxide curing‡ as seen in Table 2.3.1, which also reports HNBR and NBR comparisons at different temperatures. The mass density prediction of the HNBR model agrees within 3 % with the industrial

		HNBR (39 % ACN, $n_{CL} = 0$)		NBR (41.3 % ACN, $n_{CL} = 0$)	
		this work	data sheet	Khawaja's [133]	experiment
ρ [kg/m^3]	250 K	940(4)	–	977(3)	–
	298 K	922(5)	950-960 [150, 151]	958(5)	1000 [152, 153]
	350 K	913(4)	–	942(3)	–

Table 2.3.1: Comparison of mass density with industrial data sheet for HNBR and to experimental work for NBR. All values are computed at 0.1 MPa.

value and, furthermore, the expected trend between NBR and HNBR is reproduced. Closer inspection reveals that both models consistently underestimate the experimental density values. The root of this problem probably lies in the low transferability of the ACN force-field parameters used, which would also explain the increasing discrepancy as a function of the ACN content observed in [85, 133]. The parameters from OPLS-AA used for ACN were in fact derived for acetonitrile and only extended to parametrise

*For instance, in the 39 % ACN content, 0 % cross-linked HNBR, all the 1220 sp^2 carbon atoms are saturated with hydrogen, meaning 1220 hydrogen atoms are added to the system.

†From the OPLS-AA parameters (see Appendix A), the carbon-carbon single bond is half as stiff and approximately 14 % longer than the carbon-carbon double bond.

‡Hence with a 0 % cross-link density.

polyacrylonitrile. For better agreement, parameters for polyacrylonitrile should be derived and used. However, such an effort was deemed to be beyond the scope of this work. Specifically for HNBR, commercial formulations in data sheets do not clearly provide a list of the type and quantity of additives contained in the polymer making direct comparison even harder.

On increasing n_{CL}, additional permanent covalent single carbon-carbon bonds replace vdW interactions. Moreover, more cross-links implies a smaller number of hydrogen atoms are added to the system, and an increase in the mass density is expected. This expectation is confirmed in Figure 2.3.1, which shows a clear trend of increasing mass density as a function of the cross-link density. A similar trend is expected based on the observations on other polymers ranging from polyurethane to nitroguar gum [154, 155]. Also, it is interesting that only HNBR heavily cross-linked can match the NBR (uncross-linked) mass density.

2.3.2 Bulk modulus

The isothermal incompressibility, also known as the bulk modulus, measures the volumetric response of a material to changes in pressure at constant temperature. At atmospheric temperatures and pressures, elastomers are often regarded as incompressible[*], however, re-evaluation of this statement must be made when considering elastomer seals used in oil and gas applications, where harsher conditions can easily be found at the bottom of a well.

A way to calculate the bulk modulus is to measure the volume of the system at different pressures and fitting the resulting $P(V)$ data to an equation of state, such as that

[*] Typical bulk modulus for an elastomer is in the order of 2 GPa, which translates to a change in density of roughly 0.02 % per atmospheric pressure.

of Birch-Murnaghan [156, 157] shown in Equation 2.33.

$$P(V) = \frac{3B_0}{2}\left[\left(\frac{V_0}{V}\right)^{7/3} - \left(\frac{V_0}{V}\right)^{5/3}\right]\left\{1 + \frac{3}{4}\left(B_0' - 4\right)\left[\left(\frac{V_0}{V}\right)^{2/3} - 1\right]\right\}, \quad (2.33)$$

$$B_0 = -V_0\left(\frac{\partial P}{\partial V}\right)_T, \quad (2.34)$$

$$B_0' = \left(\frac{\partial B_0}{\partial P}\right)_T. \quad (2.35)$$

Equation 2.33 defines the pressure, P, at a volume, V, in terms of three parameters defined at zero pressure: the bulk modulus, Equation 2.34, its derivative, Equation 2.35, and the reference volume V_0. This equation has been previously applied with success to NBR [85] as well as to various other polymer systems [158] and, therefore, it is used as equation of state for HNBR.

Using MD the P(V) data can be computed, which are then fitted to Equation 2.33. The HNBR equilibrated structures are alternately: 1. squeezed in an NPT ensemble at a constant rate of 2.5 MPa ps^{-1} for 0.4 ns and 2. run in an NPT ensemble at constant pressure for 0.3 ns. Figure 2.3.2 shows an example of the procedure. During the last 0.2 ns of the recording stage, the pressure and volume of the simulation cell are saved every 0.2 ps, and the averages and standard deviations extracted. This process is performed at constant temperature, 298 K. It is started at a pressure of 0.1 MPa and stopped at the final pressure of 1 GPa, for a total of 10 average pressures and volumes. Figure 2.3.3 shows an example of the set of $P(V)$ data as well as the resulting fit to obtain the bulk modulus.

Figure 2.3.4 shows the bulk modulus for HNBR (39 % ACN content and at 298 K) as a function of the cross-link density, n_{CL}. The final incompressibility value at a given n_{CL} is the average of eight independently generated HNBR structures, while the error bar represents the standard deviation amongst those. There is a clear trend of increasing bulk modulus for more cross-linked HNBR: the network deformation due to the applied pressure is constrained by the addition of covalent bonds. Moreover, this observation is borne out by similar trends in other polymer systems [155, 159, 160]. The bulk modulus falls in the range of 2 GPa to 4 GPa, which is the typical order of magnitude for the bulk modulus of polymers. For instance, in the literature the reported bulk modulus is 1.3 GPa

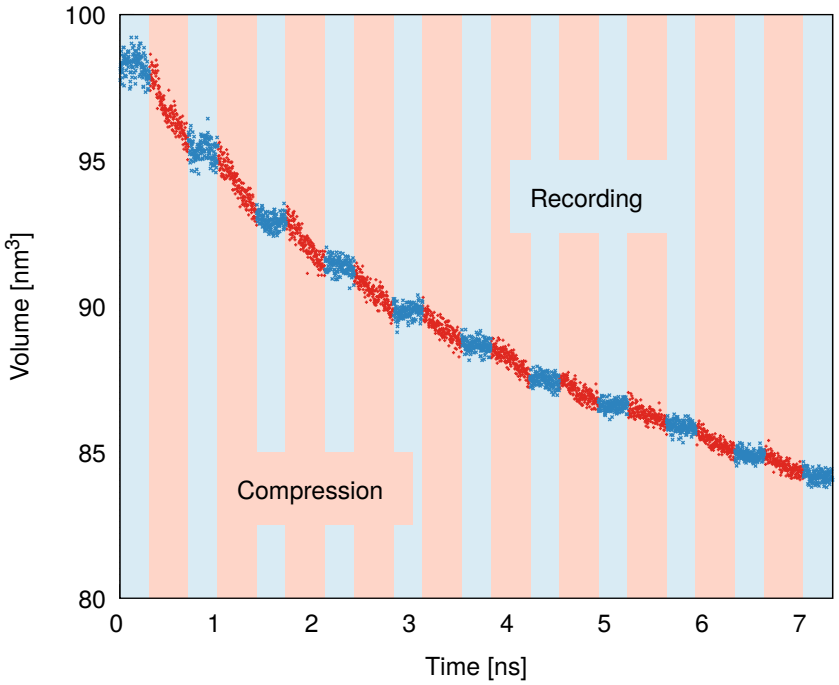


Figure 2.3.2: Example of the gradual compression of the HNBR structures to obtain the pressure-volume data. The recording stages (light blue) are 0.3 ns long, of which only the last 0.2 ns are used to compute the average volume at a given pressure. The compression stages (light red) are 0.4 ns long, during which the pressure is increased at a constant rate. The temperature is fixed at 298 K. For the sake of clarity, one in ten volume measurements is plotted here.

to 4.4 GPa for polystyrene [161–163], 2.9 GPa for polyisobutyl methacrylate [161], 1.5 GPa to 5.4 GPa for polymethyl methacrylate [161, 163]. Furthermore, loosely cross-linked HNBR has a lower bulk modulus than NBR, which can be understood with the replacement of stiff carbon-carbon double bonds with single carbon-carbon bonds.

2.3.3 Glass transition temperature

The glass transition temperature, T_g, is arguably one of the most important properties of an amorphous polymer. It is defined as the temperature at which long-range coordinated motions of the polymer become possible. T_g therefore distinguishes two regimes with

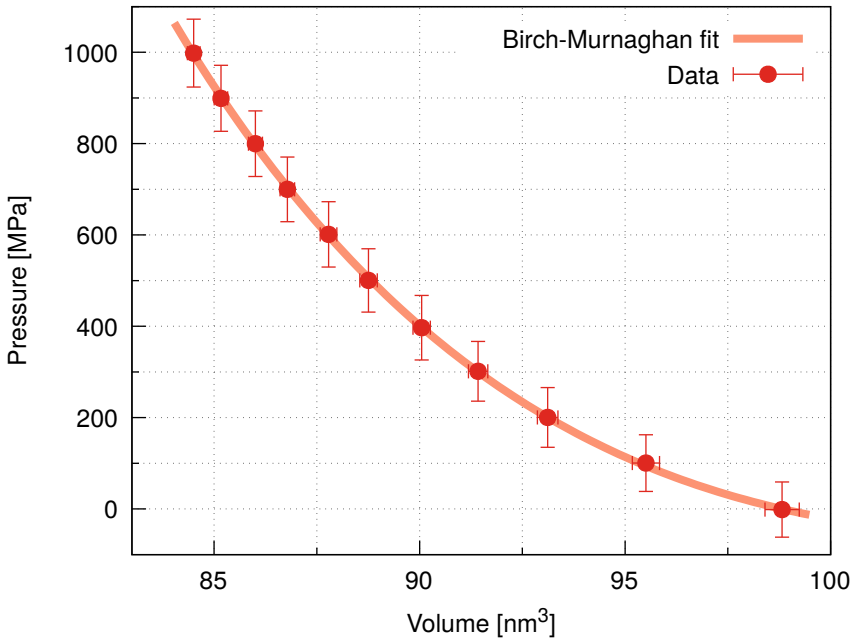


Figure 2.3.3: Example of pressure-volume relation obtained by gradual compression of 39 % ACN content, 0 % cross-linked HNBR at the constant rate of 2.5 MPa ps^{-1}. The temperature is held at 298 K. The Birch-Murnaghan equation of state is fitted to the data. The error bars for both pressures and volumes represent the standard deviations.

different physical properties*. Above the transition, the snake-like movement, also known as reptation, of polymer chains along their contours can take place, allowing structural changes due to the ability of chains to flow in the system. This regime is often called the "rubber" regime. Below the transition, the chain motions are restricted to thermal vibrations, making the polymer hard and brittle. This regime is often called the "glass" regime. This sharp difference in behaviour makes T_g a key property of amorphous polymers. An example of its importance is given by the *Challenger* disaster in 1986, which Feynman attributed to an elastomer seal-related failure caused by its glassy behaviour in a colder-than-ideal launch day [167].

*Despite this, T_g is not considered a phase transition. However, there is no clear consensus on whether or not some phase transition underlies the glass transition [164–166].

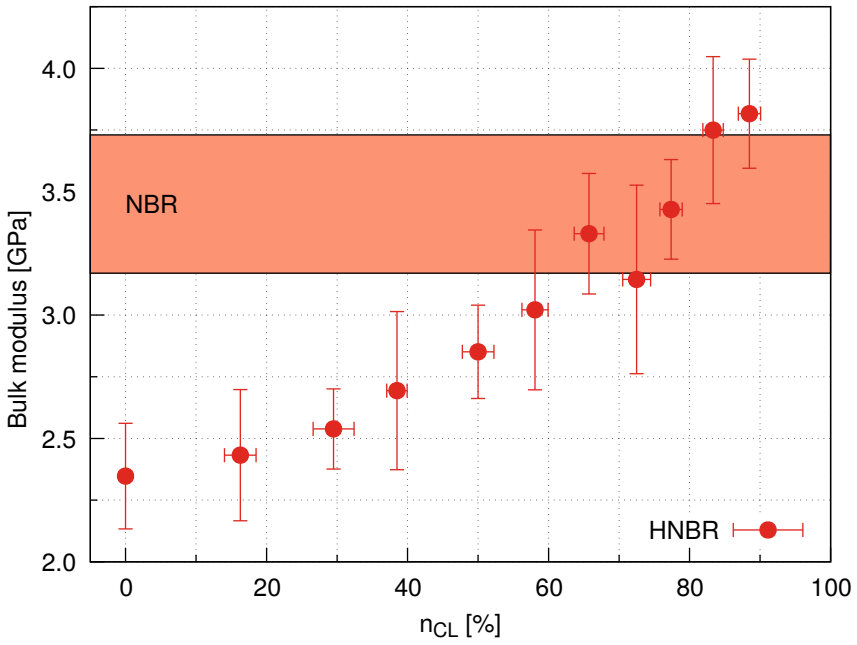


Figure 2.3.4: Computed bulk modulus for 39 % ACN content HNBR. The NBR has an ACN content of 41.3 %, its density was computed by Khawaja [85]. Temperature is fixed at 298 K. The error bars (for HNBR) and the shaded area (for NBR) represent the standard deviation over eight independently generated structures.

The partial derivative with respect to the pressure, at constant temperature, of the Gibbs free energy gives the volume, which can easily be calculated from simulations and, hence, gives us a handle to compute the temperature at which the glass transition occurs. The plot of the volume at different temperatures should therefore show two distinct regions characterised by two different gradients, and the transition between the two happens at T_g. In other words, on either side of T_g the thermal expansion coefficient differs. The following procedure was used. First, a structure equilibrated as outlined in subsection 2.2.4 is heated to 500 K over 2 ns at constant rate and later maintained at 500 K for 0.5 ns*. Then, the polymer is cooled by 15 K over 0.5 ns at constant rate before a 2 ns simulation, where temperature and volume are recorded every 0.2 ps for the last

*The possible effect of thermal hysteresis was tested on NBR; the volume-temperature curves showed no sizeable difference whether obtained by cooling or heating of the system [85, 133].

1.5 ns[*]. The process is repeated in a stepwise manner until the elastomer reaches a temperature of 150 K, generating a total of 24 volume-temperature averages spaced by 15 K. During all operations, an NPT ensemble is used with the pressure maintained at 0.1 MPa. Finally, the glass transition temperature is extracted from the volume-temperature curves following the method of Simperler [169], and summarised here.

1. The average temperature and volume values are arranged in N points, and the points are then divided into two subsets by assuming n of them belong to the glassy region and $N - n$ to the rubbery region.

2. For each subset, a linear fit and its coefficient of determination, R^2, are calculated. The total R_T^2 value for a given $P(V)$ curve is the sum of the R_g^2 and R_r^2 for the glassy and rubbery regime, respectively.

3. The procedure is repeated for all different $n \in [3, N-3]$ to ensure at least three points contribute to the linear fit in both regions.

4. The combination of linear fits that maximise R_T^2 is the one chosen.

The T_g is calculated as the intersection of the two lines that gave the highest combined coefficient of determination R_T^2. An example of this procedure can be seen in Figure 2.3.5 where it has been applied to a set of $V(T)$ data from a 39 % ACN content, 0 % cross-linked HNBR structure. This procedure is repeated for eight independently generated and equilibrated HNBR configurations at each n_{CL} percentage. The final reported T_g value at a given cross-link fraction is then the average over the eight configurations, while the uncertainty is the standard deviation.

Up to high degree of cross-linking, $n_{CL} \approx 80$ %, HNBR has a lower T_g than NBR (see Figure 2.3.6). This correlates with the drop in density, which increases the free volume of the system that in turn facilitates the chain reptation at lower temperatures. The expected trend that T_g increases with increasing cross-link fraction can be observed

[*]This is done to ensure the recorded data have no unphysical volume fluctuations due to the previous cooling and it is consistent with T_g simulations from the literature [168]. As a result, the volume fluctuations during the production runs are normally not exceeding 4 %.

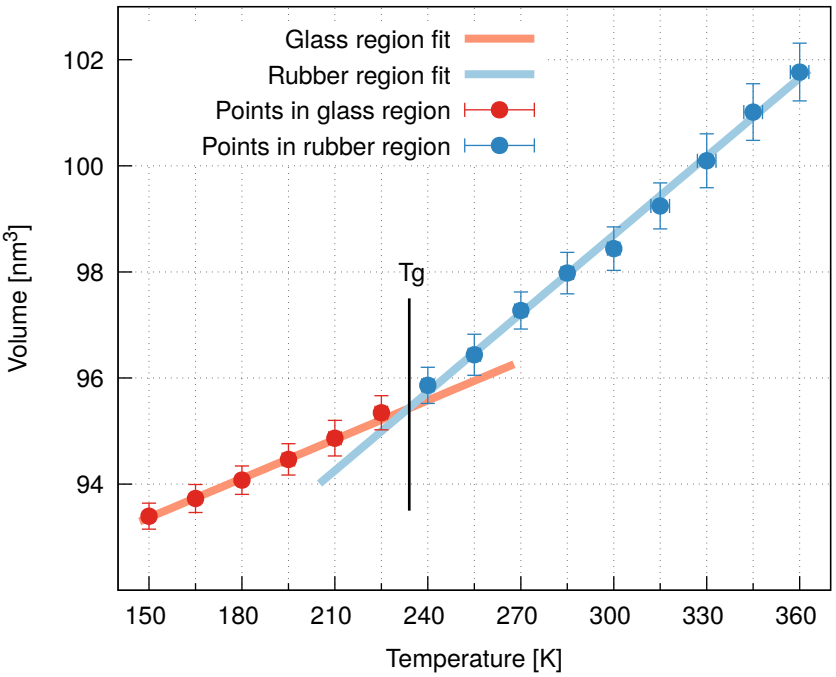


Figure 2.3.5: An example of volume-temperature data for a 39 % ACN content, 0 % cross-linked HNBR structure (0.1 MPa). The red points belong to the glassy region while the blue points to the rubbery one. A linear fit is performed on the two subsets and their intersection is the T_g for this specific structure. Error bars are the computed standard deviations.

in Figure 2.3.6. The covalent bonds added during the cross-linking procedure increase the number of constraints on the chain, limiting long-range coordinated molecular motions.

Experimental measurements of T_g as a function of the cross-link density have not been found in the public domain. However, a T_g value of 248.3 K is reported in [170] for a commercial formulation for 34 % ACN content, 0 % cross-link density HNBR. 234(15) K is the computed T_g value for a 39 % ACN content and 0 %, corresponding to the first point in Figure 2.3.6. A quantitative comparison between the computational and experimental values requires care. First, the discrepancy between the computed and experimental T_g is expected to worsen when accounting for the difference in ACN content. It has been previously shown by both experimental [128, 171] and computational [85, 133] results that T_g increases for increasing ACN content. Second,

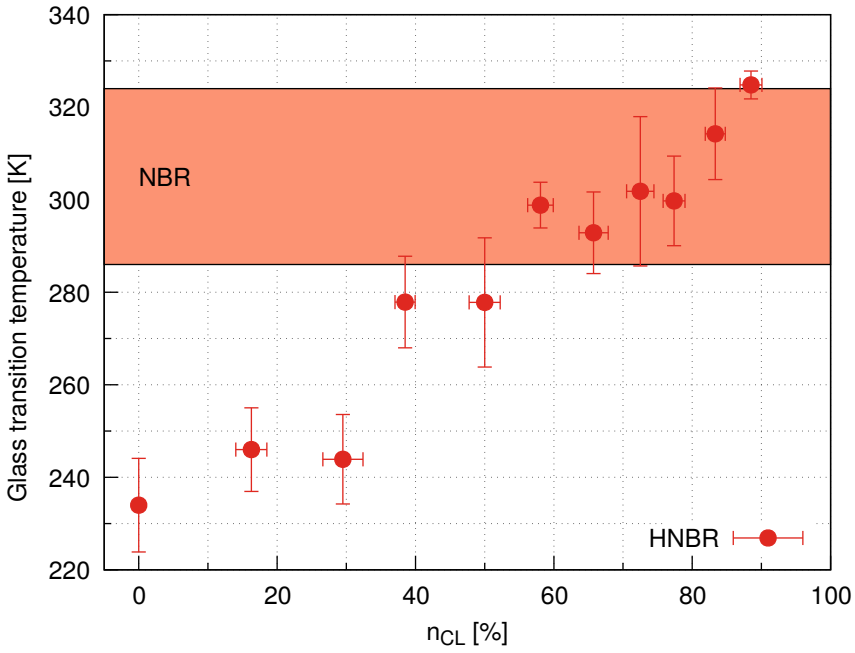


Figure 2.3.6: Computed T_g for 39 % ACN content HNBR. The NBR has an ACN content of 41.3 %, its T_g was computed by Khawaja [85]. Pressure is fixed at 0.1 MPa. The error bars (for HNBR) and the shaded area (for NBR) represent the standard deviation over eight independently generated structures.

the computation of T_g is highly sensitive to the initial configuration of the polymer. To illustrate the sensitivity to the initial structure, Khawaja increased the sample size for NBR by a factor of ten, studying the T_g for 80 independently generated structures [85]. The result is a highly-spread distribution of T_g values, with different structures showing differences in T_g prediction that can be up to 100 K. Third, T_g shows a dependence on the rate at which the system is cooled (or heated). Even in experiments, where different investigations can span seconds, minutes, hours or even days, T_g can be expected to change by 3 K to 5 K if the cooling (or heating) rate changes by one order of magnitude [172]. Cooling rates in computational experiments are normally in the order of 10^{10} K s^{-1} to 10^{11} K s^{-1} [168, 173]*, hence experiments allow for conformational

*As opposed to experimental cooling rates that are normally in the range of 10^{-1} K s^{-1} to 1 K s^{-1}.

changes that are unlikely to be successfully captured by MD. Fourth, different experimental techniques used to measure T_g are known to result in different values [174]. Fifth, but not last in importance, commercial formulations for HNBR suffers from a lack of transparency in their actual composition, meaning a variety of filler particles could have been added to the rubber. With these issues in mind, it is clear that the utility of such simulations lies in their ability to predict trends rather than the values calculated for T_g in any particular case.

2.4 Summary

In this chapter I presented a novel fully atomistic description of HNBR that is based on the synthesis of HNBR from NBR. The process opens the unsaturated NBR carbon-carbon double bonds, which are then cross-linked or hydrogenated based on a user-defined cross-link probability as well as the local atomic environment. To the best of my knowledge, this is the first time such a technique has been applied to HNBR and, furthermore, the first time the OPLS-AA force-field of Jorgensen [127] has been used to describe the inter- and intra-molecular interactions of this elastomer. Therefore, I sought to demonstrate the validity of this approach by computing several bulk properties and comparing them to both experimental data wherever possible, and previously computed values for NBR, the HNBR precursor.

The experimental trend of increasing density for higher cross-link fraction is reproduced. The paucity of experimental data prevents us from comparing the mass density over the entire range of investigated cross-linking degrees, however, the values available are within 3 % of the computed values. Furthermore, the experimental trend of higher density for NBR than for HNBR is observed. Similar agreement applies also to the glass transition temperature, although larger uncertainties were identified. The main source of the disagreement with experimental values of the T_g was attributed to the vast difference in cooling rates between experiments and atomistic simulations. The entangled and amorphous nature of HNBR makes large-scale conformational changes difficult to achieve within the time-scales of MD simulations. The bulk modulus was found to increase with increasing cross-link fraction, as expected, but no experimental data were

found for direct comparison.

The goal of this work was to provide an HNBR model – with chemical specificity and obtained from a NBR structure via hydrogenation and cross-link of the unsaturated double bonds – suitable to be used to investigate solubility and diffusion properties. By applying the solution-diffusion theory, this HNBR model has been used to study the permeation of small molecules such as He, CO_2, and water through nitrile rubber [85]. The main result highlighted that the solubility increases for increasing cross-linking of HNBR. This counter-intuitive result is found to correlate with the observed increase in free volume, which, for higher cross-linking, it is found to localise into increasingly larger clusters.

3

Polymer Nanocomposites Reinforcement

Polymers are often reinforced with the inclusion of nanoparticles within their matrix to enhance their mechanical, rheological and chemical properties. In this chapter I study the mechanical properties of elastomers filled with spherical particles using coarse-grained molecular dynamics computer simulations. Going from structures with low to high filler volume fraction (FVF), we see the following features: firstly, a yield drop appears in the stress-strain curve; then, as the FVF increases further, there is a reduction in plastic hardening; finally, at still higher filler loadings, failure via necking occurs. This behaviour is a result of the network formed by the polymer chains and filler particles, which is composed of three distinct types of local polymer-filler molecular structure motifs. The relative prevalence of these three motifs in the filled elastomer strongly depends on the FVF of the polymer and the observed qualitative changes in the mechanical response can be understood microscopically in terms of changes in the relative population of the three motifs.

3.1 Introduction

Polymers with nanoparticles (NPs) (or nanofillers or simply fillers) dispersed in the polymer matrix have been in use for almost 100 years [175], and relatively recent developments in methodologies to control their properties resulted in their widespread

adoption. To highlight their importance, according to [176], by 2022 the global polymer nanocomposites (PNCs) market will be worth 11 549 M$, which translates to a 10.9 % revenue growth. Whilst type and shape of the inserted NPs differ greatly, they all share one trait: at least one dimension of the fillers is less than 100 nm* [177]. A high surface-to-volume ratio characterises PNCs and it is the driver of the substantial differences and ability to alter the properties of the resulting component as compared to traditional composites. Flammability [3, 4], erosion resistance [5, 6], stiffness [7–9], and glass transition temperature [10–12] are only a few examples of the properties that can be altered by the incorporation of NPs in the polymer matrix. This work focuses on the mechanical response of PNCs.

While there exist a myriad of processing techniques to tailor NPs properties, for instance chemistry and NP surface [178, 179], the development of PNCs for advanced technology applications is hindered by our fundamental understanding and predictive power regarding the molecular mechanisms of how fillers modify polymer properties. Computer simulations provide a powerful framework to seek the solution to this problem. The difference in length-scales between NPs and the polymer chains poses a challenge to computational methods and, at least today, compromises have to be made†. Despite the fact that chemical accuracy must often be sacrificed in favour to CG models able to capture the relevant time- and length-scales, as highlighted in recent reviews [189–192], CG molecular dynamics (MD) simulations can be leveraged to gain fundamental insights.

Since its first use by Kremer and Grest in 1990 to study the dynamics of entangled linear polymer melts [111], the CG approach known as the bead-spring model has been widely adopted in both its basic formulation and with various extensions and generalisations. Its power can be traced back to the ability to reproduce trends in good agreement with both theoretical predictions, such as the Rouse and reptation model [193, 194], and experimental measurements, while having a relatively simple formulation.

*This implies that a high fraction of polymer chains interact with the nanoparticles, resulting in a significant portion of the polymer behaving differently than the rest of the bulk.

†Even the investigation of the mechanical properties of unfilled polymer system is often approached with coarse-grained (CG) models, for instance [180–188], mainly due to the long relaxation times that characterise all-atom descriptions.

Bead-spring models have been extensively used to investigate the mechanical properties of PNCs: Raos *et alia* used a coarse-grained dissipative particle dynamics approach to study the viscoelastic properties of rubber filled with spherical particles at constant filler loading under oscillatory shear deformations [195, 196]; Shen *et alia* investigated the strain-induced non-linear mechanical behaviour of a polymer filled with spherical and grafted nanoparticles, showing that there exists an optimal grafting density and grafted chain length that helps to improve the dispersion of the grafted NPs [197, 198]; Liu *et alia* studied the effect of FVF and polymer-filler interaction parameters on the mechanical response of reinforced elastomers, reporting the existence of an optimal FVF for mechanical reinforcement in the regime of strong polymer-filler interactions [199–201].

In this chapter, I use MD simulations and a CG bead-spring model to elucidate the molecular mechanism of mechanical reinforcement in polymer networks filled with spherical particles under uniaxial strain. Numerous studies on the mechanical properties of polymers have been conducted using the CG model presented in this chapter, for instance [199–201]. This provides solid foundations since the implementation of the model can be compared with existing literature in order to give the confidence necessary to proceed with the investigation. A summary of the model, followed by the presentation of the results and their discussion, and finally a summary of findings is now presented.

3.2 The model

The inclusion of a distribution of even the smallest filler would require length- and time-scale that are prohibitive for fully atomistic descriptions. For this work, a coarse-grained model based on the idealised polymer model proposed by Kremer and Grest [111] is adopted. The model is further developed with the aim of taking into account filler particles [200].

3.2.1 Inter- and intra-molecular interactions

The contribution to the total potential energy is split into two macro-categories: bonded and non-bonded interactions as in Equations 3.1, 3.2 and 3.3.

$$E = E_{\text{bonded}} + E_{\text{non-bonded}}, \tag{3.1}$$

$$E_{\text{bonded}} = E_{\text{FENE}} + E_{\text{LJ}}, \tag{3.2}$$

$$E_{\text{non-bonded}} = E_{\text{TSLJ}}. \tag{3.3}$$

The bonded terms, which apply only to the polymer chains, are represented by a combination of the FENE potential and a LJ potential, as in previous studies [111, 200]*. With the separation between adjacent bonded beads indicated with r, Equation 3.4 gives the total analytical form of E_{bonded}.

$$E_{\text{bonded}} = -\frac{1}{2} k R_{\text{B}}^2 \ln\left[1 - \left(\frac{r}{R_{\text{B}}}\right)^2\right] + 4\varepsilon\left[\left(\frac{\sigma}{r}\right)^{12} - \left(\frac{\sigma}{r}\right)^{6}\right]. \tag{3.4}$$

To avoid chain-crossing and high frequency modes, the values of the constants are set to $R_{\text{B}} = 1.5\,\sigma$ and $k = 30\,\varepsilon/\sigma^2$ [111]. The potential curve of this non-Hookean effective spring is sketched in Figure 3.2.1. At distances smaller than the equilibrium point†, the major contribution to the potential is given by the repulsive part of the LJ potential and it accounts for the impenetrability of the monomer beads. For distances larger than the equilibrium and up to the asymptote at $R_{\text{B}} = 1.5\,\sigma$, the logarithmic part prevails. Note that bonds described with this potential cannot be broken and have a finite maximum extension as opposed to other descriptions of the bond interactions such as Hookean, linear, harmonic springs.

There exist three different types of non-bonded interactions, i, in this model, $i \in$ [bead–bead, bead–filler, and filler–filler]. All of the above share the same functional form: a TSLJ potential‡ shown in Equation 3.5. However, the parameters differ to

*No higher-order bonded terms, such as angles and dihedral angles, are included in this model.

†The minimum of the E_{bonded} potential is at $r_{\text{eq}} \approx 0.9609\sigma$.

‡To avoid confusion, often with TSLJ only the shift in energy (or y-shift) is considered. However, here I refer to a double-shifted and truncated LJ potential where both a y- and x-shift (where the x-shift is a distance

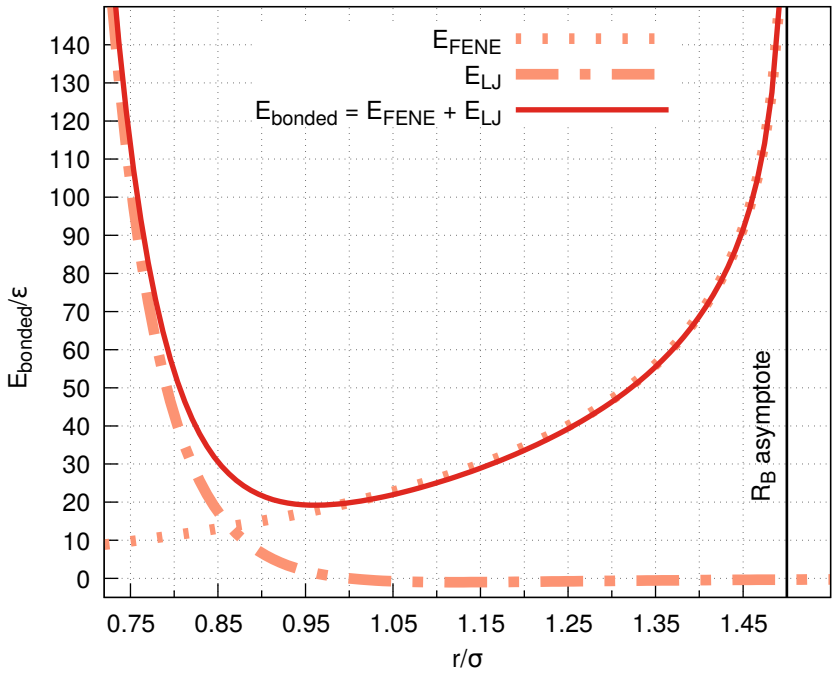


Figure 3.2.1: Plot of E_{bonded} for adjacent bonded monomers. For small distances, r, the interaction is dominated by the repulsive part of the LJ term, while the logarithmic part prevails roughly past the minimum up to the asymptote at $R_B = 1.5\,\sigma$. On this scale, the attractive part of the LJ potential cannot be appreciated.

account for the different type of interaction. The filler–filler non-bonded potential is sketched in Figure 3.2.2

$$E^{i}_{TSLJ}(r) = \begin{cases} 4a_i\left[\left(\dfrac{\sigma}{r-\Delta_i}\right)^{12} - \left(\dfrac{\sigma}{r-\Delta_i}\right)^{6}\right] - E_{\text{LJ}}\left(r_i^c\right) & \Delta_i < r \leq r_i^c + \Delta_i, \\ 0 & r > r_i^c + \Delta_i, \\ +\infty & 0 < r \leq \Delta_i. \end{cases} \tag{3.5}$$

The values for a_i, Δ_i, and r_i^c control the strength of the interaction, the shift to account for excluded volume effects, and the distance at which the interaction is truncated and shifted so that force and energy are zero, respectively. Table 3.2.1 summarises the values used in

shift) are applied.

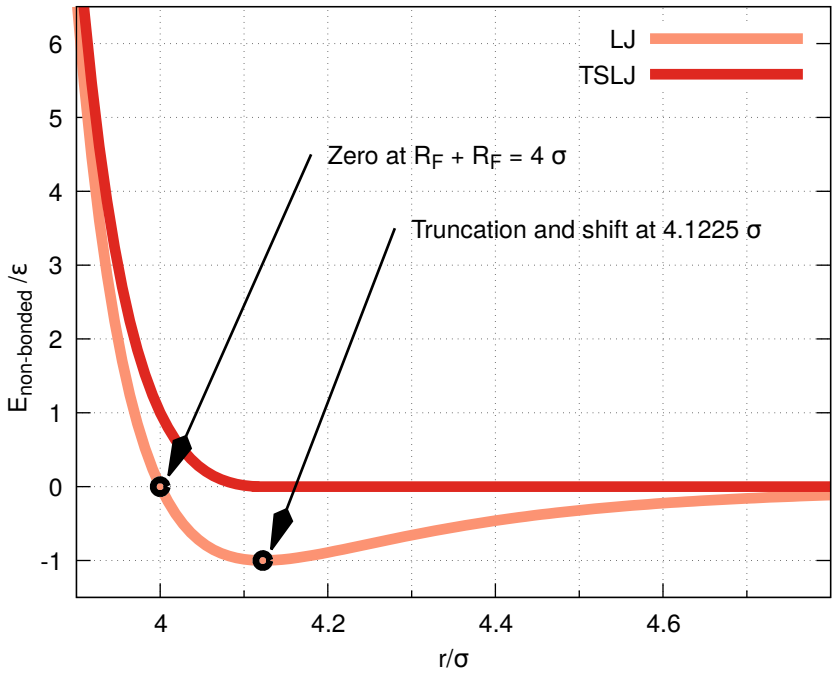


Figure 3.2.2: Plot of the TSLJ, Equation 3.5, for the filler–filler interaction. The truncation and shift at the minimum of the potential results in a hard-sphere potential, effectively equivalent to a purely repulsive Weeks-Chandler-Andersen potential [202].

this study. The weak interaction between real fillers* motivates the purely repulsive

i	$a_i\,[\varepsilon]$	Δ_i	$r_i^c\,[\sigma]$
Bead–bead	1	0	$2\sqrt[6]{2}$
Bead–filler	5	$R_F - \sigma/2$	$2\sqrt[6]{2}$
Filler–filler	1	$2R_F - \sigma$	$\sqrt[6]{2}$

Table 3.2.1: Summary of the parameters used in this work for the non-bonded interaction (a TSLJ potential, Equation 3.5), where a_i, Δ_i and r_i^c are defined in the main text. R_F stands for the radius of the spherical filler particles. In this work $R_F = 2\sigma$. The choice of this parameters coincides with the one made in [200].

*NPs are often made of silica, clay, and carbon black, which are thought to exhibit small interactions amongst each other.

interaction adopted for the filler-filler potential. Effectively, $i =$ filler–filler is equivalent to a purely repulsive Weeks-Chandler-Andersen potential [202]. On the other hand, the bead–filler interaction is attractive and is set to five times the bead–bead interaction, with the aim to model relatively strong polymer–filler interfacial interactions resulting from, for instance, functionalisation of the filler particles. The shift used to account for the excluded volume of the fillers, Δ_i, is chosen so that $\Delta = R_1 + R_2 - \sigma$, where R_1 and R_2 are the radii of the two particles taking part to the interaction. With this choice, the zero of the TSLJ is shifted at a distance equal to that of the sum of the two radii. Polymer beads have a radius of $\frac{1}{2}\sigma$, while fillers are represented by spherical particles with radius $R_F = 2\sigma$. LJ reduced units are used throughout this work, meaning the mass, m, and the LJ parameters σ and ε are set to unity, Equation 3.6. The underlying motivation is that it is not the aim of the investigation to study a specific polymer system [200].

$$m = \varepsilon = \sigma = 1.0 \tag{3.6}$$

As a result, *all* the reported results are dimensionless. In the following section, the procedure used to determine the initial coordinates for the polymer beads and NPs is explained.

3.2.2 Structure generation

First, the specified number* of spheres of radius $R_F = 2\sigma$, representing the filler NPs, are randomly and one by one positioned in a large, cubic, and periodic box. The lateral dimension of the cubic box is chosen so that, once all fillers and polymer chains are placed, the resulting density is equal to roughly 30 % of the equilibrium number density of the unfilled system, which is $\rho \sim 0.85$ [111, 200]. This large initial volume is used to ensure that the overall process of generating the initial configurations is computationally efficient and does not stagnate as a result of packing constraints.

Once all the fillers are placed, the chains are added one bead at the time, in the space left available in the box, in a self-avoiding fashion described below.

*This number ranges from 0 to 1500 to mimic different filler loadings.

1. A random position, within the zeroth image of the periodic box, is picked as tentative placement for the first bead of a chain, n_1^j, where $j \in [1, M]$ is the chain index and M the total number of chains. The trial coordinate is accepted if it overlaps with none of the previously positioned elements*. Otherwise, the step is repeated until the placement is accepted.

2. Random coordinates on a sphere of radius 0.96σ† and centred on n_1^j are picked and tested for steric overlap with all the previously placed elements. If the positioning is valid, the second bead, n_2^j, is added the to the atom list and the list of bonds is updated accordingly.

3. Trial coordinates for the subsequent beads $n_i^j,\ i \in [3, N]$, where N is the number of beads per chain, are not randomly chosen on a sphere centred on n_{i-1}^j. This would result in a high rejection ratio since a non-negligible portion of the solid angle is already occupied by n_{i-2}^j. Therefore, the suggested placement is randomly picked from a "carved" sphere obtained by removing the range of angles that would automatically result in an overlap with n_{i-2}^j. This operation is repeated until $i = N$, i.e., the number of beads per chain is reached. The force-field information is amended accordingly.

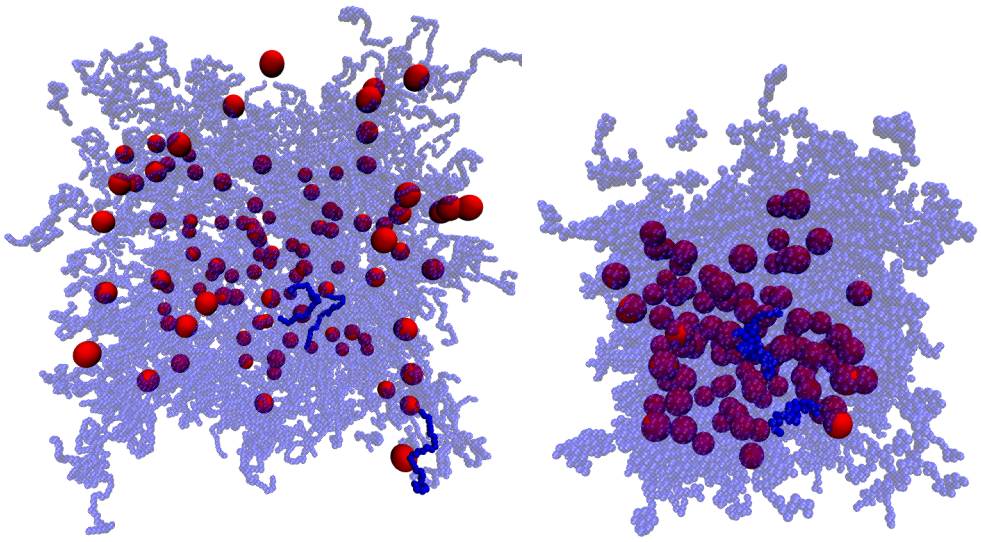
4. The whole procedure is reiterated until the total number of chains M is reached.

For this investigation, M is fixed at 1000 and N at 30, which is below the entanglement length of such systems [111, 200]. The mass of the polymer beads is $m = 1$ and the same mass density is assumed for the NPs, resulting in a filler mass which is 64 times greater than the one of the beads. An example structure as obtained by the aforementioned

*Technically, first, the steric overlap is checked using the radii of the particles and any move that would imply a distance shorter than the sum of the two radii involved is rejected. Such condition is maintained until 50 trials fail consecutively, at which point a 5 % steric overlap is allowed. This is reiterated for up to three times, potentially allowing a total overlap of 15 % between the elements. After 150 consecutive unsuccessful placements, the procedure is stopped and restarted. The general idea is to have a computationally efficient algorithm, however, in less than 1 % of the cases the 15 % overlap condition was required. Furthermore, the potential does not diverge to infinity at exactly the radius of an object, but at a distance σ from it, hence, the allowed overlap is not unphysical according to the model.

†Hence close to the minimum energy configuration of the bond that will connect them.

structure generation can be seen in Figure 3.2.3a, while Figure 3.2.3b shows the same structure once the equilibration routine, outlined in the following section, is performed.



(a) Pre-equilibration **(b)** Post-equilibration

Figure 3.2.3: Snapshots of a structure before, (a), and after, (b), the equilibration routine. Both images have unwrapped coordinates, 100 inserted fillers, and 30 000 polymer beads organised in 1000 chains of equal length. Three chains are highlighted to give an example of chain conformations. VMD [203] and the TopoTools plug-in have been used to generate the images*.

3.2.3 Further details

Equilibration

After the initial structure generation, an equilibration routine is necessary to relax the system as well as to bring the polymer from low to melt density. The general idea used to equilibrate the structures is derived from the procedure outlined in subsection 2.2.4†. A

*The TopoTools plug-in has been written by Axel Kohlmeyer, (2016). Release 1.6, http://doi.org/10.5281/zenodo.50249. The combination of VMD+TopoTools is the choice for imaging used throughout this dissertation, henceforth it will not be repeated.

†Also in this case, the minimisation step used the FIRE algorithm [138] as implemented in large-scale atomic/molecular massively parallel simulator (LAMMPS) and the exit criteria are 1. energy fluctuations

complete summary of the whole procedure is presented in Table 3.2.2. LAMMPS is the MD engine of choice for all simulations [140], and a timestep of $\delta t = 0.001$ is used to integrate the equations of motion. The Nosé-Hoover formulation for barostat and thermostat [143, 144, 146], as implemented in the LAMMPS code [140], is used throughout this work to control pressure and temperature, respectively.

Stage	Stage duration [timestep]	Total time [timestep]	Temperature	Pressure
Energy minimisation	-	-	-	-
NPT (compression)	200 000	200 000	1.0	$0.0 \rightarrow 20$
NPT	200 000	400 000	1.0	20
NPT (decompression, heating)	500 000	900 000	$1.0 \rightarrow 1.5$	$20 \rightarrow 0.0$
NPT	200 000	1 100 000	1.5	0.0
NPT (cooling)	200 000	1 300 000	$1.5 \rightarrow 1.0$	0.0
NPT	5 000 000	6 300 000	1.0	0.0

Table 3.2.2: Stages used to equilibrate the CG polymer nanocomposite structures.

Cross-linking

Once the randomly generated initial structures are equilibrated as outlined above, extra bonds are introduced in the system to mimic a loosely cross-linked network. The cross-linking is performed dynamically, using the `bond/create` function of LAMMPS[*], during a constant number of particles, pressure and temperature simulation. The reduced pressure is set to $P = 0.0$ and the reduced temperature to $T = 1.0$, well above the glass

within 0.0001 % and 2. 50 000 steps, whichever occurs first. Also, any change in pressure and temperature is performed at constant rate over the time allocated.

[*]The reader might wonder why the same LAMMPS built-in routine has not been used in chapter 2. While the routine updates the atom type and, optionally, all the bonded terms of the force-field, it does so in a "local" way. For instance, when changing the nature of a carbon atom from sp^2 to sp^3, a similar modification has to be applied to the atom that shares the original double bond with it. This feature is not, yet, implemented in the LAMMPS built-in routine, therefore the force-field parameters are not amended correctly for the atoms neighbouring the cross-link candidate. Whilst this is not problematic for the CG model presented here, it implies a loss of accuracy for the optimised potential for liquid simulation - all atom (OPLS-AA) hydrogenated nitrile butadiene rubber (HNBR) model developed and tested in chapter 2.

transition for the system [200]. A summary of the procedure is the following. Pairs of beads within a distance of 1.25σ are flagged as potential cross-linking sites if there is no bond already connecting them. The candidates are then cross-linked with a probability set to 0.03 %*, and the force-field information is amended accordingly. The dynamic cross-linking automatically stops once 1000 bonds are added to the system – in other words, once the target of one cross-link per chain on average is reached. An equilibration, in all aspects equal to the one presented in subsection 3.2.3, is performed with the goal to relax the new stretched bonds and any structural modifications introduced.

The final size of the periodic and cubic box depends on the total number of filler particles inserted, which ranges from zero (unfilled) to 1500. The total volume therefore ranges from $34.4(1)\ k\sigma^3$ to $99.5(1)\ k\sigma^3$ for zero and 1500 filler particles inserted, respectively. The average volume and standard deviation are computed on an ensemble of eight independently generated structures at each FVF.

Filler volume fraction

The FVF for all the structures is calculated right after the equilibration routine following the cross-linking of the system since the added bonds have the effect of increasing the overall density. The FVF calculation is performed over 50 000 timesteps ($P = 0.0$ and $T = 1.0$), where the value for the volume is recorded every 100 timesteps and used to compute the average volume and its standard deviation. Among the eight interdependently generated structures with the same number of inserted fillers, the differences in the average FVF are very small compared to the standard deviations. As a result, the eight structures with the same number of fillers are treated as having the same FVF and used to compute ensemble averages at constant FVF throughout this work. Figure 3.2.4 shows the range of FVFs investigated and the number of fillers used to achieve them.

*This avoids inserting too many new bonds at the same timestep, but at the same time prevents stagnation of the cross-linking procedure.

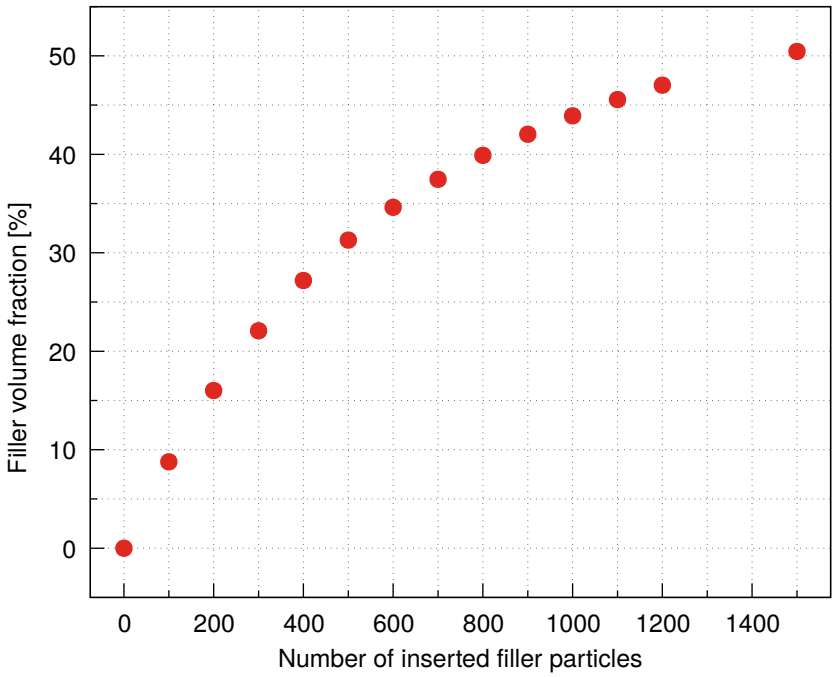


Figure 3.2.4: Number of filler particles inserted versus the computed FVF after the cross-linking and second equilibration. The temperature and pressure are fixed at $T = 1.0$ and $P = 0.0$. The FVF reported is the average over eight independently generated structures. The standard deviations are also plotted, however, they are too small to be appreciated on the scale of this plot.

Timestep and parallel efficiency

As outlined in subsection 2.2.6, for anyone wishing to explore and exploit the power of MD simulations, it is important to determine an appropriate balance among efficient sampling of the dynamics, appropriate integration of the equations of motion, and management of the computing resources. With this goal in mind, tests on the parallel efficiency and on the timestep to integrate the equations of motion were performed. The nature of these tests is similar to the investigations performed and detailed in subsection 2.2.6, therefore, an extended discussion is omitted. Here, only the chosen parameters are summarised, and, to avoid repetitions, a similar approach will be taken henceforth. Throughout this chapter, the timestep is fixed at $\delta t = 0.001$, consistent with

similar studies that used comparable models [198, 200, 201]. Each MD simulation is performed on 16 cores, which also corresponds to the number of cores per node on the nodes used for this investigation*.

Stress-strain

Structures created, equilibrated, cross-linked, and re-equilibrated as outlined in section 3.2 are uni-axially strained along the z-axis. The ensemble of choice for the straining is the $NTL_z\sigma_{xx}\sigma_{yy}$ one, Figure 3.2.5, where the total number of particles, temperature, and the stresses normal to the straining direction, z-axis, are kept constant [204]. Throughout this work, pressure and temperature are fixed at $P = 0.0$ and

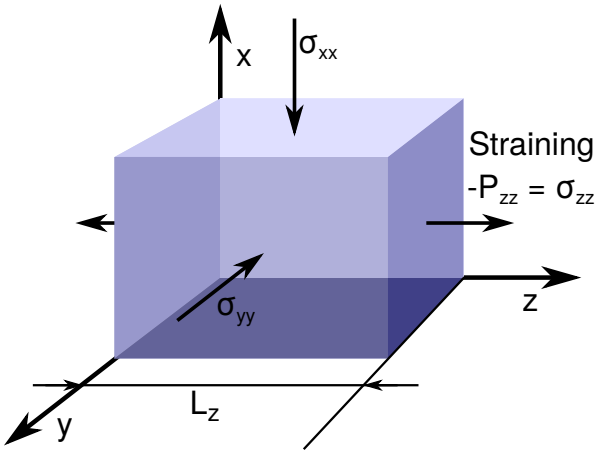


Figure 3.2.5: Simulation cell geometry and coordinate system used in the $NTL_z\sigma_{xx}\sigma_{yy}$ ensemble.

$T = 1.0$, respectively, and the stresses σ_{xx} and σ_{yy} are held at zero. In other words, contrary to the literature investigating similar systems [200], the structures are not compressed along the x- and y-axis to enforce volume conservation†.

To simulate the straining of the structures, the length of the simulation box along the

*Meaning the communication time between different nodes is avoided.

†In other words, a Poisson's ratio of 0.5 is not imposed on the system.

z-axis, L_z, is increased at constant and uniform strain rate $\dot{\eta}$, as in Equation 3.7.

$$L_z(t) = L_z(0)(1 + \dot{\eta}t). \tag{3.7}$$

Here $L_z(0)$ is the box side in the z direction before the structure is strained, $L_z(t)$ the value at time t during the straining, and the strain rate, $\dot{\eta}$, is kept constant at $3.27\,\%$ every $\tau = \frac{1}{\delta t} = 10^3$ timesteps[*]. The straining is performed for a time of 100τ, resulting in a final strain on the system of $327\,\%$ at the end of each simulation. The stress along the straining direction, σ_{zz}, is given by the negative of the zz-pressure from the pressure tensor. At each FVF, the reported stress at a given strain is averaged over eight independently generated systems. The width of the shading of the stress-strain curves signifies the standard deviation of the calculated stresses.

3.3 Results & discussion

3.3.1 Validation of the model

The model used throughout this investigation is relatively simple, nevertheless, a comparison with the existing literature is necessary to provide the confidence required to proceed with the investigation. Number density, glass transition temperature, and bulk modulus of *unfilled and uncross-linked structures* are computed and, except for the isothermal incompressibility, compared to existing studies. All the following results are averages over an ensemble of eight independently generated structures.

The number density for a given structure is computed over a 50 000 timesteps NPT simulation, where temperature and pressure are set to $T = 1.0$ and $P = 0.0$, respectively. The density is recorded every 100 δt, resulting in 500 values then used to compute the average for every structure. The reported values for mass density and its uncertainty are computed on the ensemble of eight independently generated structures. Kremer *et alia* report a number density of $\rho = 0.85$ [111], Liu *et alia* of $\rho = 0.84$ [200], and, in this work, $\rho = 0.86(1)$ was obtained.

[*]The constant strain rate is set equal to that of previous similar studies with similar models [200, 201, 205].

The glass transition temperature (T_g) is computed with a procedure similar in nature to the one used for HNBR and detailed in subsection 2.3.3, only adapted to account for the differences in the two models. In particular, the volume of the structure was recorded from a temperature of $T = 1.0$ to a final temperature of $T = 0.05$, at steps of $\delta T = 0.05$, and the pressure fixed at $P = 0.0$. Temperature is decreased at a constant rate over 100 000 timesteps, and the cooling is followed by a 500 000 timesteps NPT simulation, where the volumes are recorded every 100 timesteps over the second half of the simulation to account for volume readjustments. The average volume is computed at every temperature, and the set of $V(T)$ data used to extract the glass transition as detailed in subsection 2.3.3. Liu reports $T_g \sim 0.4$ [200, 206], and the model presented here results in a glass transition of $T_g = 0.408(1)$.

Finally, the isothermal incompressibility is calculated. The pressure of the simulation is increased from $P = 0.0$ to $P = 15.0$ at steps of $\delta P = 1.0$, while the temperature is kept constant at $T = 1.0$. The compression is performed at constant rate in a 100 000 timesteps long NPT simulation, followed by a 500 000 timesteps NPT simulation, and the volume recorded and averaged over the second half of it. $P(V)$ data are then fitted to Equation 2.33, and the bulk modulus computed. Full details on the procedure can be found in subsection 2.3.2 The bulk modulus value obtained is $B_0 = 10.4(3)$ and, to the best of my knowledge, there exist no literature values to use as a comparison.

3.3.2 Stress-strain response and FVF

Stress-strain curves corresponding to 0.0 %, 27 % and 47 % FVF are shown in Figure 3.3.1(a), (b), (c), respectively, and Figure 3.3.1(d) and (e) show examples of structures at the beginning and end of the straining procedure for 0.0 % and 47 % FVF, respectively. Figure 3.3.1(a) serves as a reference point for the mechanical effects of fillers embedded in the polymer matrix since this corresponds to the unfilled case. In the stress-strain response at 27 % FVF, Figure 3.3.1(b), quasi-elastic (up to 5 % strain) and plastic (for strains greater than 5 %) regimes are clearly defined. At 47 % FVF, Figure 3.3.1(c), there is a clear yield drop in the stress-strain response, as indicated by the appearance of a pronounced peak in the stress. There is also a marked weakening of the

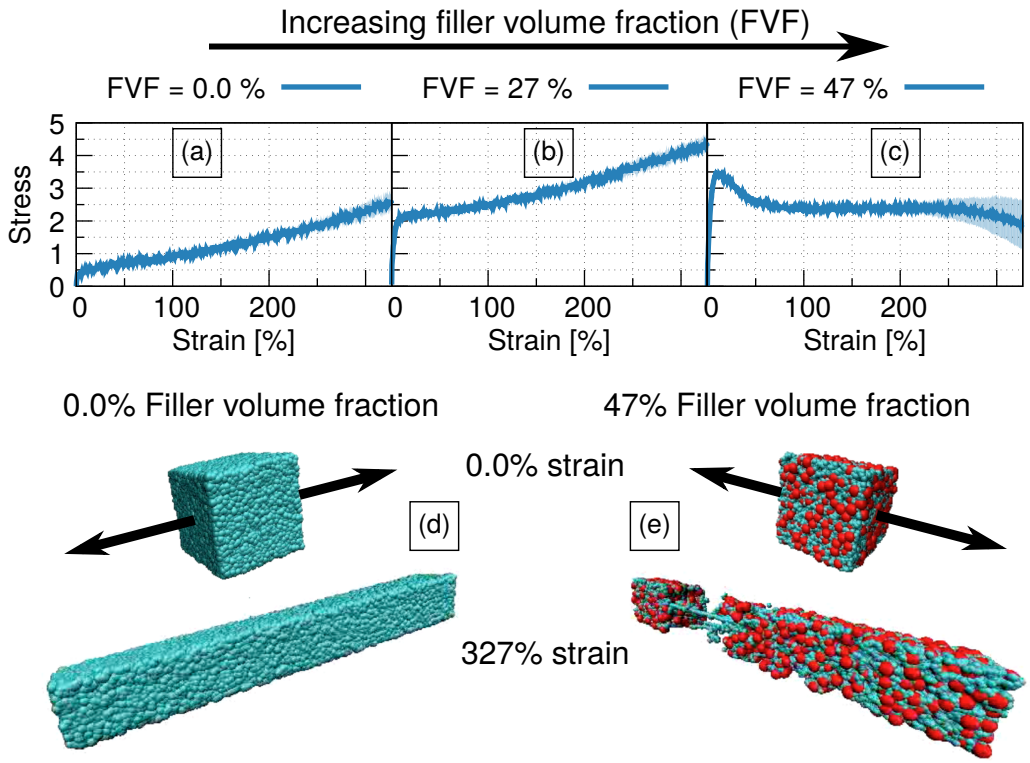


Figure 3.3.1: (a), (b) and (c) show stress-strain curves for three FVF exhibiting qualitatively different responses to the loading. (d) and (e) are example of structures at the beginning and end of the straining procedure. (d) is a structure with no filler loading while (e) has a 47 % FVF. In the latter necking can be observed.

plastic regime, signified by the lower slope of the curve after the yield drop as compared to the case of 27 % FVF. Moreover, for strains exceeding 250 %, there is the onset of mechanical failure, which ultimately results in the necking observed in Figure 3.3.1(e). The standard deviation in the mechanical response among the eight structures at all FVFs is generally small, indicating a weak dependence of the stress-strain curve on the initial structures with the same FVF.

For FVF up to 27 %, the filled polymer is progressively reinforced by the inclusion of more particles, Figure 3.3.2. The quasi-elastic regime exhibits a progressively higher modulus; there is no substantial change in the range of strain over which the stress-strain

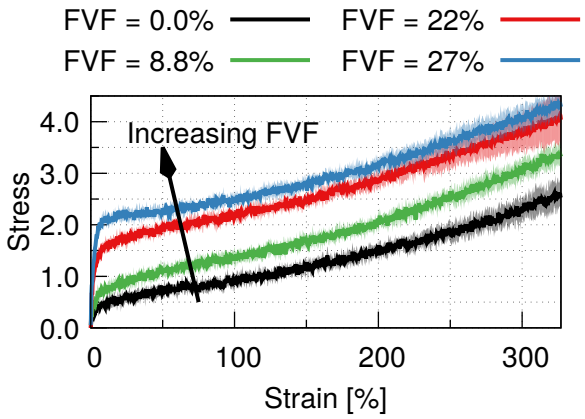


Figure 3.3.2: Stress-strain curves for four different FVF, corresponding to 0.0 %, 8.8 %, 22 %, and 27 %.

curve is quasi-elastic; there is no substantial change in the slope of the plastic regime. In other words, the curves are approximately only shifted towards higher stresses for the same strain without other substantial changes. A different picture emerges, however, for higher FVFs. In Figure 3.3.3, the stress-strain curves for 27 %, 31 %, and 35 % are presented. At 31 % FVF, the mechanical response is further reinforced, but a yield drop appears, resulting in a qualitatively different stress-strain response. This yielding phenomenon characterises all the structures beyond 31 % FVF, becoming more prominent for higher FVFs. The presence of a threshold in the FVF, at constant filler-polymer interaction strength, after which the yield drop appears suggests a structural change occurs in the system. Moreover, a weakened slope of the plastic regime for 35 % FVF is visible, effectively indicating the existence of an optimal FVF for mechanical reinforcement at large strains. This observation is supported by similar results from the literature [200]. To understand the molecular origin of the variation in mechanical response as a function of filler loading, the nature of the polymer-filler network is investigated.

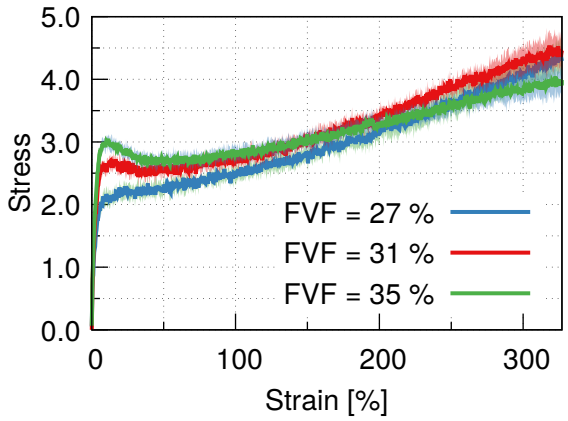


Figure 3.3.3: Stress-strain curves for three FVFs corresponding to 27 %, 31 %, and 35 %. Up to 27 % FVF (blue) the mechanical response does not exhibit a yield drop and the PNC is reinforced as compared to lower FVFs, Figure 3.3.2. At 31 % FVF (red) a peak appears between the elastic and plastic regime while at the same time the system is further reinforced. At 35 % FVF (green) the peak is clearly present and the plastic regime becomes weakened compared to lower filler volume fractions.

3.3.3 Polymer-filler network at equilibrium (0 % strain)

The radial distribution function (RDF) is calculated between all fillers for all structures at all FVFs. The RDFs are computed after the structures are equilibrated, but before being strained. For each equilibrated structure, a total of 50 snapshots separated by $100\delta t = 0.1\tau$ are recorded and used to compute the average RDF of a single structure. Figure 3.3.4 shows examples of the RDF for one representative structure for the cases of 27 % and 40 % FVF. The distributions show clear peaks corresponding to three coordination families: (1) fillers in direct contact with each other, with corresponding peak at $2R_F = 4\sigma$; (2) fillers separated by one layer of polymer beads, with corresponding peak at $2R_F + \sigma = 5\sigma$; and (3) fillers separated by two layers of beads, with corresponding peak at $2R_F + 2\sigma = 6\sigma$. The area under each peak is a measure of the prevalence of the corresponding coordination family within the polymer-filler network. In Figure 3.3.5, we show this quantity as a function of FVF, where the value reported for each FVF is an average over an ensemble of eight independently generated structures. The label BB ("bridging beads") denotes the number of polymer bead layers between two

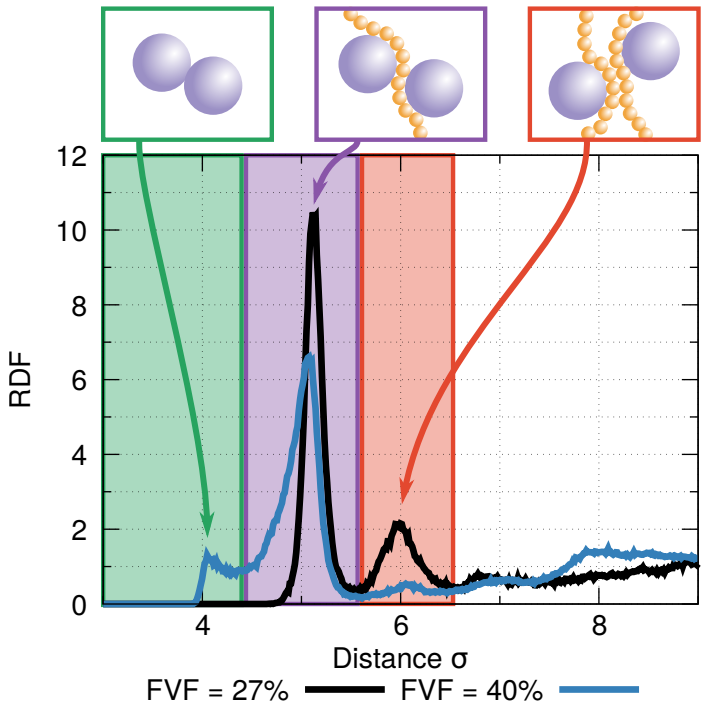


Figure 3.3.4: Examples of RDFs: black corresponds to a 27 % FVF structure, and blue to a 40 % one. The former shows peaks at 5σ and 6σ that correspond to fillers separated by one and two layers of polymer beads, respectively. The RDF for the 40 % FVF structure shows a clear peak at 4σ, which relates to fillers in direct contact with each other.

fillers and is used to distinguish the different coordination families henceforth. Three main regimes are identified:

- Up to 27 % FVF: reinforcement. For FVF less than 27 %, filler–filler interactions are almost entirely mediated by either one (BB = 1) or two (BB = 2) bridging polymer bead layers. As the FVF increases up to 27 %, the prevalence of BB = 1 increases, whilst BB = 2 stays approximately constant. At the same time, the filled polymer is progressively reinforced by the inclusion of more filler particles, as shown by the stress-strain curves in Figure 3.3.2. A negligible fraction of filler particles are in direct contact (BB = 0) and there is no discernible peak corresponding to BB $\geq$ 3. There is an energetic driving force for polymer beads to

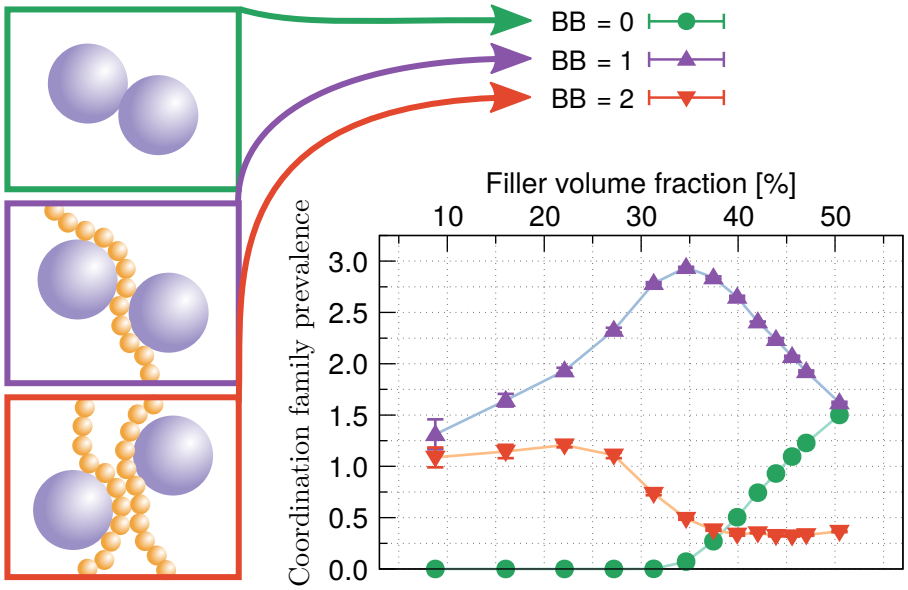


Figure 3.3.5: Prevalence of the different peaks in the filler–filler RDF as a function of FVF. The three curves correspond to the first three peaks in the distribution that indicate: (green) fillers touching directly (BB = 0), (purple) fillers touching via one layer of polymer beads (BB = 1) and (orange) fillers touching via two layers of polymer beads (BB = 2). The error bars are the standard deviations among eight independently generated structures.

coordinate the filler particles* and, as the FVF increases, BB = 1 dominates over BB = 2 since it allows for lower energy configurations by increasing the overall count of filler-bead interactions.

- At 31 % FVF: yield drop. Between 27 % and 31 % FVF, there is an onset of a relatively abrupt depletion of BB = 2, which correlates with the appearance of a yield drop in the stress-strain response of the system as shown in Figure 3.3.3 (FVF=31 %). The relative abundance of BB = 1 increases through this range of FVFs, while BB = 0 remains absent. Whilst a yield drop appears at 31 % FVF, the quasi-elastic region of the stress-strain response is extended and the plastic region is not weakened as compared to the case of 27 % FVF.

*As the strength of the interaction between the beads and the filler particles is set five times greater than the bead–bead one, Table 3.2.1.

- For FVF$>31\,\%$: plastic weakening. As the FVF increases beyond $31\,\%$, the prevalence of BB $= 1$ continues to rise, reaching a maximum at $35\,\%$ FVF, and the BB $= 0$ family, corresponding to fillers directly in contact, starts to appear, Figure 3.3.5. At $35\,\%$ FVF, the stress-strain response (green curve in Figure 3.3.3) at low strains is further reinforced as opposed to lower FVFs and the quasi-elastic regime extended. However, the curve presents both a yield drop as well as a weakened plastic regime, as shown by the reduced slope of the plastic regime as compared to the case of $27\,\%$ and $31\,\%$ FVF. It is perhaps not surprising that the appearance of the BB $= 0$ family correlates with the observed weakening of the PNC. The direct filler–filler interaction is limited to the repulsive part of the LJ potential (see interaction parameters in Table 3.2.1), therefore there is no energy cost in separating them. As a result, structures in the BB $= 0$ family effectively act as nucleation points for mechanical weakening of the system. The specific geometry and location of such nucleation points will depend strongly on the specific realisation of the structure being examined, which rationalises the relative higher variance at large strains in the stress-strain curve of Figure 3.3.1(c) as opposed to lower FVFs. Beyond $35\,\%$ FVF, the weakening of the plastic regime is exacerbated, eventually leading to the almost complete mechanical failure observed in Figure 3.3.1(c) for $47\,\%$ FVF.

In this model, the network formed by the polymer chains and the filler particles at equilibrium ($0\,\%$ strain) undergoes changes as a function of FVF which correlate with the qualitative evolution of the mechanical response as determined by the stress-strain curves for different FVFs. In particular, the observations indicate the existence of an optimal filler loading for PNCs if interested in the mechanical response at large strains. In other words, as the slope of the plastic regime is decreased past $35\,\%$ FVF, for optimal reinforcement at high strains the filler loading should be lower than $35\,\%$. Whilst the distribution of coordination families as a function of FVF observed in Figure 3.3.5 provides a snapshot of the organisation of the filler–polymer network at only $0\,\%$ strain, even this static picture enables insightful observations about how the details of the unstrained polymer–filler network correlates with and determines the nature of the dynamic stress-strain response. However, for a more detailed understanding of the

molecular mechanisms of mechanical deformation, it is necessary to study the dynamical evolution of the polymer–filler network as it undergoes strain.

3.3.4 Coordination during straining

The calculation of the RDF is performed similarly to the static case, but adapted to be computed dynamically during the straining of the structures. The only difference with the static case is that the averaging at a given strain is performed on a single snapshot at that strain, rather than over 50 snapshots. This is done to capture the instantaneous distribution of polymer chains and filler particles. As in the static case, the integrals of the peaks of the RDF are averaged over eight structures from independent runs of the straining process. The large number of beads in our model, as opposed to previous work in the literature [200], results in a higher number of filler particles at a given FVF. This translates into a well-converged RDF even without averaging over multiple snapshots, with the only exception being the lowest FVF (8.8 %, 100 filler particles). As a result, the instantaneous RDF, and hence the filler–polymer network structure, can be captured dynamically during the straining process. Figure 3.3.6 shows the distribution of the coordination families in the system up to 100 % strain, and for different FVFs. To aid the interpretation of these results, the stress-strain response corresponding to the same FVF is superimposed. In Figure 3.3.6, up to small strains of the order of $\sim$5 %, the partition of the coordination families stays approximately constant. This observation holds true for all FVF and it indicates no major rearrangement in the filler–polymer network. This explains and correlates with the initial quasi-elastic regime observed in the stress-strain curves at all filler loading. The main qualitative differences in the mechanical response, i.e. the appearance of a yield drop and the weakening of the plastic regime observed in Figure 3.3.3, are now discussed in light of the dynamical repartition of the coordination motifs.

Yield drop. As previously observed from Figure 3.3.3, a yielding phenomenon is absent in structures with FVF$\leq$27 %, while it characterises all the mechanical responses for structures with FVF$>$31 %. Figure 3.3.6 shows very different evolutions of the coordination families during the uniaxial straining for structures with different filler

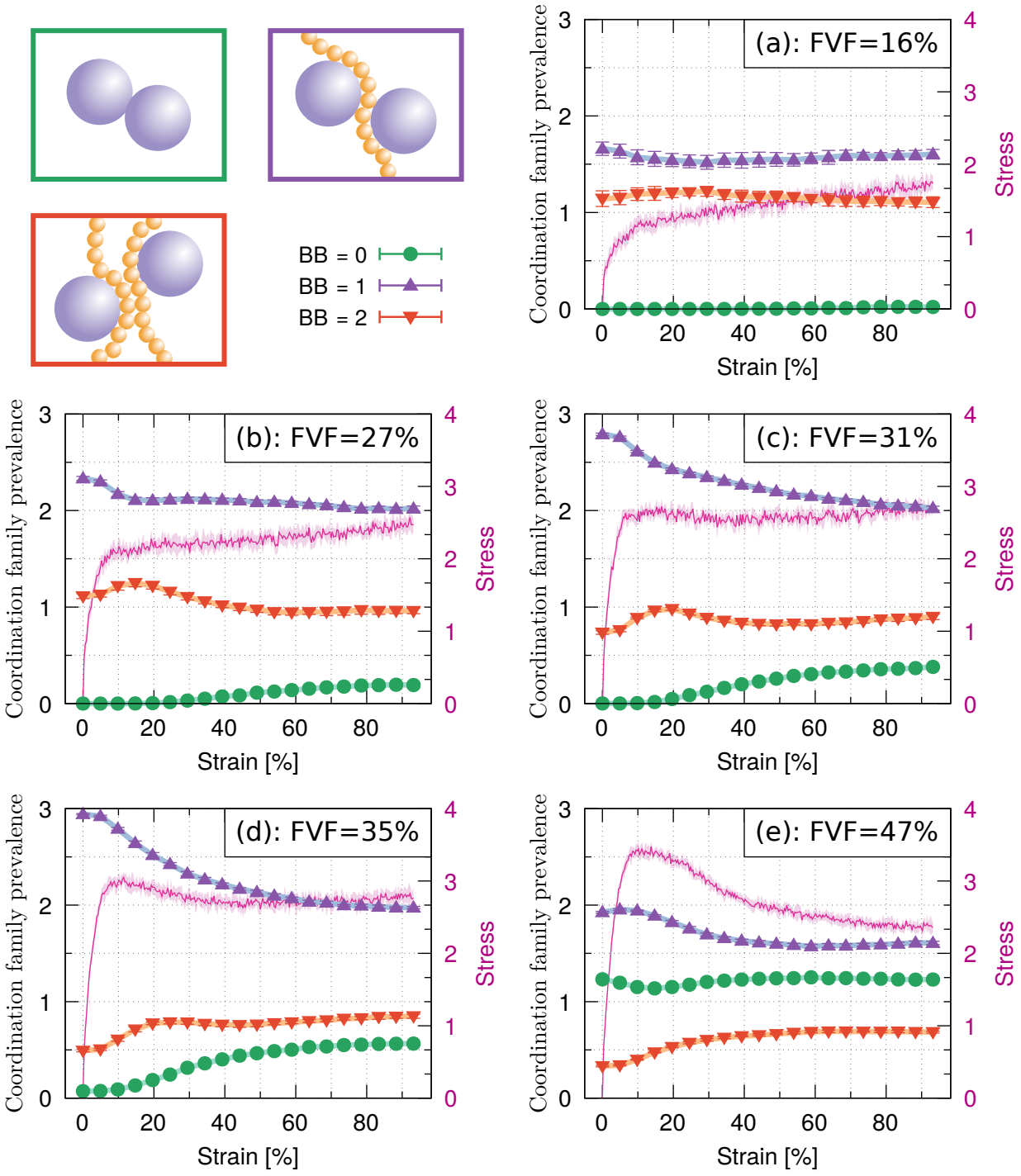


Figure 3.3.6: Prevalence of the coordination family obtained by integration of the filler–filler RDF at different FVFs and straining. The error bars are the standard deviations among eight independently generated structures.

loading. At FVF smaller than 27 %, BB = 1 remains approximately unaltered in terms of both the absolute prevalence and in its contribution relative to BB = 0, 2. On the other hand, at 31 % FVF, BB = 1 decreases with strain (see Figure 3.3.6(c)). For BB = 1, a polymer chain is the only mediator between two filler particles and it experiences attractive interactions from both fillers. Upon straining, stress builds up until such a configuration breaks and the polymer chain remains attached to one of the filler particles. The depletion of the BB = 1 family translates into a higher prevalence of less energetically constrained structures, BB = 0, 2, causing the appearance of a yield drop. In other words, to observe a yield drop phenomenon, there needs to be a mechanism that results in a facilitated means of rearrangement of the polymer–filler network once the maximum stress is achieved, and this is exactly what a reduction of BB = 1 in favour of BB = 0, 2 brings to the system.

Plastic weakening. For FVFs greater than 31 %, a weakening of the plastic regime is observed in Figure 3.3.3. The depletion of the BB = 1 family during the straining process results in an increased number of fillers in direct contact. Greater fractions of the energetically weakest family, BB = 0, increasingly undermine the mechanical response of the structures. This culminates in the observed mechanical weakening of the plastic regimes for FVFs exceeding 35 %.

Persistence and average coordination

A quantity called "persistence" is introduced, which is defined as the fraction of beads coordinating a filler that remains the same between two consecutive snapshots of the structure during the straining procedure. In other words, a persistence of 1.0 for a given filler particle at a given snapshot implies that the local coordination around the filler did not change from the last snapshot. If a bead is within $R_F + \sigma = 3\sigma$ from the centre of a filler, it is marked as coordinating. Let G_n^i and G_{n+1}^i be the sets containing the indices of the beads coordinating filler i at straining step n and $n + 1$, respectively. Then the persistence for filler i at straining step $n + 1$, $\mathcal{P}_{n+1}^i$, is defined as in Equation 3.8.

$$\mathcal{P}_{n+1}^i = \frac{G_n^i \cap G_{n+1}^i}{|G_n^i|}. \tag{3.8}$$

Figure 3.3.7 summarises the persistence value as a function of straining for each of the 1200 fillers separately for a representative structure with 47 % FVF. There are two

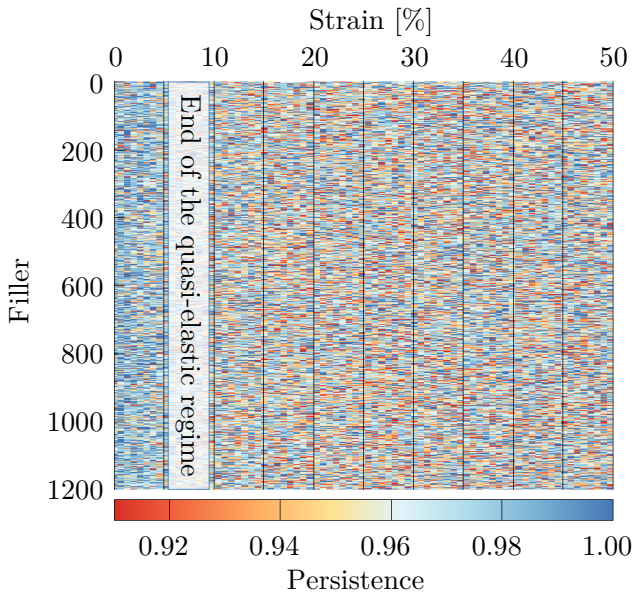


Figure 3.3.7: Persistence of each of the 1200 fillers in a 47 % FVF structure as a function of strain. This particular structure is taken as representative as all structures show the same locality of rearrangements and decrease in persistence. The other plots corresponding to the remaining seven 47 % FVF structures are presented in Appendix C.

important features observed in Figure 3.3.7. First, despite being rare, regions with a persistence ∼91 % can be found for strains lower than approximately 5 %. This highlights that, even in the so-called quasi-elastic regime, sporadically a few fillers alter their coordination environment. The non-negligible alteration of the coordination around some filler particles prevent us from defining as "elastic" the region of the stress-strain curve with strain lower than ∼5 %. In other words, while the system does not undergo substantial network rearrangements, as observed from Figure 3.3.6, local structural modifications are present, hence the "quasi" used to define the quasi-elastic regime. For strain values greater than 5 % in Figure 3.3.7, i.e., after the quasi-elastic regime, rearrangements in the coordination are more common and are experienced by a significant fraction of the filler particles. Second, at all straining, no long segments with

persistence value consistently lower than ∼91 % are observed. This indicates that local rearrangements around a given filler particle do not last longer than a few straining steps. Once the local environment around a filler is altered, the stress is passed in the network to other filler particles that then undergo similar transitions.

With the aim to better understand how the persistence evolves throughout the straining resulting in the appearance of the yield drop for certain FVFs, the average persistence value across all filler particles for a given structure and strain is computed. At a given FVF and straining, the average and standard deviation across all eight structures is computed and reported in Figure 3.3.8.

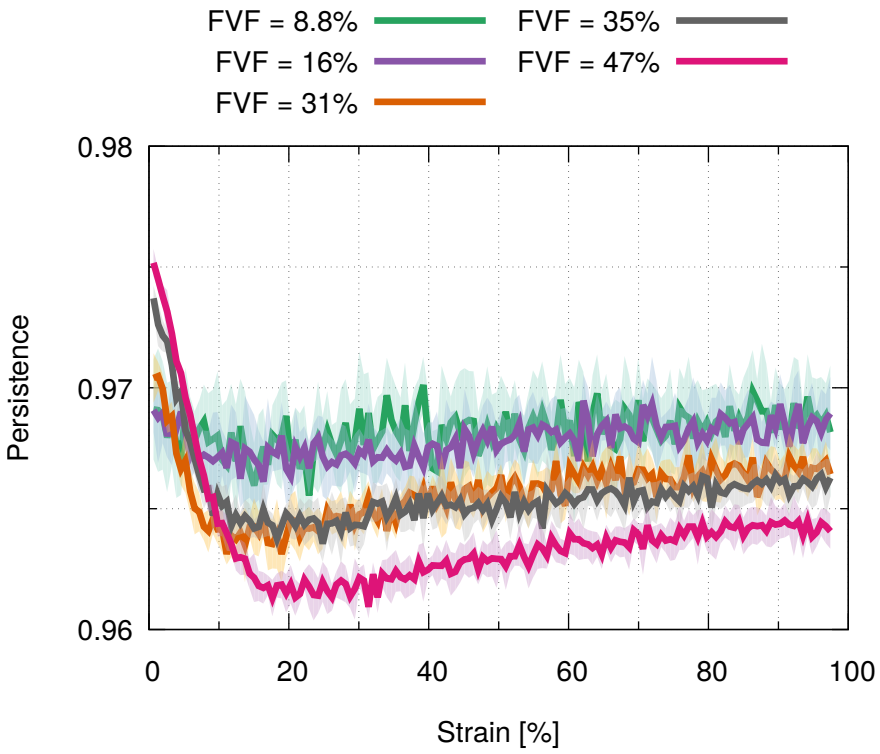


Figure 3.3.8: Average persistence value across all filler particles at a given FVF as a function of the strain.

The average persistence for 8.8 % and 16 % FVF stays roughly constant at around 97 %, indicating small changes in the specific beads responsible for coordinating. The persistence for strain values lower than 5 % is observed to increase for increasing FVFs,

indicating the network is stabilised by the increasing number of BB $= 1$ present in the structures, Figure 3.3.6. This correlates with the observed reinforcement of the quasi-linear regime for increasing FVFs. For the case of 31 % FVF and beyond, the average persistence decreases sharply in the range of straining from 0 % to 20 %. Its relatively rapid decrease at low strains* further clarifies the appearance of the yield drop since it reduces the energetic constraints in the systems.

Average and total filler coordination

To further investigate the plastic weakening and the appearance of the yield drop, average and standard deviation on the per-filler bead coordination are computed and reported in Figure 3.3.9. At 8.8 % and 16 % FVF the number of beads coordinating a filler on

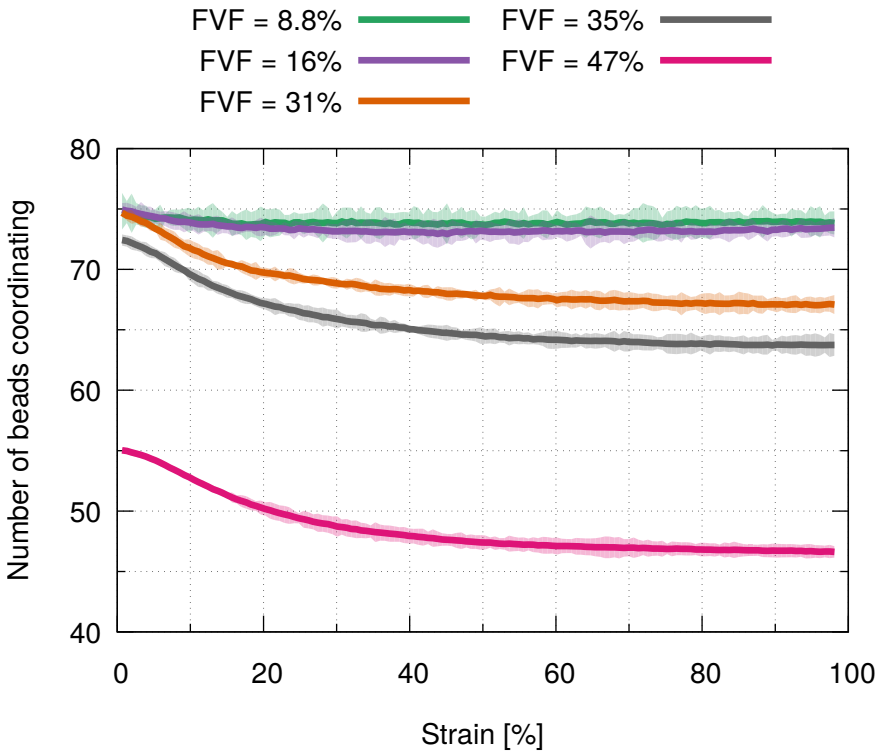


Figure 3.3.9: Average total number of beads coordinating the filler particles at a given FVF as a function of the strain.

*Which culminates in an overall lower persistence at large strains for increasing FVF.

average has a weak dependence on the strain, staying approximately constant at 75. The curves of the average number of beads coordinating the fillers are consistently characterised by an initial drop followed by a plateau for FVFs greater than 31 % resulting in the loss of eight coordinating units by 100 % strain, but a key difference arises between 31 % and 35 % FVF: the absolute average coordination is reduced. A lower average coordination signifies a weakened network, hence explaining the decrease in the slope of the plastic regime observed for structures with FVF greater than 35 %. This observation is consistent with the increasing prevalence of BB = 0 for FVFs greater than 31 % observed in Figure 3.3.5. A higher number of filler particles in direct contact results in a lower fraction of the surface of the filler available to interact with the beads from the polymer network.

To understand why the quasi-elastic regime is monotonically reinforced, the maximum stress before the yield drop, calculated from the stress value at 10 % strain, as a function of the total number of filler–polymer interactions is shown in Figure 3.3.10. Despite the abundance of BB = 0 in the range between 35 % to 47 % FVF and, hence, the

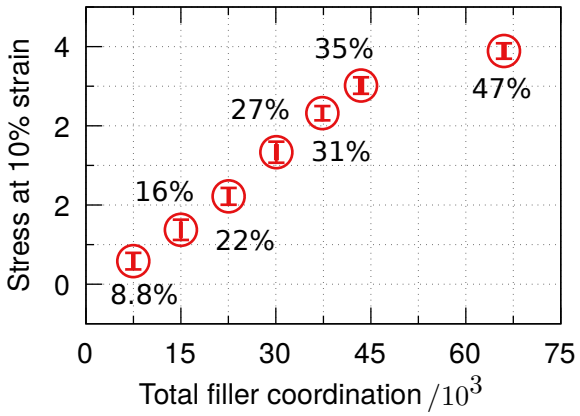


Figure 3.3.10: Stress recorded at 10 % strain versus total bead coordination of the fillers. Both values are averaged over eight independently-generated structures and the error bars indicate the standard deviation in that set.

lower average coordination observed in Figure 3.3.9, the total number of polymer beads interacting with filler increases thanks to the overall greater number of filler particles, resulting in a higher stress value at 10 % strain. Moreover, up to 35 % FVF, the maximum

stress is linearly related to the total number of coordinating beads. The deviation from the linear relationship observed for 47 % FVF can be correlated with the relatively high fraction of BB = 0 present in the structures, which causes significant weakening of the system.

Total bond energy

Finally, the total bond energy throughout the straining is computed for all FVFs. The average and standard deviation reported in Figure 3.3.11 are computed on the set of structures with the same FVF. For the sake of clarity, a rigid offset has been applied to the

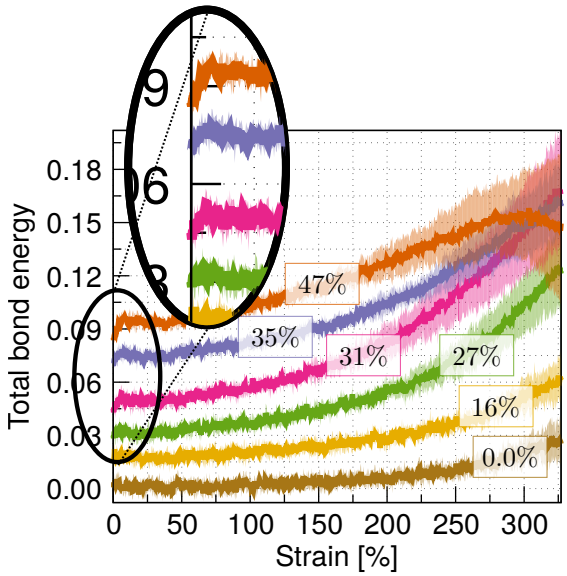


Figure 3.3.11: Total bond energy as a function of the straining in the structures at different FVF. The shade around the solid lines represent the standard deviation among eight structures with the same FVF. For the sake of clarity, the curves have been rigidly offset so that the minima of the curves are equally spaced in the y direction.

curves so that they may be more easily compared with one another in the same plot.

An increase in the total bond energy of the system for strains lower than 10 % is observed for the same structures that exhibit a yield drop, i.e., for FVFs greater than 31 %. On the other hand, the lightly-filled structures (FVF$<$27 %) do not present any

statistically-significant increase in the total bond energy and, coincidentally, no yield drop is observed. The statistical significance of the rise in the total bond energy is determined by comparing the absolute increase to the standard deviation amongst eight structures for strain values lower than 50 %. The storing of elastic energy in the bonds* of the system is a reflection of the lower contribution of BB = 2 to the total coordination at equilibrium, Figure 3.3.5. BB = 2 structures experience weaker energetic constraints as opposed to BB = 1 and, as a result, they can be more easily disturbed without requiring bond stretching.

The polymer network has, on average, one cross-link per chain, and therefore it cannot be indefinitely strained without inducing bond stretching. As a result, the total bond energy increases even for the unfilled polymer systems, black curve in Figure 3.3.11. This effect is present at all FVFs since it is a property of the bare polymer network, however, its role in determining the stress-strain response for strains greater than 100 % can be overcome by the appearance of the energetically weak BB = 0 structural motifs in the system at FVFs greater than 35 %, Figure 3.3.5. Consequently, the appearance of BB = 0 motifs, which act as nucleation points for mechanical failure due to their hard-sphere interaction, is associated with a reduction in both the slope of the total bond energy, Figure 3.3.11, and the stress-strain response at high strains, Figure 3.3.3, and hence a weakening of plastic hardening at higher FVFs.

3.4 Summary

Polymer nanocomposites are already widely used in technological applications in a variety of fields, yet a molecular understanding of their effects would lead to improved properties and, ultimately, cost-cuttings. With the use of a coarse-grained molecular dynamics model, in this chapter I investigated the microscopic origin of mechanical reinforcement in PNC. This investigation highlighted the following main points.

First, I observed qualitatively different behaviours in the mechanical response as a function of the number of filler particles inserted in a structure. Weakening of the plastic

*This stretching is, most likely, not shared among all bonds in the system, but localised to specific spatial regions where BB = 1 prevails.

regime for "high enough" FVFs is observed in agreement with previous studies [200]. However, in contrast with previous reports [200], the appearance of a peak in the stress-strain response between the quasi-elastic and plastic regimes is not limited to high polymer-filler interactions, but it can result from specific network features that depend on the number of fillers in the structure.

I proceeded by highlighting how different filler–polymer coordination motifs stem from the FVF in the structure and how they evolve throughout uniaxial straining. The evolution of the different features of the filler–polymer network is linked to the qualitatively different stress-strain response observed. In particular: 1. the presence of a yield drop is intimately related to the sudden depletion of BB $=1$ during the straining in favour of BB $=0, 2$, which have lower energy barriers to flow and rearrange themselves. 2. The maximum achievable reinforcement at 10 $\%$ strain has an increasing linear dependence with the total number of polymer bead-filler interactions up to a FVF of 35 $\%$. At higher filler loadings, the presence of the BB $=0$ coordination family undermines this relation, which deviates from its linearity. 3. The plastic regime of structures with FVFs exceeding 35 $\%$ is weakened as opposed to lower FVFs by the increasing relative contribution of BB $=0$. 4. The maximum achievable reinforcement for the plastic regime is obtained in concomitance to the peak in the relative prevalence in the system of the BB $=1$ motif.

Effectively, this work remarks the importance of controlling the dispersion state of the fillers introduced in polymer matrix for mechanical applications by providing the microscopic origin of the qualitatively different features observed in the stress-strain response as a function of different filler-polymer coordination motifs. The insights gained from this research can be used to help the design of PNCs and to better understand the microscopic origin of mechanical reinforcement.

4

Nanoparticles as Universal Soft Matter Glue

Nanoparticles have been recently shown to act as universal glues for both synthetic and biological polymers, providing a tuneable, cheap and general solution to the centuries-old problem of sticking soft materials together. The design of new adhesive solutions based on this platform, however, requires understanding of how nanoparticles' and polymer' design parameters concur to determine the final adhesion strength. Here, coarse-grained (CG) modelling and molecular dynamics (MD) simulations are used to investigate such link. The main result shows that the adhesion is clearly influenced by the way nanoparticles (NPs) organise at the interface and how this results in strong non-monotonous reinforcing behaviour depending on the concentration of NPs and their mutual interactions. These findings represent an important step towards rationalising this new class of NP-based adhesives.

4.1 Introduction

Developing the perfect adhesive to stick two materials together represents an important technological challenge throughout materials science. Polymers are often the primary choice thanks to their stress dissipation properties, their ability to adapt to different surface morphologies and their extremely low manufacturing costs. Given their exceptional properties as adhesives, it is peculiar that finding a good adhesive for

polymers has proven rather difficult. Especially in the case of polymer gels, this issue has been typically tackled on an *ad-hoc* basis via the design of smart but complex molecular glues [67, 68].

Recently, Rose *et alia* have shown that an elegant and general solution to this problem is to exploit the ability of NPs to form multiple and reversible bonds with polymers [69]. In particular, these authors showed that painting the surface of different types of both synthetic and natural polymers with NPs allows them to strongly stick at room temperature without the need of any further treatment. Although a simple solution, there are still various parameters of the system that must be designed in order to provide good adhesion, e.g., chemistry, size, and concentration of NPs.

For instance, the chemistry of the NP must be compatible with that of the polymer, in other words, there should be a net attraction between the monomers and the NPs. Another parameter that have been speculated to play an important role is the size of the NPs [69, 207]. In this case, optimal adhesion is thought to occur, based on scaling principles from polymer physics [208], when the diameter of the NP is comparable to the mesh size of the polymer. That not all choices of parameters lead to adhesion is well exemplified by the fact that, as shown in [209], non-monotonic behaviours in adhesion versus concentration of the NPs are experimentally observed. In certain cases, adhesion lower than that of the bare polymer surface can be observed. More in general, powders like talcum*, where a poly-disperse distribution of particles of multiple size are present, have actually been used to prevent polymeric surfaces from sticking [210]. Overall, the experimental evidence points to the fact that NPs-mediated adhesion only happens within a certain range of parameters, but identification of these sweet spots is everything but trivial, especially considering that various non-monotonic behaviours are observed.

In this chapter, MD computer simulations are performed to shine light on this issue†. With the use of a CG model, the tearing of an interface between two permanently cross-linked polymer networks, which adhere due to NPs adsorbed on their surface, is studied. The stress-strain curves as a function of polymer–NP strength of the interaction,

*Clay mineral made of hydrated magnesium silicate: $Mg_3Si_4O_{10}(OH)_2$.

†These simulations concentrate on the case of a polymer in bad solvent conditions, i.e., the network is in a collapsed state.

size as well as the planar concentration of the NPs are investigated, and the trends in the adhesion strengthening analysed. The use of MD simulations allows us to establish a link between macroscopic behaviours and microscopic details of the systems, which is used to develop a simple analytical model to summarise the findings into a ready-to-use rule-of-thumb for the design of polymer adhesives.

4.2 The model

Following the procedure detailed in subsection 3.2.2[*], eight independently-generated structures, having zero fillers and four cross-links on average per chain, are created as a starting point for this investigation. These structures represent a polymer in so-called bad-solvent conditions, in other words, the polymer network is in a collapsed state. Figure 4.2.1 shows an example structure right after the initial generation, (a), and after the cross-linking and equilibration, (b). The following further modifications of the structures have the aim of introducing two surfaces and inserting in between them NPs with different size, polymer-NP interaction strength, and number density:

1. All bonds crossing the plane $z = a$, where $a = (Z_{\text{low}} + Z_{\text{high}}/2)$ (Z_{low} and Z_{high} being the lower and upper bound of the simulation box in the z direction, respectively) is the middle of the box in the z direction, are removed, effectively cutting the structure in two halves. The force-field information is amended accordingly.

2. The two halves are separated and spherical NPs are inserted in-between. The separation is set to be $s = 7R_{NP}$[†], where R_{NP} is the NP radius, Figure 4.2.1(c). The NP coordinates are randomly chosen from the empty slab created in-between the two polymer halves. The number of particles inserted is controlled by imposing the ratio between the area obtained by projecting all the particles onto the

[*] The model used here also inherits the force-field, see section 3.2 for functional form and parameters.

[†] The minimum distance between the two polymer halves required for a successful insertion is twice the radius of the particles. A larger separation is adopted for two reasons. First, this allows for the insertion of a number of particles higher than the perfect packing at the interface. Second, it avoids stagnation of the insertion routine, which might result from consecutive failed insertions.

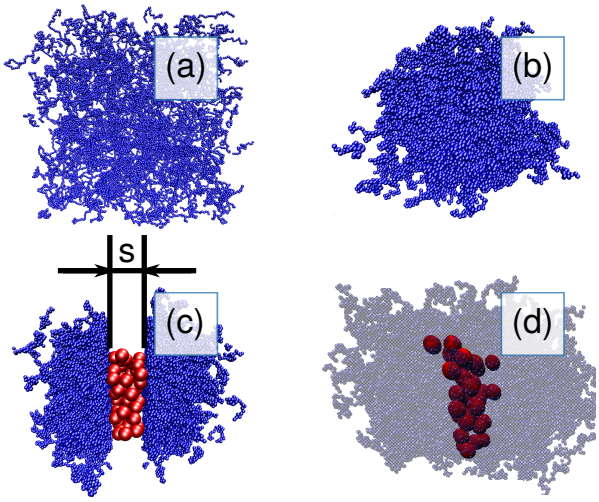


Figure 4.2.1: Main steps of the structure generation process. (a) 1000 chains each 30 beads long placed in a large volume, subsection 3.2.2. (b) The structure is equilibrated, cross-linked and equilibrated again. (c) All bonds crossing the plane perpendicular to the z axis and passing through the centre of the box are cut and the two halves separated by $s = 7R_{NP}$. (d) The structure is re-equilibrated. All the structures pictured here have unwrapped coordinates.

interface and the area of the interface; we call this ratio PA. In this work PA ranges from 0.0 (no particles) to 1.2.

3. The structures undergo an equilibration routine equal to the one outlined in Table 3.2.2. The resulting structure is shown in Figure 4.2.1(d)*.

Once the last equilibration is performed, the structures are strained at a constant strain rate along the z axis in the $\mathrm{NTL}_z\sigma_{xx}\sigma_{yy}$ ensemble and σ_{zz} is computed, see Figure 4.2.2. Details on the straining procedure can be found in chapter 3. In summary, the reduced temperature and stresses perpendicular to the straining direction are kept constant at $T = 1.0$ and $\sigma_{xx} = \sigma_{yy} = 0$, respectively, and the straining rate is kept constant at 3.27 % per unit time. All the MD simulations are performed using large-scale atomic/molecular massively parallel simulator (LAMMPS), and timestep of $\delta t = 0.001$ is used to integrate

*Effectively, this is the third equilibration routine that a single structure undergoes, the first one being right after the structure generation at low density and the second one after the dynamical cross-linking.

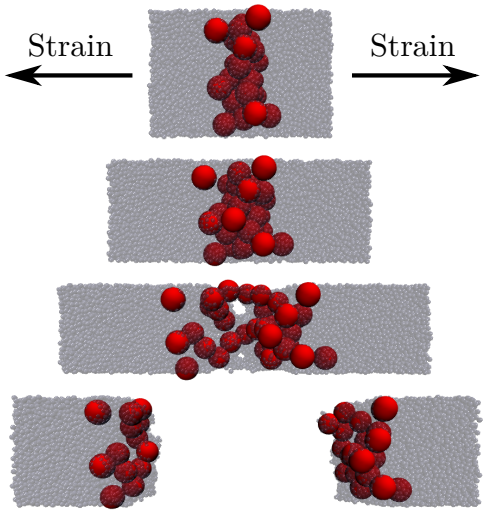


Figure 4.2.2: Evolution of a structure. The red spheres represents the nanoparticles while the polymer chains are made partially transparent for clarity. From top to bottom: the cross-linked, reinforced with nanoparticles, and equilibrated structure is ready to undergo the straining procedure. The NPs act as glue between the two polymer networks improving the overall mechanical properties. For larger strains the system starts to fail; voids and cavities weaken the mechanical response of the system. Finally, complete mechanical failure is reached and two interfaces coated with nanoparticles are obtained. The straining axis corresponds to the z direction, Figure 3.2.5, which is the direction normal to the slab where the nanoparticles are placed.

the equation of motions. The Nosé-Hoover formulation for barostat and thermostat [143, 144, 146], as implemented in the LAMMPS code [140], is used throughout this work to control pressure and temperature, respectively.

In this study, the contribution of NP size, NP-polymer interaction strength, and PA to the mechanical reinforcement of the interface is disentangled. The NPs investigated have a radius of $R_{NP} = 1, 2,$ or 4σ, an interaction strength with the polymer of $\varepsilon_{\text{Bead-NP}} = \varepsilon_{\text{BN}} = 1, 2,$ or 5ε, $\varepsilon_{\text{Bead-Bead}} = \varepsilon_{\text{BB}} = 1\varepsilon$, and $PA = 0.0, 0.4, 0.8,$ or 1.2. Eight structures for each combination of the aforementioned parameters are independently generated.

It is worth restating that the cubic simulation boxes have periodic boundary conditions. Also, the total number of polymer beads is constant, 30 000, while the number of filler particles varies depending on radius and PA. As a result, the total volume

of the simulation box at equilibrium* varies between $33.6(1)\ k\sigma^3$ and $52.7(1)\ k\sigma^3$ for $(R_{NP} = 1.0, PA = 0.0)$ and $(R_{NP} = 4.0, PA = 1.2)$, respectively. The reported volumes and standard deviations are the ensemble average over eight independently generated structures. As $(R_{NP} = 1.0, PA = 0.0)$ corresponds to the unfilled case, it is worth stressing that the difference with the unfilled case in chapter 3, where the volume of the unfilled structure was $34.4(1)\ k\sigma^3$, is due to the larger number of cross-links. In fact, the structures presented in this work possess four times as many cross-links compared to the structure in chapter 3.

4.3 Results & Discussion

4.3.1 NPs profile

With the aim of characterising the structures and understanding the distribution, along the z axis, of the NPs and polymer beads, density profiles are computed for all the combinations of parameters. An NPT MD simulation, where $T = 1.0$ and $P = 0.0$, is run for a total of 50 000 timesteps, and the density values are recorded as follows. The simulation box is subdivided in slabs, as wide as the box itself in the x and y directions, and with thickness σ in the z direction. For every slab, the filler and polymer bead number density is recorded every 100 timesteps. This produces a total of 500 values, on which the average and standard deviation are computed.

Figures 4.3.1 and 4.3.2 report the results for a few of the combinations of the studied parameters, with $R_{NP} = 1\sigma$ in the former, and $R_{NP} = 4\sigma$ in the latter, in particular. For each colour, the solid line represents the average value, while the shaded area indicates the standard deviation among the eight structures sharing the same set of parameters. The general trend is that for higher PA and lower strength of the NP-polymer bead interaction, $\varepsilon_{\text{NP-bead}}$, the NPs tend to segregate onto the two surfaces.

A note-worthy observation is that, while for $R_{NP} = 1\sigma$, $PA = 0.8$, and $\varepsilon_{\text{NP-bead}} = 5$ the NPs diffuse into the bulk of the polymer network, for the same density and interaction strength but $R_{NP} = 4\sigma$ two NPs layers are present. This is attributed to the

*Hence, before the straining is performed.

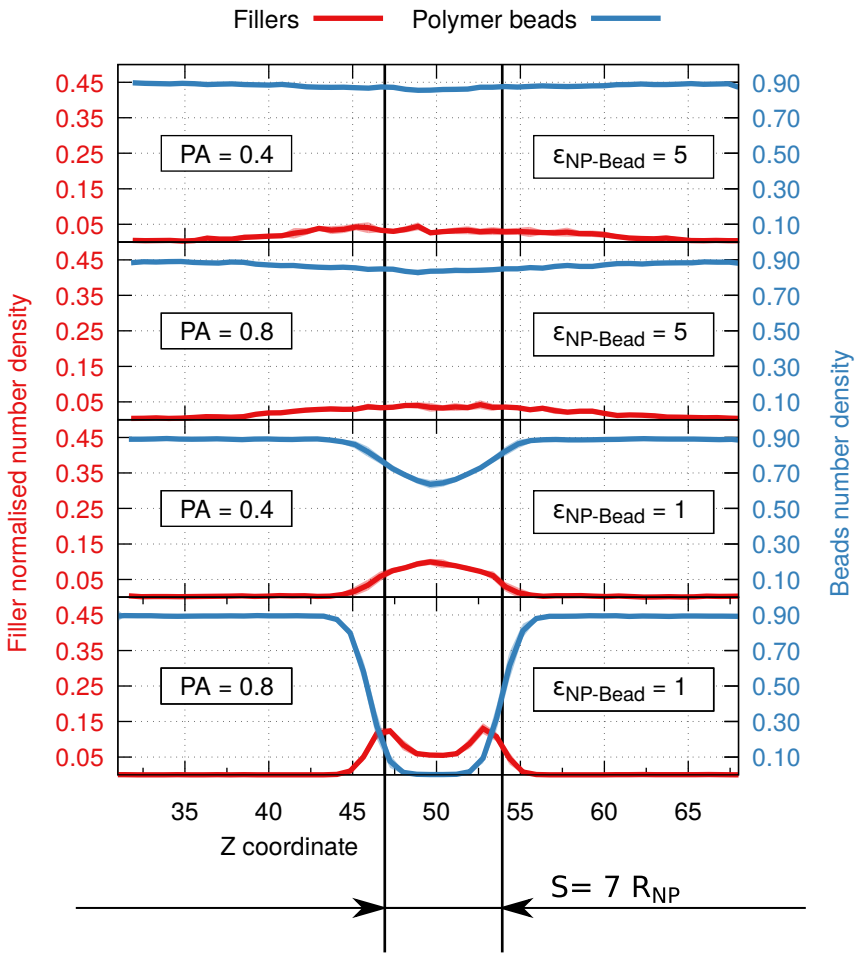


Figure 4.3.1: NPs ($R_{NP} = 1\sigma$, red curve and y_1 axes) normalised number density and polymer beads (blue curve and y_2 axis) number density profiles along the z axis. The values are obtained by averaging on slabs as wide as the simulation box in the x and y direction, and thick 1σ in the z direction. Temperature and pressure are kept constant at $T = 1.0$ and $P = 0.0$, respectively, for a NPT MD simulation 50 000 timesteps long. The standard deviations are also plotted as shaded area around the curves, however, they are too small to be appreciated on the scale of this plot.

difference in size of the NPs. The polymer chains are composed of 30 beads, with an average cross-link density of four cross-links per chain, meaning that, on average, cross-link bonds are ten beads apart. Figure 4.3.3 shows an example of a small polymer

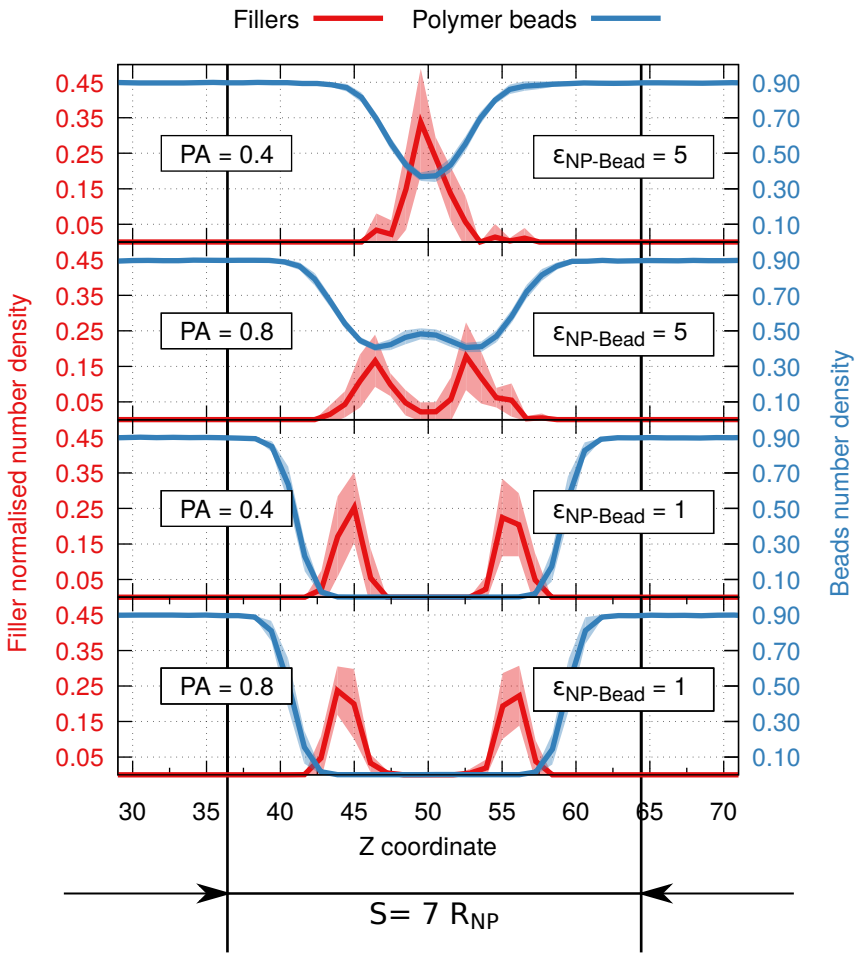


Figure 4.3.2: NPs ($R_{NP} = 4\sigma$, red curve and y_1 axes) normalised number density and polymer beads (blue curve and y_2 axes) number density profiles along the z axis. The values are obtained by averaging on slabs as wide as the simulation box in the x and y direction, and thick 1σ in the z direction. Temperature and pressure are kept constant at $T = 1.0$ and $P = 0.0$, respectively, for a NPT MD simulation 50 000 timesteps long.The standard deviations are also plotted as shaded area around the curves.

loop* that exists in the polymer network. Such a loop is 20 beads long, hence it has a circumference of 20σ, therefore greatly hindering the movement of spherical objects with radius greater than $\sim 3.2\sigma$. As a result, the NPs with $R_{NP} = 4\sigma$ are "filtered" by the polymer network and confined to the proximity of the surface, while NPs with $R_{NP} = 1\sigma$

*The smallest loop involves only one chain folding onto itself, leading to an even smaller loop.

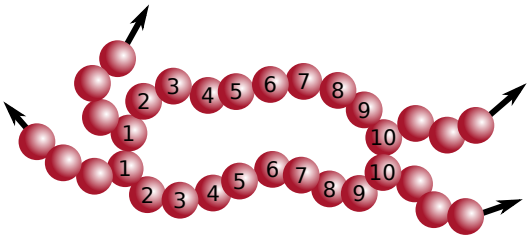


Figure 4.3.3: Example of polymer chain loop that is present in the polymer network.

can diffuse into the bulk with ease[*].

4.3.2 Polymer bead–NP interaction and NP size

Figure 4.3.4 presents the stress-strain response at low density of particles, $PA = 0.4$, as a function of (a,b) the radius of the NPs, and (c) strength of the interaction between the NPs and the polymer beads. This specific value of $PA = 0.4$ was chosen to illustrate the behaviour in a regime where the particle–particle organisation at the interface can be neglected; this effect will be clarified later. It should be noticed that in both (a) and (b), $\varepsilon_{BN} > \varepsilon_{BB} = 1$ hence the chemistry of the NPs is tuned so that there is an energy-driven tendency to adsorb polymer beads on the surface of the NPs. However, in (a) $\varepsilon_{BN} = 2$ whereas in (b) $\varepsilon_{BN} = 5$, and two different behaviours are found.

In Figure 4.3.4(a), NPs are detrimental to the stress-strain response of the system, the more so the larger their size. However, for $R_{NP} = 1\sigma$ (twice the radius of a polymer bead) the system shows almost the same mechanical properties as in the unfilled case; NPs with larger radii weaken the response, both in term of the maximum strain as well as the maximum stress at breakage. On the other hand, when the ε_{BN} is "high enough" as in (b), a non-monotonic reinforcement as a function of particle size is observed. $R_{NP} = 1\sigma$ results in small improvement with respect to the unfilled case, and for $R_{NP} = 2\sigma$ yields the best mechanical response, while for $R_{NP} = 4\sigma$ a moderately weakened curve compared to $R = 2.0\sigma$ is observed, where not only the maximum stress but also the strain at the breakage point are reduced.

[*]While the reported NPs profiles are certainly time-scale dependent, the general idea of this observation is expected to hold true at longer time-scales.

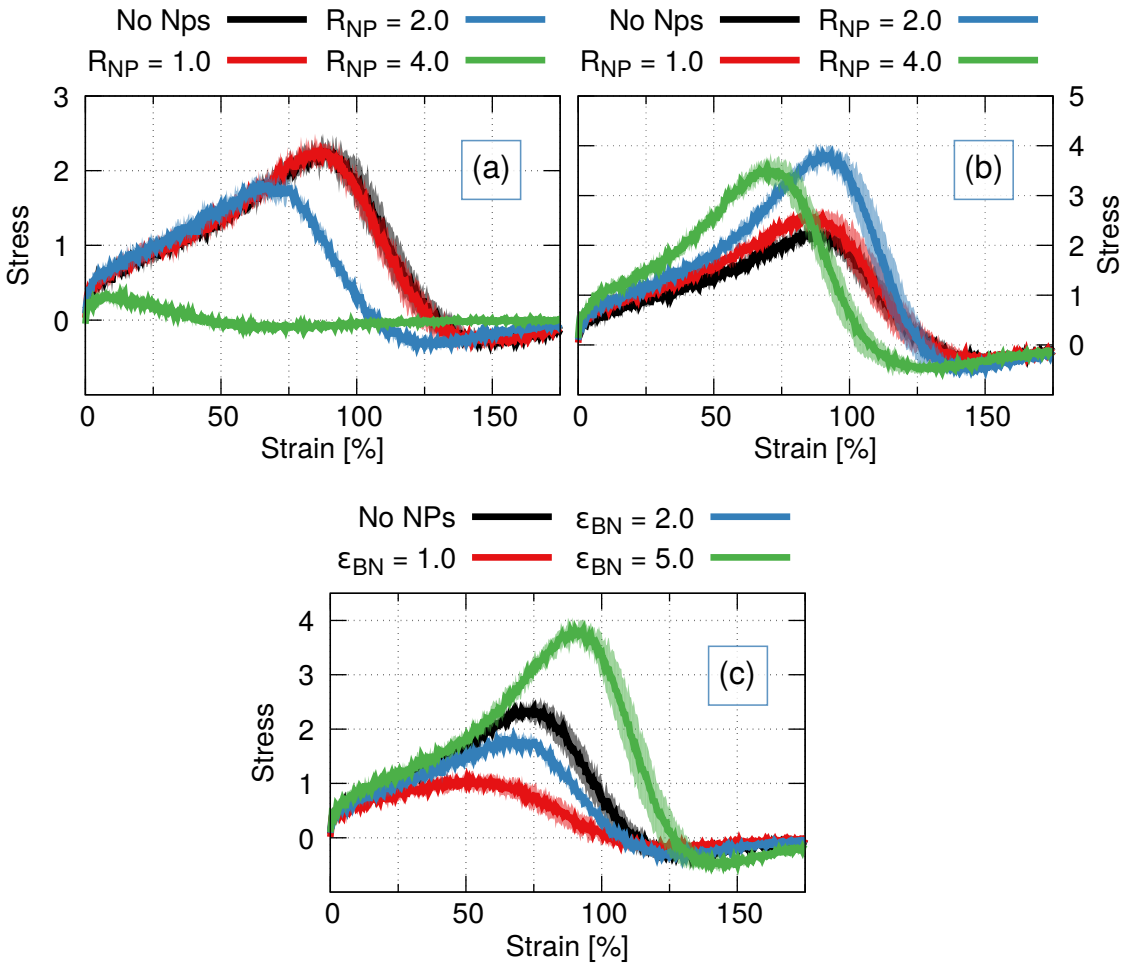


Figure 4.3.4: Mechanical response for different (a,b) NP radius and (c) NP interaction with the polymer beads. The black curve shows the stress-strain for the unfilled case. For both (a,b) $PA = 0.4$ while the polymer bead-NP interaction is set at 2 and 5 for (a) and (b), respectively. In (a) a higher effectiveness of small particles is observed while (b) shows a non-monotonic behaviour as a function of the radius of the NPs. In (c) $R_{NP} = 2\sigma$ and $PA = 0.4$. Note that a weakening of the mechanical response is observed even for a polymer bead–NP interaction exceeding the bead–bead parameter. The shade around each curve represents the standard deviation amongst eight independently generated structures.

Figure 4.3.4(c) helps to further clarify the difference in the results observed between (a) and (b). Purely based on the difference between polymer bead–NP and bead–bead

interaction, stronger adhesion between the two polymer surfaces, as obtained in the green curve for $\varepsilon_{BN} = 5.0$, would be expected for any $\varepsilon_{BN} > \varepsilon_{BB} = 1$, albeit with different magnitudes. However, for a polymer bead–NP strength of interaction twice as strong as the bead–bead one, the system shows a weaker response to the straining action as opposed to the unfilled case.

The results from Figure 4.3.4 show that the polymer bead–NP interaction alone is not a good predictor of interfacial mechanical reinforcement, which instead requires some form of coupling with the size of the NPs. In practice, one needs to consider the fact that although a high polymer bead–NP strength of the interaction can reinforce the polymer–polymer interface, forming this contact also requires the polymer to wrap around the NPs, with subsequent loss of entropy. In general, the latter step requires a positive mechanical work that must be taken into account. Proceeding along these lines, the findings in Figure 4.3.4 are well described by a trivial modification of the model recently presented by Cao and Dobryinin [211]. It is assumed that the interfacial reinforcement is well measured by $W_{\text{reinforce}}$, which is the work required to reversibly separate two polymer networks bridged by NPs compared to the same work for the two bare networks. Hence, the expressions in Equations 4.1 and 4.2 are obtained.

$$W_{\text{reinforce}} = PA\left[\left(\gamma_{\text{B}} + \gamma_{\text{N}} - \gamma_{\text{BN}}\right)\left(\frac{\gamma_{\text{B}} + \gamma_{\text{N}} - \gamma_{\text{BN}}}{G\,R_{\text{NP}}}\right)^{2/3} - 2\gamma_{\text{B}}\right], \tag{4.1}$$

$$\propto PA\left[\alpha\left(\varepsilon_{\text{BN}} - \varepsilon_{\text{BB}}\right)\left(\frac{\varepsilon_{\text{BN}} - \varepsilon_{\text{BB}}}{G\,R_{\text{NP}}}\right)^{2/3} - 2\beta\varepsilon_{\text{BB}}\right]. \tag{4.2}$$

α and β are two proportionality coefficients of order one, and the NPs are assumed to be in the bridging regime [211]. G is the polymer shear modulus. From Equation 4.1 to Equation 4.2 a simple broken-bond argument is used to connect the microscopic interaction parameters, ε_{BN} and ε_{BB}, to the interfacial free-energies γ_i of the polymer, $i \equiv$ B, the NP, $i \equiv$ N, and their interface, $i \equiv$ BN. Although a strict proportionality between ε and γ is a strong assumption of broken-bond models, requiring no surface relaxation compared to the bulk that is surely not true for the polymer, one can safely expect the two to show the same trend (i.e. one is a strictly monotonic function of the

other).

Considering that reinforcement compared to the bare interface is only observed if $W_{\text{reinforce}} > 0$ and the opposite otherwise, Equation 4.2 qualitatively describes all the trends we observe: a lower critical value for the polymer bead–NP interaction parameter, ε_{BN}, below which the interface is weakened rather then reinforced, a monotonically increasing reinforcement as ε_{BN} increases, and the fact that larger particles require stronger interaction energies to show the same reinforcement as smaller ones. A "reinforcement phase-diagram" is included to aid the interpretation of Equation 4.2, Figure 4.3.5. In principle, Equation 4.2 does not explain the

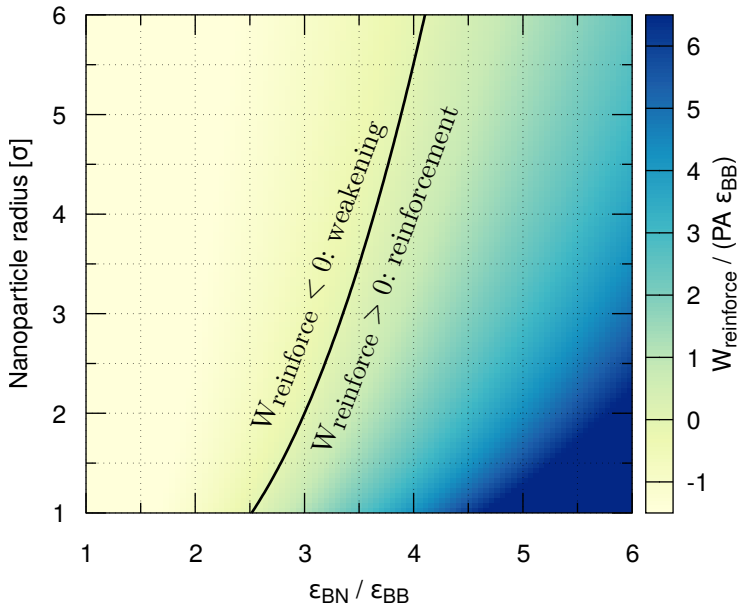


Figure 4.3.5: "Reinforcement phase diagram" in the limit of low NPs surface concentration ($PA \ll 1$), as predicted by Equation 4.2. The colour codes for the work of reinforcement per projected area of the nanoparticles, $W_{\text{reinforce}}/(PA\varepsilon_{\text{BB}})$, as a function of both $\varepsilon_{\text{BN}}/\varepsilon_{\text{BB}}$ and the radius of the NP. The model shows the presence of a size-dependent critical value for the reinforcement of the interface. The values of the constants are set to $G = \alpha = \beta = 1$.

non-monotonic behaviour as a function of size observed in Figure 4.3.4(b). However, the weak positive reinforcement observed for $R_{NP} = 1\sigma$ is thought to be the result of the fact that, due to their size that allows them to easily diffuse through the polymer network,

small NPs do not stay at the interface, but rather move towards the bulk of the polymer, as seen in Figure 4.3.1. These findings are compatible with experimental studies of similar NPs-elastomer systems, where it is shown that, depending on the chemical compatibility, or in other words the interaction strength, of the polymer-NP interaction, NPs can either be used to prevent adhesion, or to actually strengthen it [212, 213].

When the number of inserted NPs is small, i.e. $PA \ll 1$, their interaction can be neglected. In this concentration regime, a single layer of NPs is formed and inserting more of them will monotonically strengthen or reduce the interface binding energy depending on whether or not ε_{BN} is lower or higher compared to a radius-dependent critical value, as described by Equation 4.2. However, a more complex picture arises when the number of NPs is "high enough" that their excluded volume interactions come into play. In this scenario, NPs organisation at the interface plays a crucial role.

4.3.3 High NPs concentrations

Figure 4.3.6 presents the stress-strain curves for different *PA*s and radii of the NPs, $R_{NP} = 2.0\sigma$ and $R_{NP} = 4.0\sigma$ for (a) and (b), respectively. It is worth repeating that *PA* is the *nominal* projected area fraction, in other words, what would be obtained if all the NPs initially inserted at the interface between the two networks remained at the interface. *PA* is thought to be a good indicator since this would be the control parameter in an experiment using NPs as glue, where one can only control the concentration of the NPs solution and, hence, the number of NPs initially deposited on the surface. However, whereas this corresponds approximately to the effective *PA* at the interface when $PA \ll 1$*, for larger values of *PA*, NPs cannot all localise at the interface, producing peculiar effects.

In Figure 4.3.6(a), no statistically significant difference in the mechanical response as a function of the number of inserted NPs is observed. The initial insertion of NPs, corresponding to $PA = 0.4$, leads to a stress at failure almost twice as great as the one corresponding to the unfilled system. However, additional insertion of NPs does not lead to further reinforcement and a plateau is reached. The only observed difference for

*And, especially, for large enough NPs, whose movement is hindered by steric arguments.

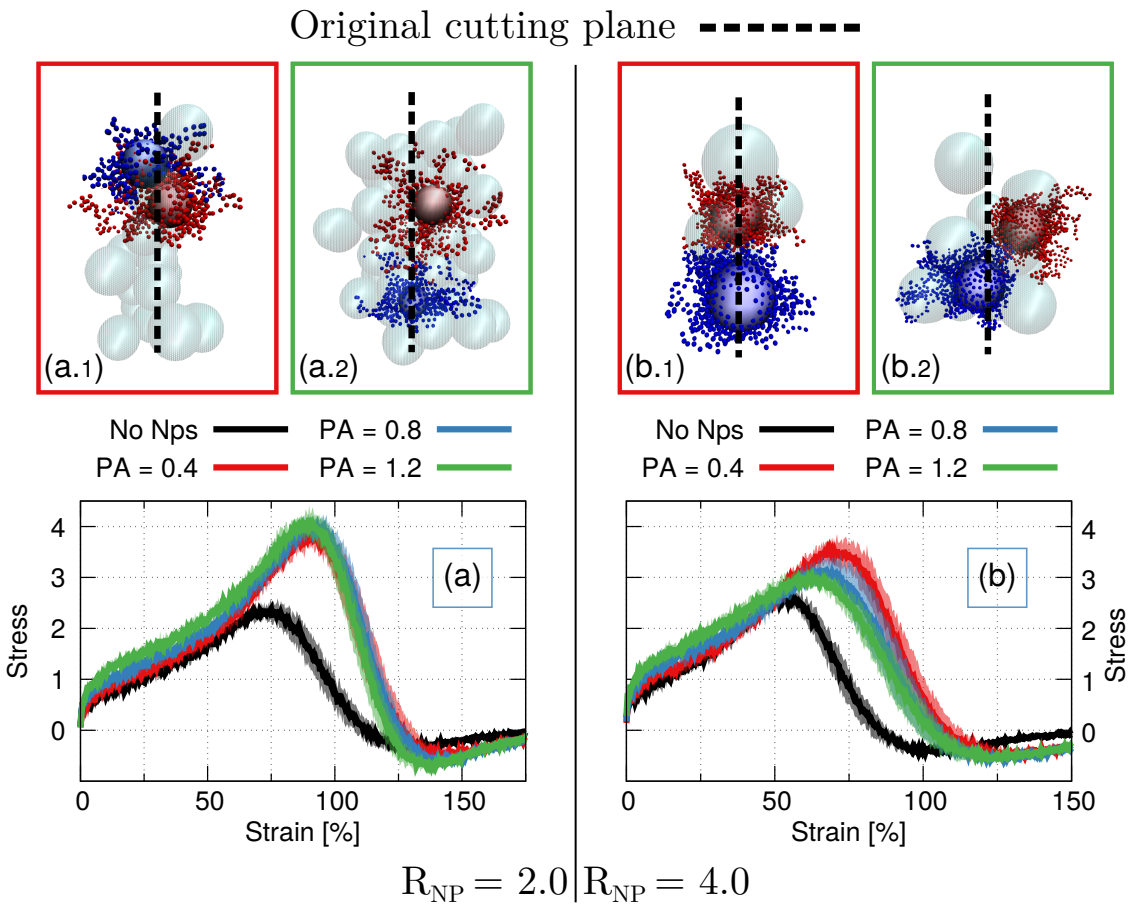


Figure 4.3.6: Mechanical response at strong polymer bead–NP interaction, $\varepsilon_{PN} = 5.0$, for: (a) $R_{NP} = 2.0\sigma$ and (b) $R_{NP} = 4.0\sigma$. The top ($a._{1,2}$ and $b._{1,2}$) MD snapshots present the distribution of NPs between the two polymer networks, the latter not shown for clarity. For each snapshot, two NPs and their coordinating chains are highlighted. The shade around each stress-strain curve represents the standard deviation amongst eight independently generated structures.

different *PA*s is a small increase in the toughness of the plastic hardening regime. To clarify the origin of this plateau, Figure 4.3.6($a._1$) and ($a._2$) present MD snapshots representative of the local environment of the NPs in the structure; the dashed line is placed at the interface between the two polymer networks. In both snapshots two NPs and their coordinating chains are highlighted, whereas the rest of the polymer beads are ignored for the sake of clarity. For both $PA = 0.4$, ($a._1$), and $PA = 1.2$, ($a._2$), on average

the chains coordinating NPs at the interface belong to both networks, i.e., there is no significant coordination predominance from a network from either side of the interface. However, at large values of *PA* not all NPs can sit at the interface and they are pushed away from it[*]. Since these latter particles do not contribute to linking the two networks, the mechanical reinforcement obtained plateaus to the observed value.

Figure 4.3.6(b) presents the same study as Figure 4.3.6(a) but for particles with larger radius, $R_{NP} = 4.0$, which further complicates the observed picture. In fact, the reinforcement plateau reported for smaller radius of the NPs is not reproduced. Instead, increasing the number of inserted NPs above a certain value leads to a *weakening* of the mechanical response. In other words, an optimal reinforcement condition emerges. The inability of NPs with $R_{NP} = 4.0\sigma$ to reach a "good coordination" condition[†] is the origin of the observed non-monotonicity. NPs are trapped at the interface because of their size, larger then the polymer mesh, as shown in Figure 4.3.3. This results in the observed formation of two contiguous layers of NPs for *PA*s that exceed optimal planar packing, impeding an homogeneous chain coordination by both sides of the interface and therefore weakening the stress-strain response. This observation does not hold for $PA = 0.4$, where a single layer of NPs is always present, leading to "good coordination" and, hence, more effective mechanical reinforcement compared to higher *PA* values. Figure 4.3.6$(b_{.1})$ and $(b_{.2})$ present MD snapshots of the NPs with $R_{NP} = 4.0\sigma$ in the structure. $(b_{.1})$ shows a coordination environment similar in nature to the one presented in $(a_{.1})$ and $(a_{.2})$. On the other hand, $(b_{.2})$ highlights the asymmetric origin of the coordinating chains for two NPs.

To further clarify this point, the total average coordination of the NPs by the polymer bead and the persistence are computed. Similarly to subsection 3.3.4, a polymer bead is marked as "coordinating" if its centre is within a distance of $R_{NP} + \sigma$ from the centre of a filler. Unlike in subsection 3.3.4, the persistence here is defined as the fraction of beads coordinating a filler that remains the same as compared to the initial set of coordinating

[*]It should be noticed that for such particles passive diffusion is very slow, hence, once the pressure exerted by other particles decreases as they move towards the bulk, they stop diffusing. This is not true for small particles, $R_{NP} = 1.0$, which can more easily diffuse into the bulk of the polymer.

[†]Meaning the condition where the particles are evenly coordinated from polymer chains belonging to both networks.

beads*. Hence, the persistence at timestep n, $\mathcal{P}_n^i$, is defined as

$$\mathcal{P}_n^i = \frac{G_o^i \cap G_n^i}{|G_o^i|}. \tag{4.3}$$

Where G_o^i and G_n^i are the sets containing the indices of the beads coordinating filler i at straining step o and n, respectively. The results are shown in Figure 4.3.7(a),(b) for average filler coordination and persistence, respectively. All the curves have a similar

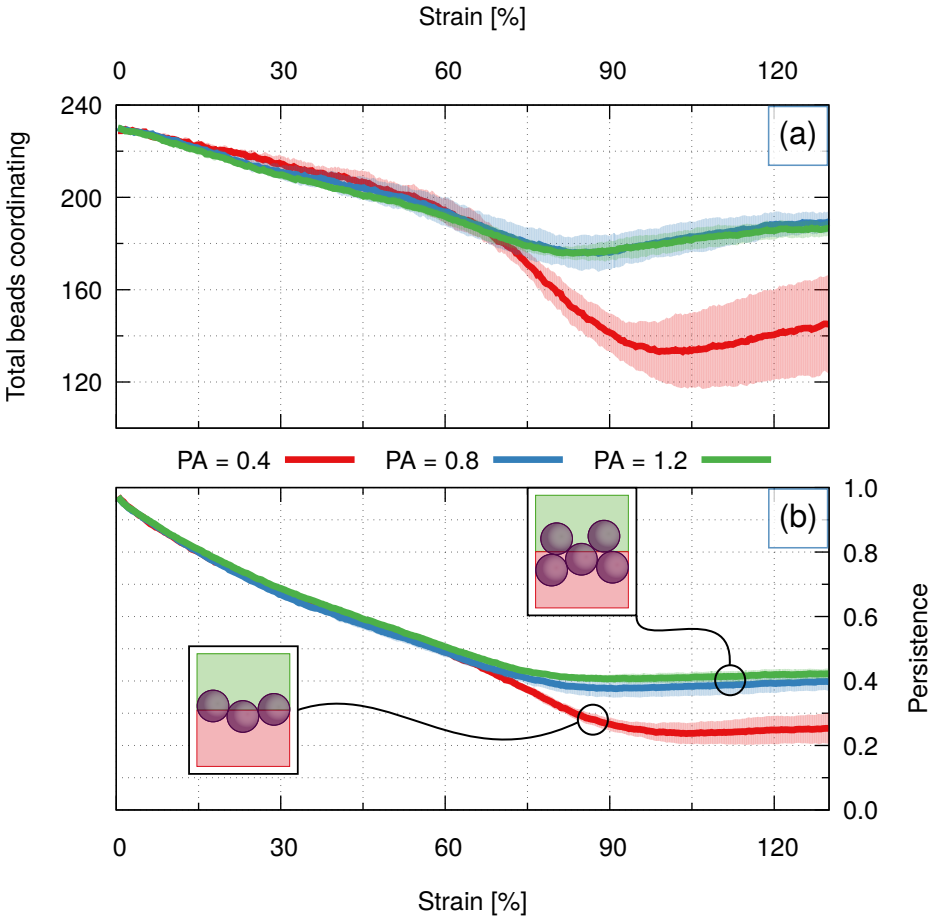


Figure 4.3.7: Total coordination, (a), and persistence, (b), as a function of the straining for PA $= 0.4, 0.8,$ and 1.2, $R_{NP} = 4\sigma$ and $\varepsilon_{\text{NP-bead}} = 5$.

*Unlike what was done in subsection 3.3.4, i.e., where the persistence was computed between two consecutive snapshots to capture the dynamical evolution.

dependence on strain up to a strain value of approximately 70 %, which corresponds to the onset of mechanical failure observed in Figure 4.3.6. After a strain value of 70 %, the decrease in average bead coordination and persistence experienced by $PA = 0.8$ and 1.2 stops. On the other hand, both the average filler coordination and persistence for $PA = 0.4$ keep decreasing, reflecting the need to break a larger number of links since the NPs are in a "good coordination" condition*.

A non-monotonous behaviour in the interfacial adhesion strength as a function of the number of inserted NPs has been very recently observed experimentally by Kim *et alia* [209]. To explain their results, the authors speculated that a layering mechanism might occur in the system. The detailed microscopic picture arising from these CG MD simulations clearly confirms their hypothesis. At the same time, it shines light on the dependence of the mechanical reinforcement of the interface on the size of the NPs. It has been previously speculated by Rose *et alia* [69] that the optimal size of the NPs is close to the mesh size, on the ground that in this case several different network strands adsorb on the same particle, allowing it to act as an effective connector between surfaces. These simulations as well as the analytical model in Equations 4.1 and 4.2 show that different regimes should be considered, depending on the concentration of NPs at the interface. Overall, the understanding gained from a microscopic view of the problem allowed us to help reconcile various different trends observed in these peculiar systems, thereby providing a more complete understanding and helping future designs.

4.4 Summary

Using CG MD simulations, this chapter presents how NPs' properties such as size and strength of the interaction couple together with those of the polymer, controlling their organisation at the interface and thereby affecting their potency as adhesive. The investigation resulted in the following two important findings: 1. The existence, at NPs concentration far away from optimal packing, of a size-dependent threshold in the polymer-NP interaction required to observe any interfacial reinforcement compared to

*Furthermore, a change in the gradient of the two curves is observed, which signals a more abrupt alteration of the coordination environment.

the bare polymer networks. This and other results are qualitatively captured by a simple analytical model, Equations 4.1 and 4.2, derived by adapting an earlier model of Cao and Dobrynin [211]. 2. The presence and the origin of plateauing and non-monotonicity in the mechanical response at high NPs concentrations is explained. In practice, NPs self-organisation in mono- or bi-layers has a direct implication on how the structure reacts under uni-axial strain. Thanks to the CG approach adopted, the results are based on general physics rather than on specific chemistry. This makes the findings qualitative rather than quantitative, but at the same time the trends observed are expected to be more general and not system-specific [214].

5

Li-Bis(trifluoromethane)sulfonimide in Poly(ethylene)oxide

Currently available solid polymer electrolytes for Li-ion cells require significant improvement in ionic transport properties in order to enable their use in high-power batteries. Atomistic simulations are used to model the solid amorphous polymer electrolyte system comprising poly(ethylene)oxide (PEO), lithium and bis(trifluoromethane)sulfonimide (TFSI) anion, exploring the effects of high salt concentrations relevant for applications. Using statistical analysis of ion distribution and transport, the significant effect that salt concentration has on ion mobility is investigated. At practical salt concentrations a previously undetected ensemble of Li-TFSI clusters emerges where Li ions have significantly lower coordination by the polymer, and this results in their significantly lower mobility compared to Li ions coordinated by the polymer. The tendency for Li-anion clusters to be asymmetrical was also observed, with the anions in greater number than Li cations, which may contribute to the low transference number of this material.

5.1 Introduction

The first, crude attempt at an electric carriage was made almost 200 years ago by Scottish inventor Robert Anderson [215], and it was followed by various improvements* that led to a variety of car models over the next few decades. In 1900, a stunning 28 % of the 4192† cars produced in the United States are powered by electricity [219]. However, eight years after, the introduction of mass-produced, price-competitive and petrol-powered model T by Henry Ford [220] marked the beginning of a decline for electric cars and by 1920 they ceased to be a viable option [221]. Electric vehicles fell in a dormant period for approximately 60 years [222, 223], until their sleeping potential was uncovered by a United States Congress-issued bill recommending the use of electric-powered cars to reduce air pollution [222, 223].

Fast-forward to present day, electric vehicles have found renowned interest for mainly two reasons. According to the latest report of the United States Environmental Protection Agency [224], over a quarter of the total greenhouse gas emissions in 2015 can be traced back to the transportation sector, Figure 5.1.1. This includes any means of transportation for people and goods, from private cars to trains, ships, airplanes, and trucks‡. The vast majority of today's vehicles, over 90 % [224], rely on the combustion of petroleum-based fuels such as gasoline and diesel, producing CO_2 as a result. Aside from the environmental reason, over time, the search and extraction of new hydrocarbon reserves faces increasingly harsher and hostile downhole conditions as observed in Figure 2.1.1, increasing the costs and challenges associated with oil production. For these reasons, over the past couple of decades, considerable efforts have been spent trying to solve the central issue of electric-powered cars that even troubled Edison: the battery compartment.

To take electric cars to their heyday, they need to be competitive with current petrol-powered vehicles on essentially two levels: price and practicality. Focusing on the latter, the main concerns orbit around: 1. range of operation, i.e., how far can we drive

*Even Thomas Edison was involved in the mission of creating long-lasting and powerful batteries suited for commercial automobiles [216, 217].

†This is actually the lowest number among the sources I found, the highest being 38 % of 33 842 [218].

‡Over half of the CO_2 emissions of the transportation sector is produced by passenger cars and light-duty trucks only [224].

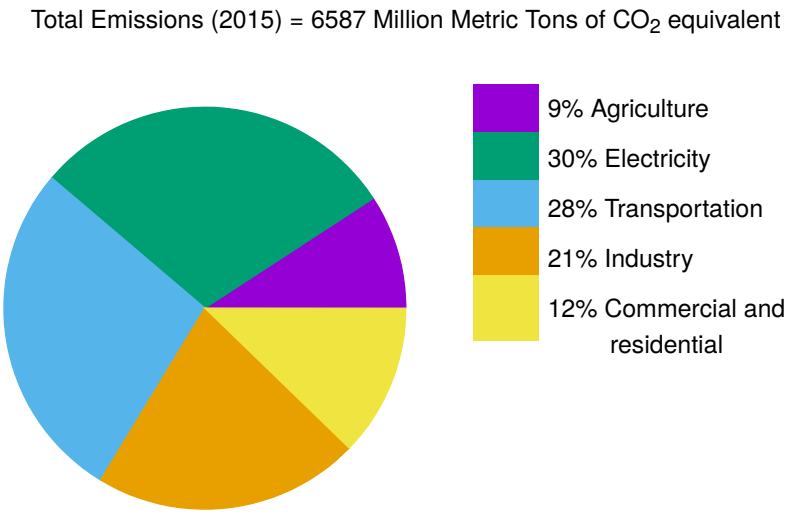


Figure 5.1.1: Breakdown by sector of the total emissions in 2015. The total sum amounts to 6587 Million metric ton of CO_2 equivalent. The data are taken from [224].

with a fully-charged battery, and 2. downtime, i.e., how long does it take to go back to full charge. The translation in technical terms of the former requirement is a battery with an specific energy density* of, at the very least, 120 W h kg^{-1} and a number of reliable charging/discharging cycles exceeding 1000, all of the above at a reasonable, i.e., market-competitive, price. Table 5.1.1 shows a comparison of the specific energy for different storage materials.

Lithium-ion batteries research is currently one of the most supported for essentially two major reasons: 1. weight, i.e., lithium is the lightest electrochemically-useful element that can be relatively safely be handled, and 2. highest oxidation potential [64]. An example of a rechargeable Li-based battery is sketched in Figure 5.1.2. Nevertheless,

*Or energy per unit mass, not to be confused with energy density, i.e., energy per unit volume. Specific energy density is often the quantity of choice when referring to storage technology for vehicles due to the importance of controlling the total weight of the system.

Storage material	Specific energy density [W h kg^{-1}]	Reference
Lead-acid battery	25-80	[225]
Lithium-ion battery	125-250	[226]
Carbohydrates	4800	[227]
Kerosene	12 000	[228, 229]
Diesel	12 000	[229]
Uranium	22 393 817 400	[230]
Deuterium-Helium-3	107 000 000 000	[231]

Table 5.1.1: Specific energy density for different storage materials.

current solutions are not entirely viable and gargantuan research efforts, in both academia and industry, aim to improve specific energy density, reliability, lifetime, safety, and, ultimately, lower costs. The approaches taken could essentially be summarised in the development of new 1. high-capacity, electrode materials, and 2. safer and highly-lithium-conductive electrolytes. During my time at the Robert Bosch Research and Technology Center, Cambridge, MA, I mainly focused on the latter.

The electrolyte has the dual task of acting as an insulator to electrically separate the anode from the cathode, while at the same time allowing the movement of lithium from one to the other. A Lithium-anion* salt is dissolved in the electrolyte to provide a quickly accessible source of lithium to the electrodes. Solid polymer electrolytes are preferred over liquid ones thanks to their key advantages in terms of safety, such as absence of leakage of the electrolyte, non-combustible reaction products at the interface with the electrodes, and no internal shorting [52–58]. Ionic conductivity is the major drawback for polymer-based electrolytes. Electrically powered vehicles would require batteries with an electrolyte possessing an ion conductivity of at least 10^{-5} S cm^{-1} in a temperature range of -20 °C to 60 °C, and conductivity in polymers is normally far lower than this [64]†.

*The presence of the anion is necessary to ensure charge-neutrality in the battery.

†Ceramic and glass materials are also investigated thanks to their ionic conductivity often exceeding 10^{-3} S cm^{-1} to 10^{-1} S cm^{-1} (for instance [60–62]) for a wide range of temperatures. However, they lack the mechanical properties to withstand the severe changes in volume that the electrodes undergo during lithiation and delithiation [63]. For example, one of the most commonly used material for the negative electrode, graphite, expands up to 10 % [232–234], while Si and Sn can have a volume expansion up to 400 % [235–237].

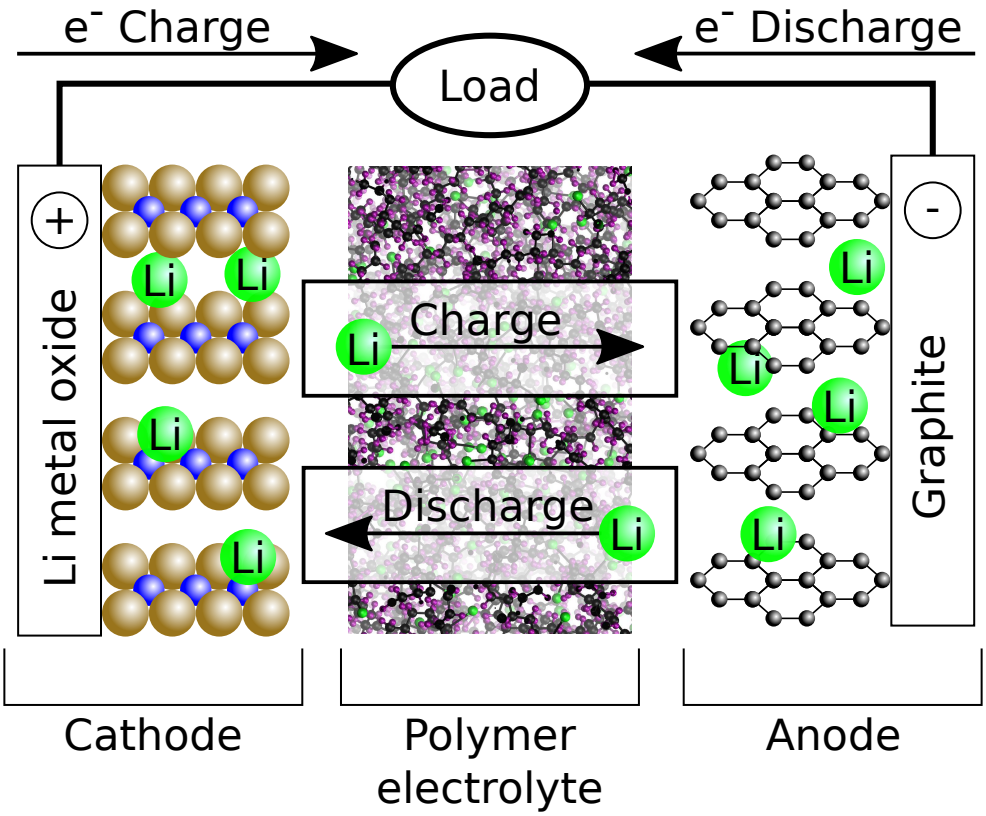
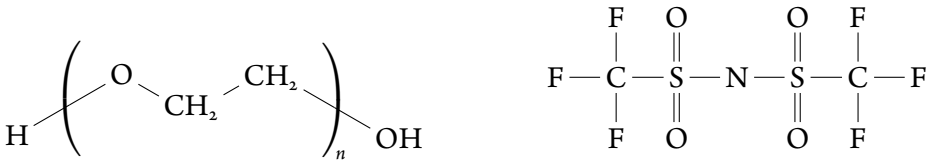


Figure 5.1.2: Typical set-up of a rechargeable Li-ion battery. This type of battery is "rechargeable", meaning it can be used multiple times, or cycles, as an energy storage component. During the discharging phase, electrons flow from the anode to the cathode, driven by the difference in electrochemical potential. At the same time, the electrical charge needs to be neutralised with a similar flow of positive charge in order to sustain the process. This task is accomplished by the lithium cations diffusing through the medium that separate the two electrodes. This medium is known as electrolyte, and its properties are fundamental in the determination of the efficiency as well as safety of the entire electrochemical cell. When an appropriate voltage is applied, the electrons and cations move back to the anode in what is, effectively, a charging phase.

5.1.1 LiTFSI and PEO

In the first study of lithium-alkali metal salt dissolved in PEO (molecular structure in Figure 5.1.3a) in 1973, the reported lithium conductivity at ambient temperature was 10^{-8} S cm^{-1}, well below the acceptance threshold [238]. However, the proof of ionic



(a) PEO **(b)** TFSI

Figure 5.1.3: Molecular structure for the TFSI molecule and for the PEO polymer, where n is the number of monomers composing a chain.

conduction combined with chemical inertness sparked interest in PEO-based systems. One of the currently most promising Li-salt-polymer combination is the lithium-TFSI-PEO*, which shows an ionic conductivity on the order of 10^{-4} S cm^{-1} to 10^{-3} S cm^{-1} at 80 °C [243]. Figure 5.1.3b shows the molecular structure of TFSI.

Molecular dynamics simulations have been extensively used to develop a molecular-level understanding of this promising electrolyte, however, the vast majority of the literature focuses on the dilute limit. For instance, efforts focused on explaining the comparatively high cationic conductivity, the nature of the lithium coordination cage, and the mechanisms by which Li moves through the polymer [244–250]. Whilst these investigations are precious to unveil fundamental knowledge, for instance the fact that lithium is coordinated by the oxygen atoms present on the PEO backbone, technologically-relevant systems require high concentrations of the lithium salt. Highly-concentrated systems are less studied, and efforts mainly focused on clarifying the relative merit of different mechanisms of lithium diffusion [250, 251]. Motivated by recent experimental speculation [252], a molecular dynamics approach has been used to investigate the role of ionic-liquid (IL) molecules on lithium mobility in Li-TFSI-PEO-IL systems. A higher diffusion coefficient for lithium in such systems was found and its origin can be attributed to the plasticizing effect induced by the IL molecules [253]. Nonetheless, essentially all the lithium atoms in the system were found to be coordinated by the oxygen on the PEO backbone, further highlighting the importance of a fundamental understanding of the Li-TFSI-PEO system at technologically relevant salt concentration. A specific understanding on the relations between coordination,

*Li-TFSI salt has received much attention mainly thanks to its high solubility in PEO, good thermal and hydrolytic stability compared to the popular Li-PF_6 salt [239–242].

cooperative ion motion and clustering for high salt concentrations in Li-TFSI-PEO is lacking, and this motivates the investigation presented in this chapter.

5.2 The model

Typically, the molecular weight, M_w, of the PEO chains used in polymer electrolytes is in the 4000 Da to 5000 Da range, i.e., as short as possible without the risk of the polymer diffusing into the electrodes. The systems simulated in this chapter are composed of 40 PEO chains, each 100 monomers long, $n = 100$ in Figure 5.1.3a, and hydrogen is used as termination, hence the M_w is 4402 Da. The number of LiTFSI molecule is either 120, corresponding to a salt concentration of 1 M, or four times higher (480 and corresponding to a 4 M solution), for a total number of simulated atoms of 30 000 and 35 760, respectively. To prepare the initial structures, first all the lithium atoms are placed in a cubic cell with a large volume* to avoid a subsequent stagnation when the polymer chains are grown in it. Second, the TFSI anions are added, followed by the chains, which are grown in the remaining free volume of the cubic cell.

The initial structure builder as well the force-field used to describe the molecular interactions are taken from the MedeA package developed by Materials Design. The second-generation PCFF+ is the force-field of choice for this work†, and the point charges of Li and TFSI are reduced so that the total cation/anion charge is 0.75 e [254]. A summary of the charges assigned to the atoms constituting the TFSI anion is presented in Table 5.2.1 for all the scenarios investigated. Whilst accessible to licensed users, the PCFF+ parameters are part of a proprietary force-field and therefore not reported here, however, the functional form of the potential energy is freely available and summarised in Appendix B.

*Following the same logic as in subsection 3.2.2, the volume is chosen so that the total mass density once all the atoms are inserted is around 40 % of the equilibrium density at room temperature and pressure.

†PCFF+ is a proprietary force-field, however, unlike the condensed-phase optimized molecular potentials for atomistic simulation studies (COMPASS) force-field (introduced in subsection 2.2.1), the parameters are not hidden in an encrypted database. Therefore, scientists can access, inspect, compare, and modify them. Furthermore, the adoption of PCFF+ does not limit the choice of the molecular dynamics (MD) engine, in other words, the open-source and widely adopted large-scale atomic/molecular massively parallel simulator (LAMMPS) can be used.

Atom type	Charges [|e|]		
	Normal	Polar	Spread
N	-0.482	-2.25	-0.05
S	+1.308	0.00	-0.05
O	-0.624	0.00	-0.05
C	+0.748	+0.75	-0.05
F	-0.314	0.00	-0.05
Total	-0.750	-0.750	-0.750

Table 5.2.1: Point charges of the atoms constituting the TFSI anion. Three different scenarios are investigated and their partial charges summarised: 1. normal dynamics, 2. and 3. we modify the charges to simulate a more/less polar configurations, respectively. The charge for the cation is chosen accordingly to ensure charge neutrality in the system.

Once generated, the structures are brought close to equilibrium by a series of energy minimisation, compression/decompression, and annealing stages similar in nature to those in subsection 2.2.4 and in [133]. Table 5.2.2 summarises the equilibration procedure. LAMMPS is used as the MD package. All MD simulations have periodic boundary conditions, and a timestep of 1.0 fs is chosen to integrate the equations of motion. Pressure and temperature are imposed on the system with the Nosé-Hoover formulation for barostat and thermostat as implemented in LAMMPS, and are kept fixed throughout this study at 0.1 MPa and 353 K, respectively.

With the aim to quickly verify the transferability of the PCFF+ parameters and, hence, the validity of the model, mass density and lithium conductivity are computed as a function of salt concentration at 353 K and compared to experiment. After the equilibration procedure, the structures are run for 0.5 ns and the density recorded every 100 fs to ensure sufficiently uncorrelated values. The mass density and its uncertainty are the average and standard deviation of the 5000 recorded values. The mass density for the 1 M system is 1.129(3) g/cm^3 and 1.335(3) g/cm^3 for the 4 M structure. The experimental mass density for pure PEO, at 298 °C and $M_w \sim 5000$, was reported to be 1.12 g/cm^3 [159], and 2.023 g/cm^3 for LiTFSI [255]. Therefore, we expect the density to increase for larger salt concentrations, as is observed in our simulations. 1.2 gcm^{-3} and

Stage	Stage duration [ns]	Total time [ns]	Temperature [K]	Pressure [MPa]
Energy minimisation	-	-	-	-
NPT (compression)	0.10	0.10	353	$0 \rightarrow 100$
Energy minimisation	-	-	-	-
NPT (compression)	0.50	0.60	353	$0 \rightarrow 400$
NPT	0.40	1.00	353	400
NPT (decompression)	0.60	1.60	353	$400 \rightarrow 0.1$
NPT (heating)	0.40	2.00	$353 \rightarrow 453$	0.1
NPT (cooling)	0.40	2.40	$453 \rightarrow 353$	0.1
NPT (compression)	0.30	2.70	353	$0.1 \rightarrow 400$
NPT (decompression)	0.30	3.00	353	$400 \rightarrow 0.1$
NVT	0.80	3.80	353	-
NPT	1.20	5.00	353	0.1

Table 5.2.2: Stages used to equilibrate the Li-TFSI-PEO initial structures.

1.3 gcm^{-3} are the mass density values for 1.0 M and 4.1 M, respectively, computed from the experimental molal density [243], using Equation 5.3. ρ_x, m_x, V_x are the density, mass,

$$
\begin{aligned}
\text{Solute (TFSI) index} &= 1, \\
\text{Solvent (PEO) index} &= 2, \\
\text{Molal concentration} &= A = \left[\frac{mol\,(\text{solute})}{Kg\,(\text{solvent})}\right], \\
\text{PEO+TFSI density} &= \rho_{1+2} = \frac{m_1 + m_2}{V_1 + V_2}, && (5.1) \\
&= \frac{m_2\left(1 + \dfrac{m_1}{m_2}\right)}{V_2\left(1 + \dfrac{V_1}{V_2}\right)}, && (5.2) \\
&= \rho_2 \frac{1 + A * (M_{W,1}/10^3)}{1 + A * (M_{W,1}/10^3) * \dfrac{\rho_1}{\rho_2}}. && (5.3)
\end{aligned}
$$

and volume of component x, respectively, and $(M_{W,1}/10^3)$ is the molecular weight of TFSI, rescaled to Kg/mol. To further test the force-field, the attention was shifted to the cation conductivity. The values for the lithium conductivity are computed from a 140 ns NPT simulation using the Wheeler-Newman approach for concentrated solutions [256] To summarise, the Wheeler-Newman is a method to simulate multicomponent diffusion in concentrated solutions with the use of MD simulations. The full diffusion-coefficient matrix for all species is computed with a Green-Kubo approach to Stefan-Maxwell diffusivities. Their final result links the mass-transport coefficients L°_{ab}, Equation 5.4,to the generalised species flux $J_{a,b}$, Equation 5.5.

$$L^{\circ}_{ab} = \frac{V}{3k_B T}\int_0^{\infty} \langle \vec{J}_a(t) \cdot \vec{J}_b(0)\rangle dt, \tag{5.4}$$

$$\begin{aligned} \vec{J}_i &= \frac{\partial}{\partial t}\vec{R}_i \\ &= \frac{\partial}{\partial t}\left[\frac{1}{N_i}\sum_{j\in i}\vec{r}_j - \frac{1}{N_0}\sum_{j\in 0}\vec{r}_j\right]. \end{aligned} \tag{5.5}$$

a and b refer to two different species, i can be either a or b, and 0 corresponds to the reference species. For $a = b$ we obtain the self-diffusion coefficient. The conductivity κ is then computed as

$$\kappa = \sum_{a\neq 0}\sum_{b\neq 0} L^{\circ}_{ab}\theta_a\theta_b. \tag{5.6}$$

Where θ_a and θ_b are the charge densities of species a and b, respectively. Substitution of the electrical current definition

$$\vec{i}_c = \sum q_i \vec{v}_i, \tag{5.7}$$

where q_i is the electrical charge of molecule or ion i, and of Equation 5.4 into Equation 5.6, the well-know Green-Kubo expression for electrical conductivity is obtained [257, 258]

$$\kappa = \frac{1}{3Vk_B T}\int_0^{\infty} \langle \vec{i}_c(t) \cdot \vec{i}_c(0)\rangle dt. \tag{5.8}$$

The angular brackets indicate ensemble, or simulation, average. The equivalence of the

two is ensured by the ergodic hypothesis [259]. For an observable $\mathcal{O} = \mathcal{O}\left(\vec{v}^N(t), \vec{r}^N(t)\right)$ the ergodic hypothesis says

$$\langle \mathcal{O} \rangle = \bar{\mathcal{O}}, \tag{5.9}$$

$$\langle \mathcal{O} \rangle = \lim_{s\to\infty} \frac{1}{s} \sum_{j=1}^{s} \mathcal{O}\left(\vec{v}^N, \vec{r}^N\right),$$

$$\bar{\mathcal{O}} = \lim_{s\to\infty} \frac{1}{s} \int_0^s \mathcal{O}\left(\vec{v}^N(t), \vec{r}^N(t)\right) dt.$$

Where the angular brackets indicates the ensemble average, while the bar the time average. Complete details on the procedure used to compute the conductivity can be found in [256]. Figure 5.2.1 presents the comparison between the experimental lithium conductivity values from [243] and the computed ones as a function of LiTFSI salt concentration. The results show good qualitative agreement with experiments, and the

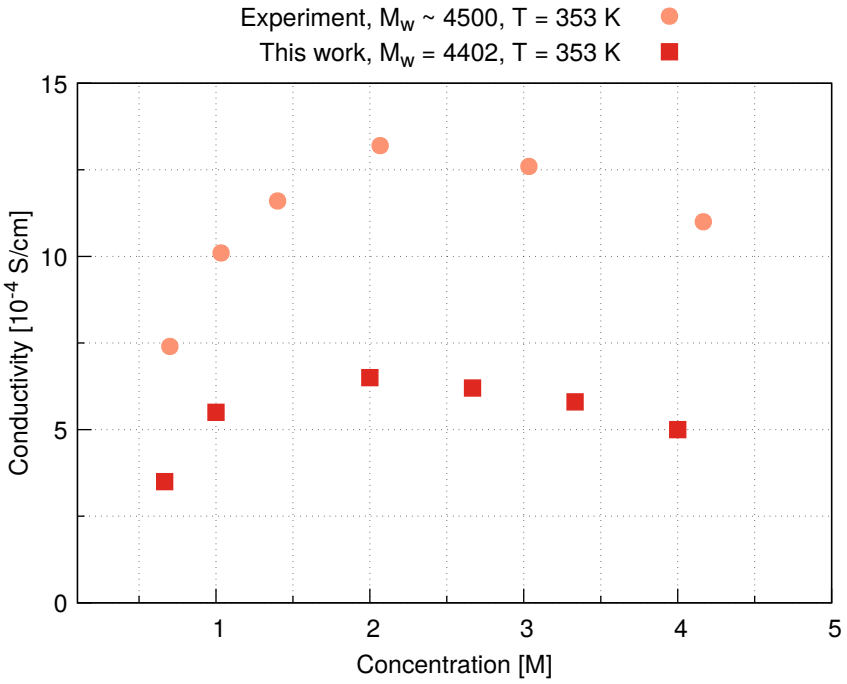


Figure 5.2.1: Li ionic conductivity as a function of Li-salt concentration. The experimental data are taken from [243].

quantitative values are within a factor of two of experimental ones. In particular, the peak in the lithium conductivity at a salt concentration of roughly 2 M is reproduced. The obtained results for mass density and cationic conductivity give us confidence in the transferability of the PCFF+ force-field to the system of interest, allowing us to proceed with the investigation.

At this stage, the structures are ready to undergo the MD simulation needed for the lithium coordination and mobility analysis: 20 ns at constant pressure, 0.1 MPa, constant temperature, 353 K, and constant number of particles. Every 100 ps, a snapshot of the structures, in other words the complete set of coordinates for all the atoms, is saved for post-processing analysis.

5.3 Results & Discussion

5.3.1 Concentration and coordination

A distance threshold defining when a given cation is coordinated by a given oxygen is required. Such a threshold should minimise the noise due to the fluctuations in the determination of the lithium coordination cage. With this in mind, a "lithium hopping matrix", an example of which is presented in Figure 5.3.1, is constructed as follows.

1. A radius, R_c, in the range between 3.00 Å to 6.00 Å at steps of 0.20 Å, is chosen. Then, a sphere of radius R_c and centred on a lithium atom is constructed, and the oxygen atoms, from the PEO backbone, inside the sphere are counted. The counting operation is repeated for all the lithium atoms in the system and at all recorded snapshots.

2. Two-value tuples are formed by saving the number of coordinating oxygen atoms at snapshot n and snapshot $n + 1$. The total number of tuples is $m \cdot 200$[*], where m is the total number of lithium in the system, which can be either 120 or 480 depending on the salt concentration.

[*]The 200 is the total number of snapshots recorded, i.e., 20 ns divided by 0.1 ns.

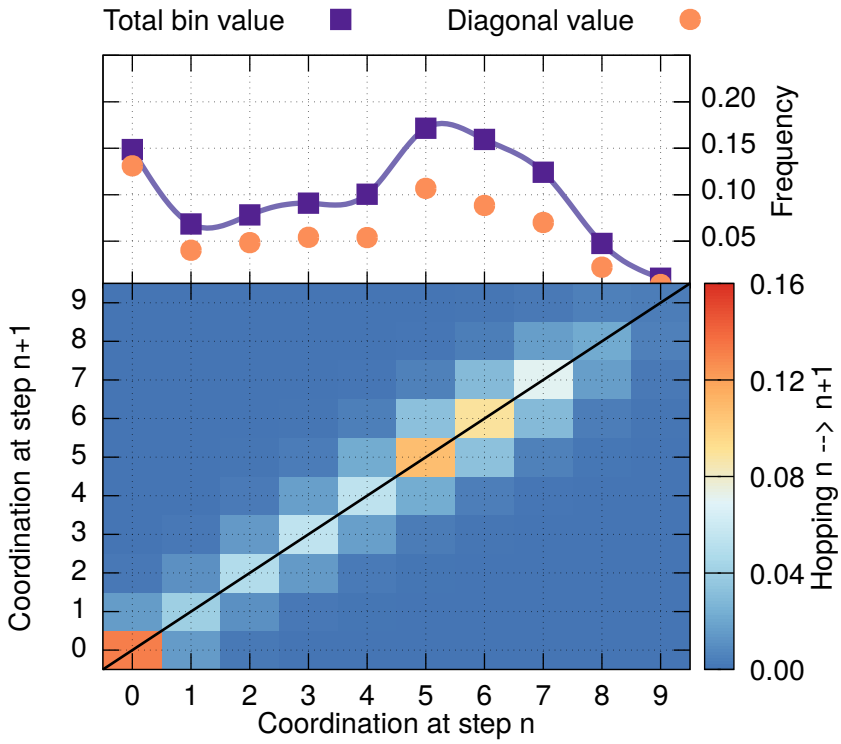


Figure 5.3.1: Example of the lithium hopping matrix for 4 M salt concentration and $R_c = 4.00$ Å.

3. A matrix is constructed with the tuples by using the number of oxygen atoms coordinating at snapshot n and $n + 1$ as column and row indices, respectively. The matrix is normalised to one.

The diagonal values of such matrix indicate the fraction of lithium atoms that did not change the number of coordinating oxygen atoms from the PEO backbone between two consecutive snapshots of the structure. On the other hand, off-diagonal values represents a change in the coordination cage.

The plot on top of the hopping matrix in Figure 5.3.1 shows the diagonal contribution to every column. The ratio between the diagonal value and the total column value is related to how stable the computed coordination cages are. Figure 5.3.2 shows the percentage contribution of the diagonal value to the total coordination bin, i.e., to a given

column, as a function of different R_c. The diagonal contribution shows a peak at $R_c =$

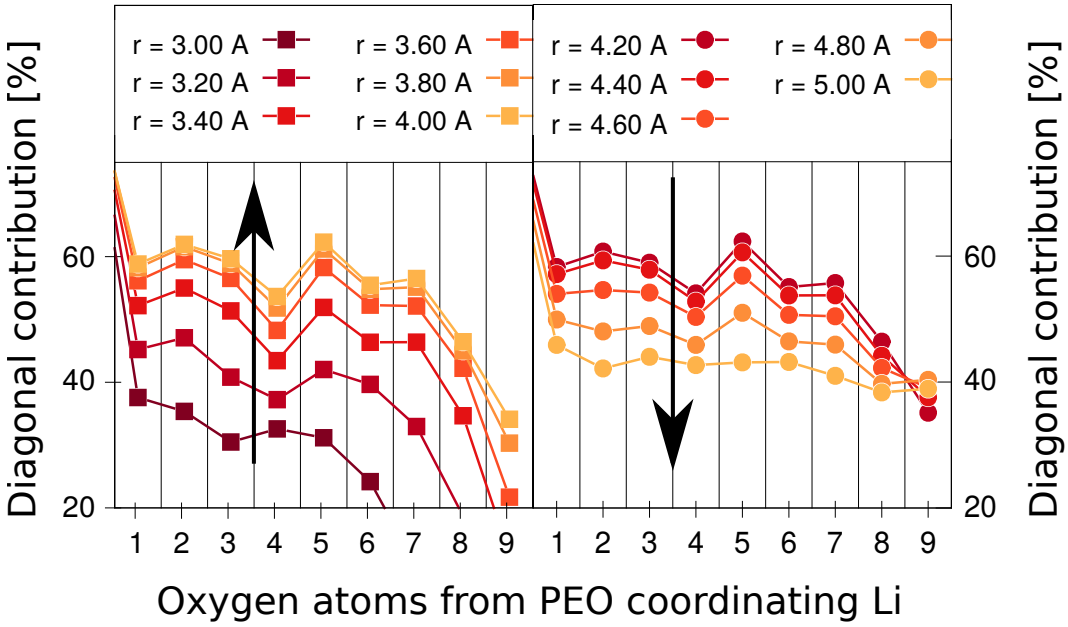


Figure 5.3.2: Percentage contribution to the total coordination of the stable cages, i.e., of the cages that do not change in size between two consecutive snapshots of the structure.

4.00 Å, this finding is interpreted as follows.

- $R_c < 4.00$ Å. The lower fraction of stable coordinating cages is due to the only partial inclusion of the oxygen atoms composing a cage. R_c is small, therefore thermal fluctuation of the cage and of the lithium position result in transitions that correspond to the lithium moving within the same cage*.
- $R_c > 4.00$ Å. At large R_c and after the peak, the diagonal contribution decreases since oxygen atoms beyond the coordinating cage start to be included. This oxygen atoms do not coordinate the lithium and, therefore, should be excluded.
- $R_c = 4.00$ Å. At this cutoff radius the fraction of stable coordinating cages has its maximum, indicating that the uncertainty in determining the number of oxygen

*A quick check on the indices of the oxygen atoms coordinating ensured that the fluctuations in the coordinating number are not due to an actual change in cage.

actually coordinating a given lithium is minimised. In other words, $R_c = 4.00$ Å ensures the noise due to temperature fluctuation in the determination of the coordination cage is minimised.

Therefore, oxygen atoms* are considered as "coordinating" a given lithium if found within a sphere of radius 4.00 Å centred on that given cation.

Figure 5.3.3 shows the relative contribution of the oxygen atoms from PEO and TFSI to the total coordination at 4 M, Figure 5.3.3(a)-(c), and 1 M, Figure 5.3.3(d)-(f). In other

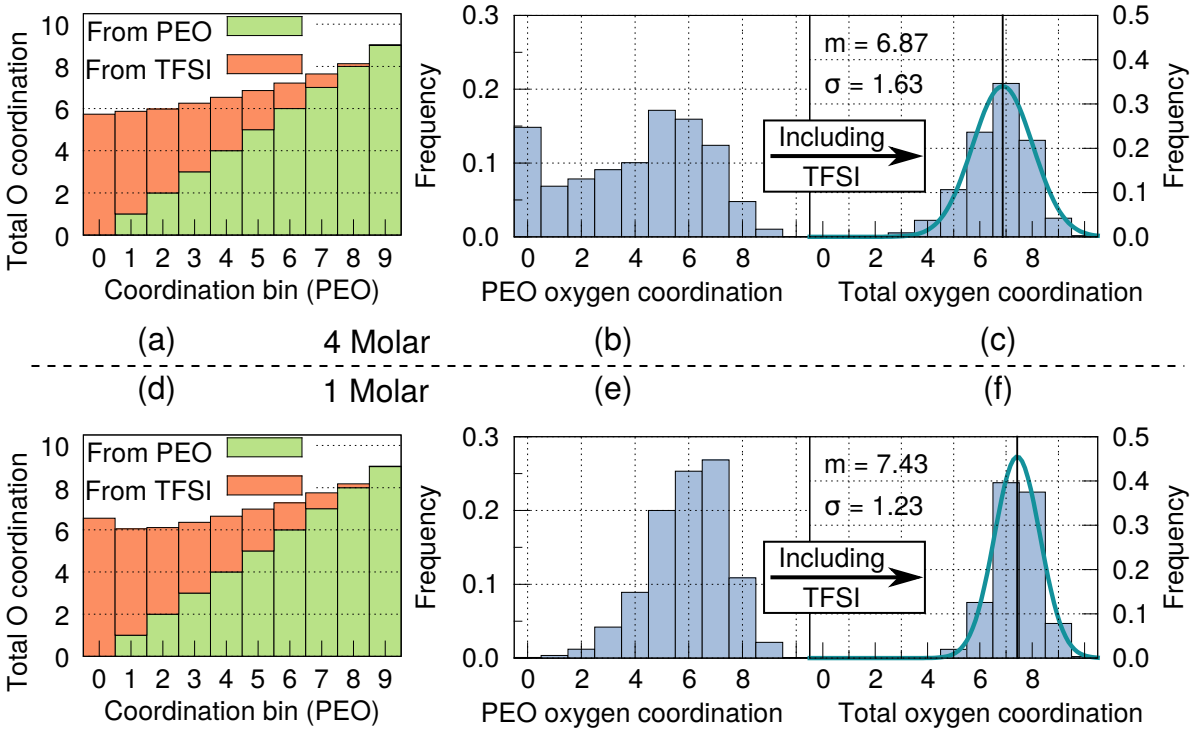


Figure 5.3.3: From left to right: (a,d) Relative contribution to the cation total coordination of Li by oxygens from the TFSI anion and the PEO backbone, (b,e) coordination distribution when only the oxygens from the polymer are taken into account and (c,f) total coordination distribution where both anion and polymer oxygens are counted. From top to bottom: 4.00 M and 1.00 M salt concentration.

words, Figure 5.3.3 provides the relative statistics of Li coordination by PEO and by TFSI

*Either from the PEO backbone or the TFSI anion depending on the study.

in the Li-TFSI-PEO system. Looking at Figure 5.3.3(b), there is a large fraction of Li ions with a small coordination number (less than four) if only the oxygen atoms from PEO are taken into account. It is clear that the anion plays a substantial role in the coordination of Li, especially for the fraction of cations which are under-coordinated by the PEO oxygen, and coordination cages as (a) and (c) in Figure 5.3.4 appear in the system. In particular,

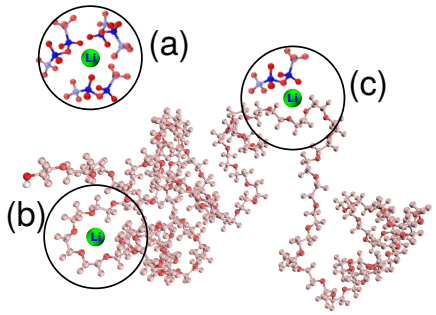


Figure 5.3.4: Schematic representation of different coordination environments of Li ion. (a) refers to a anion-only coordination, (b) shows a PEO-only one-chain coordination and (c) sketches a PEO-TFSI mixed coordination environment.

for the 4 M case, approximately 15 % of the cations have no coordination by PEO. Figure 5.3.3(a) presents the oxygen contribution from the anion to the Li coordination for different PEO coordination environments. Combining the anion contribution (Figure 5.3.3(a)) with the PEO contribution of coordination (Figure 5.3.3(b)), the total distribution of oxygen surrounding the cations in the system is obtained, as shown in Figure 5.3.3(c). Also, the majority of Li ions are coordinated by a single PEO chain, as shown in Figure 5.3.5, confirming previous results from the literature [247, 249]. For the 1 M case ∼80 % of Li is coordinated by one chain and almost all the rest by two chains. For the 4 M case ∼75 % of Li is coordinated by one chain and ∼10 % by two chains, and ∼15 % of Li is not coordinated by the polymer at all.

On the one hand, the overall oxygen coordination distribution is barely modified going from the 1 M to the 4 M salt concentration (Figure 5.3.3(f),(c), respectively), and the total 6-7 oxygen coordination reported in the literature is reproduced [244, 246, 260]. On the other hand by looking more closely at the origin of the coordinating oxygen, the oxygen atom from TFSI account for 39 % and 19 % of the total count for respectively the

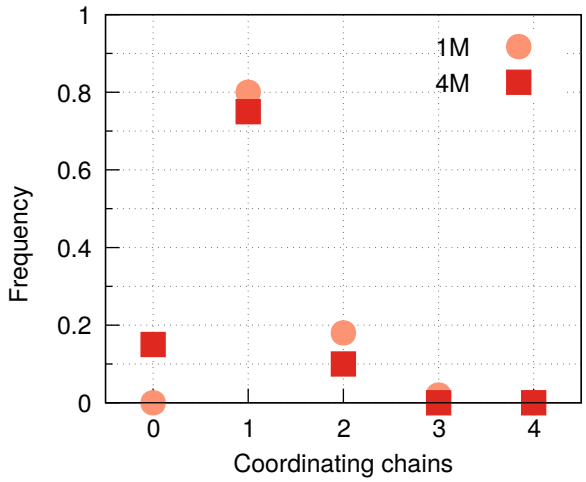


Figure 5.3.5: Frequency of the number of unique PEO chains coordinating the lithium atoms. the values are averaged over all the lithium and snapshots.

4 M and 1 M salt concentrations. The unexpected finding is that an ensemble of Li ions exists that is not coordinated by any oxygen from the polymer backbone, Figure 5.3.3(b), instead associating only with TFSI anions, especially at high salt concentrations. The landscape in which the cations move is completely altered by the presence of the anion and this has a significant effect on its mobility as it is observed in the next section.

5.3.2 Concentration and Mobility

The landscape in which the cations reside is strongly modified at high salt concentrations, so now the mobility of the lithium atoms in different coordination families is investigated. To this end, the average distance travelled by all the cations in a given coordination bin over a time period of 100 ps is studied. As an estimate, a time window of 100 ps allows an investigation of the mobility of the lithium atoms, despite not being sufficient for the system to reach the diffusive regime[*].

Figure 5.3.6 summarizes the findings for the two salt concentrations under

[*]This time window of 100 ps is meant to have no connections with the long-scale diffusion, but rather it is used to show and study the different mobility experienced by lithium atoms in different coordination environments.

investigation. At the lower salt concentration, a higher cation mobility than for the more

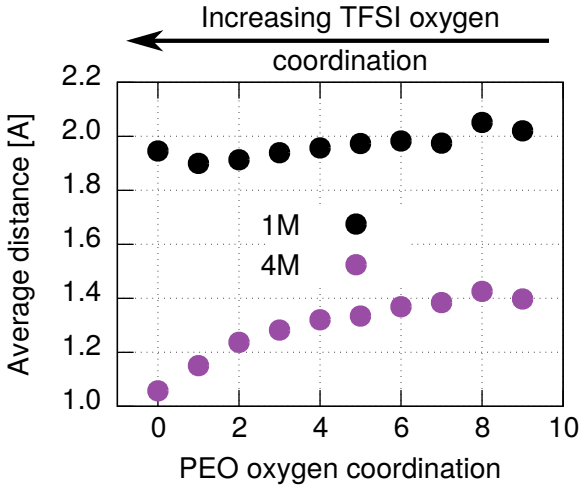


Figure 5.3.6: Average distance travelled by the cations in a specific oxygen (from the polymer) coordination bin over 100 ps for both the 1 M and 4 M salt concentration.

concentrated case is obtained, as previously observed experimentally [261, 262]. Moreover, different coordination environments do not lead to significant differences in the mobility for the 1 M case. On the other hand, the 4 M case produces a different behaviour: the more the Li cation is coordinated by the anion, the lower its mobility is, by up to 40 % at full TFSI-coordination. The nucleation of clusters in the system is found to be the origin of these observations, and it is studied in the following section.

5.3.3 Clustering

An important observation from Figure 5.3.3(a),(d) and Figure 5.3.6 is that the anion-cation coordination has a noticeable effect on the cation mobility. Here, the spatial correlation between the two components is analysed by looking at the clusters they form during the simulation. A cluster is identified by iteratively grouping Li cations with TFSI anions based on a threshold distance of 3.25 Å between any TFSI atom with a negative

point charge and Li*. Starting from a lithium in the system, all negative anion species within the cutoff are recorded. If any are found, lithium atoms, other than the initial one, are searched within the same cutoff, but now centred on all negative species of the anions found at the previous step. The operation is repeated until no new species are found and the cluster composition is identified by counting the cations and anions. $(C_iA_j)^{i-j}$ denotes the cluster with the number of Li atoms i, TFSI molecules j, therefore having charge $i - j$. The operation is then repeated from a different starting lithium. Figure 5.3.7(a),(b) present the distribution of cluster compositions at 4 M salt concentration on the left, (a), and the biggest cluster during the entire simulation on the right, (b). Figure 5.3.7(c),(d) show the same information for the 1 M case. The black diagonal line in both Figure 5.3.7(a) and (c) corresponds to clusters with symmetric compositions $i = j$, i.e., equal count of anions and cations. At both salt concentrations the most common clusters are small, containing only a few atoms/molecules. The most frequent species are always the $(C_1A_0)^{1+}$ and $(C_0A_1)^{1-}$ where Li and TFSI are isolated from each other, as shown in Table 5.3.1, and $(C_1A_1)^0$ corresponding to a dimer. As expected from electrostatic considerations, extreme cases where there is a high composition asymmetry (high total charge) are not present. This observation also explains the lower amount of small clusters with even size ($i + j = 2n$) compared to the nearest odd sizes ($i + j = 2n \pm 1$) in Table 5.3.1. Ignoring the contribution from neutral clusters, the major contribution to even clusters is from $i - j = \pm 2$, which carries a double positive/negative charge. One notable observation is the tendency for big clusters to have an anion predominance in their composition. This can be noticed from the asymmetry of the distribution of frequencies with respect to the black diagonal line in Figure 5.3.7(a) and (c) as well as from Table 5.3.1. Since the total number of Li and TFSI are equal in the simulation,

*The threshold distance is different to the one used earlier in the chapter, where only oxygen atoms from the PEO backbone were taken into account. 3.25 Å was determined in the following manner. The partition of clusters is computed for thresholds ranging from 3.00 Å to 5.00 Å at steps of 0.25 Å. A non-monotonous partition of the clusters is observed: the fraction of three-body clusters, i.e., clusters of size three, initially increases, it peaks and then starts decreasing in favour of bigger clusters. A too small threshold value would result in an artificially-higher number of isolated Li atoms and TFSI molecules, while a too large threshold value increases the fraction of bigger clusters. Hence, the value of the threshold distance corresponding to the peak was chosen. Note that a similar non-monotonous behaviour is observed when focusing on higher order clusters (but clearly at larger thresholds); however, focusing on the smallest, non-trivial clusters was deemed to be the most sensible option.

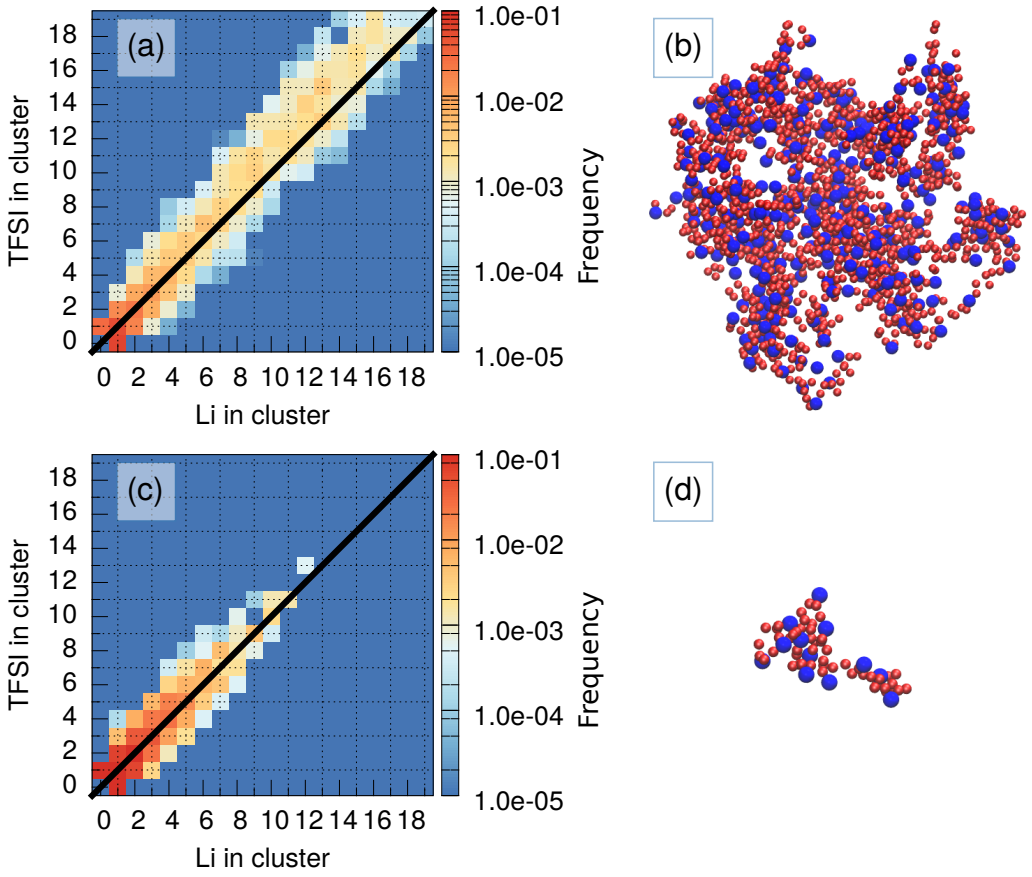


Figure 5.3.7: Cluster analysis. (a),(b) refer to the 4 M case while (c),(d) to the 1 M one. The plots on the left, (a) and (c), summarise the cluster compositions during the simulation. The structures on the right, (b) and (d), show the biggest cluster formations found during the 20 ns dynamics.

looking at the difference between $(C_1A_0)^{1+}$ and $(C_0A_1)^{1-}$, the isolated species, the overall asymmetry in the cluster compositions can be determined. In the 4 M case there are almost three times as many isolated Li ions than isolated TFSI molecules (6.5% versus 2.3%). This implies that over the entire population of non-trivial clusters ($i + j > 1$) there is an overall asymmetry, with the majority of clusters containing an excess of TFSI and thus negatively charged. At lower concentration, a higher percentage of isolated $(C_1A_0)^{1+}$ cation and $(C_0A_1)^{1-}$ anion species is observed, and clusters are overall smaller. This is consistent with 1 M Li-TFSI concentration being lower than the solubility limit at these

Cation + **A**nion: Positive combinations (reverse indices and charge for negative)	1 M			4 M		
	Positive		Negative	Positive		Negative
1: $(C_1A_0)^{+}$ — Free species	13 %	>	12 %	6.5 %	>	2.9 %
3: $(C_2A_1)^{1+}$, $(C_3A_0)^{3+}$	6.4 %	<	6.8 %	1.7 %	>	1.5 %
4: $(C_3A_1)^{2+}$, $(C_4A_0)^{4+}$	0.2 %	<	0.5 %	0.1 %	=	0.1 %
5: $(C_3A_2)^{1+}$, $(C_4A_1)^{3+}$, $(C_5A_0)^{5+}$	2.4 %	<	4.1 %	0.7 %	<	0.8 %
6: $(C_4A_2)^{2+}$, $(C_5A_1)^{4+}$, $(C_6A_0)^{6+}$	0.1 %	<	0.7 %	0.1 %	<	0.2 %
7: $(C_4A_3)^{1+}$, $(C_5A_2)^{3+}$, $(C_6A_1)^{5+}$, $(C_7A_0)^{7+}$	0.9 %	<	2.1 %	0.4 %	<	0.5 %
8: $(C_5A_3)^{2+}$, $(C_6A_2)^{4+}$, $(C_7A_1)^{6+}$, $(C_8A_0)^{8+}$	0.2 %	<	0.5 %	0.1 %	<	0.2 %

Table 5.3.1: (cation + anion) / (total number of cation and anion) percentage for all asymmetric clusters with size: (cation + anion) ≤ 8. The first column reports a given cluster size followed by all the positive cluster combinations possible at that size. The negative clusters with the same total size have switched cation/anion indices and opposite cluster charge. For every cluster size and concentration we report the summation over all the positive (cation > anion) and negative (anion > cation) clusters, separately.

conditions and model parameters. At the same time cluster composition is more symmetric than at 4 M salt concentration, but negatively charged clusters still account for the majority, however with a small margin.

While the existence of clusters is expected based on similar observations on different salts [249, 263–265], the asymmetry in the clusters is unexpected. It has been previously shown that clusters are undesired since they lower the ability of the system to transport ionic charge [265]. The merit of different Li-salts concentration on transport properties such as, for instance, transference number is dubious since different effects for increasing salt concentrations have been observed experimentally [266–271]. The asymmetry in the cluster composition may have a significant effect on the overall transport properties of the system. On the one hand, small negatively charged clusters such as $(C_1A_2)^{1-}$ or $(C_2A_3)^{1-}$ would transport Li in the direction opposite to where positive Li ions move during battery operation, thereby reducing the Li transference number. On the other hand, the higher number of free Li and its higher mobility than that of clusters could counterbalance this effect. Further in-depth investigations of the effect of correlation and

asymmetry on macroscopic transport properties, in the context of concentrated solution theory, would help in assessing their interplay and relative importance.

5.3.4 Modifications

Here the efforts to gain microscopic understanding of the role of cations and anions and their correlation in transport properties are presented. The 4 M salt concentration is the focus of this study. The approach is to perform computational experiments by introducing controlled modifications and constrains in the electrolyte system. Similar modifications are normally hard to reproduce experimentally, and, therefore, the conclusions drawn from the following results should be interpreted as an effort to gain mechanistic understanding.

The first investigation consists of fixing in space a given number of atoms in the simulation and observing the implications on the mobility of the cations; the total number of fixed atoms is 480. Figure 5.3.8(a) shows the result of freezing all the nitrogen belonging to TFSI, which immobilizes the anions. This allows us to study the impact of anion mobility on the cation mobility. Fixing the nitrogen positions has the obvious effect of decreasing the mobility of the cations that are predominantly coordinated by TFSI. Furthermore, freezing the nitrogen atoms has an effect on the mobility of Li cations that are mainly surrounded by oxygen atoms coming from the polymer backbone as well. This is explained by observing that, even if not directly limited in their movements, PEO chains experience numerous constraints when all the anion present in the system are frozen, hence the polymer segmentation is hindered.

In Figure 5.3.8(b), every PEO chain is frozen directly in 12 points, i.e., roughly every eight monomers. The major change in mobility is found in cations that are mainly PEO-coordinated. The effect on cations that are mainly coordinated by the anion is weaker than the effect on cations coordinated by the polymer when the nitrogen atoms of TFSI are immobilised. This suggests that the mobility of Li-TFSI clusters is not severely altered by reducing the freedom of movement of the chains. Given that Li mobility noticeably changes when the movement of PEO chains is restricted, the polymer chain motion plays a central role in cation diffusion, and any restrictions would result in lower

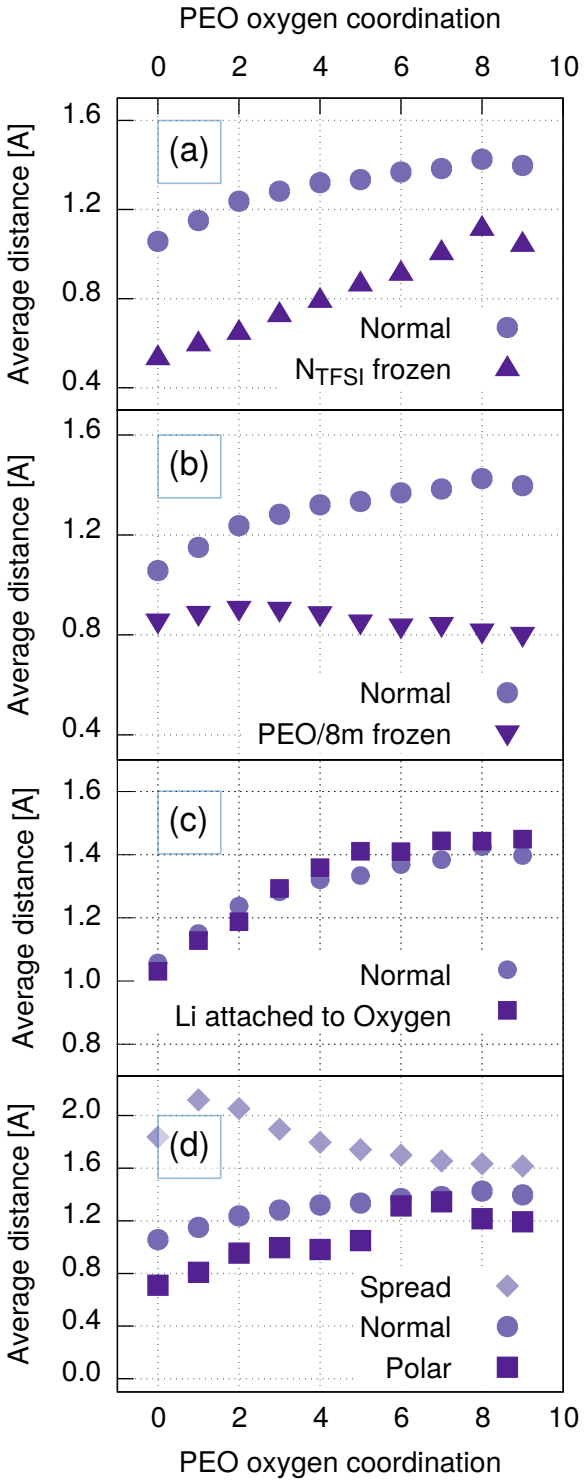


Figure 5.3.8: Molecular dynamics modifications to better understand the potential implications of four effects: 1. immobilized anion (corresponding to (a) where we freeze all the nitrogen from TFSI). 2. less mobile chains (corresponding to (b) where we freeze every PEO chain in 12 points). 3. Li atoms bonded to the closest PEO oxygen, if any is coordinated (corresponding to (c)). 4. different charge repartition on the anion (corresponding to (d) where we reorganize the charges on TFSI atoms according to Table 5.2.1).

Li mobility; this observation is supported by the literature [246, 272]. Specifically, these results can be used to speculate that any modification involving sufficiently aggressive cross-linking of PEO chains will negatively affect the cation mobility.

In the second investigation, the effect on Li of the segmental motion of the PEO chain is isolated. The procedure is as follows: 1. create a permanent bond between every Li and the closest PEO oxygen (if any are coordinating Li), 2. re-equilibrate the system with the procedure outlined in the Table 5.2.2 and 3. perform the mobility analysis. Figure 5.3.8(c) shows the results of this study. Significant differences in the mobility of Li between the normal dynamics and the simulation where every Li is attached to the closest PEO oxygen are not observed. This clearly shows that in the unmodified real system Li atoms are tightly bound to their host polymer chains. As mentioned above, the vast majority of Li is associated with a single PEO chain, and it is apparent that Li diffusion is caused by the segmental motion of the polymer. This constrained simulation thus proves that inter-chain hops are very rare events, and any motion along the host chain is much slower than the overall Li diffusion brought about by the motion of the chain itself. To verify that this behaviour is not an artefact of the limited time-scale of our simulations, longer dynamics simulations of over 200 ns are performed. During those runs, on average only one inter-chain hop event per Li is observed, which confirms that Li stays attached to a particular PEO chain for a long time, and segmental motion determines the overall Li transport[*]. A secondary conclusion is that motion of Li along the chain is not significant on this time scale.

Lastly, the partial charges of the atoms composing the TFSI anion are altered in order to obtain either a highly polar molecule or a molecule where the charge is evenly spread across all atoms, while keeping the total charge constant (see Table 5.2.1). The results on the cation mobility are illustrated in Figure 5.3.8(d). Increasing the polarity of the anion negatively affects transport properties of the polymer electrolyte system in two ways: firstly, the mobility of the Li ions is reduced across all coordination bins, and secondly the anion-cation clustering is increased (see Figure 5.3.9(a),(c)); the opposite is observed for the evenly spread case (see Figure 5.3.9(b),(d)). On the one hand, these results depend on the charge distribution chosen for the system and highlight the importance of having a

[*]No data are presented on this for information protection reasons.

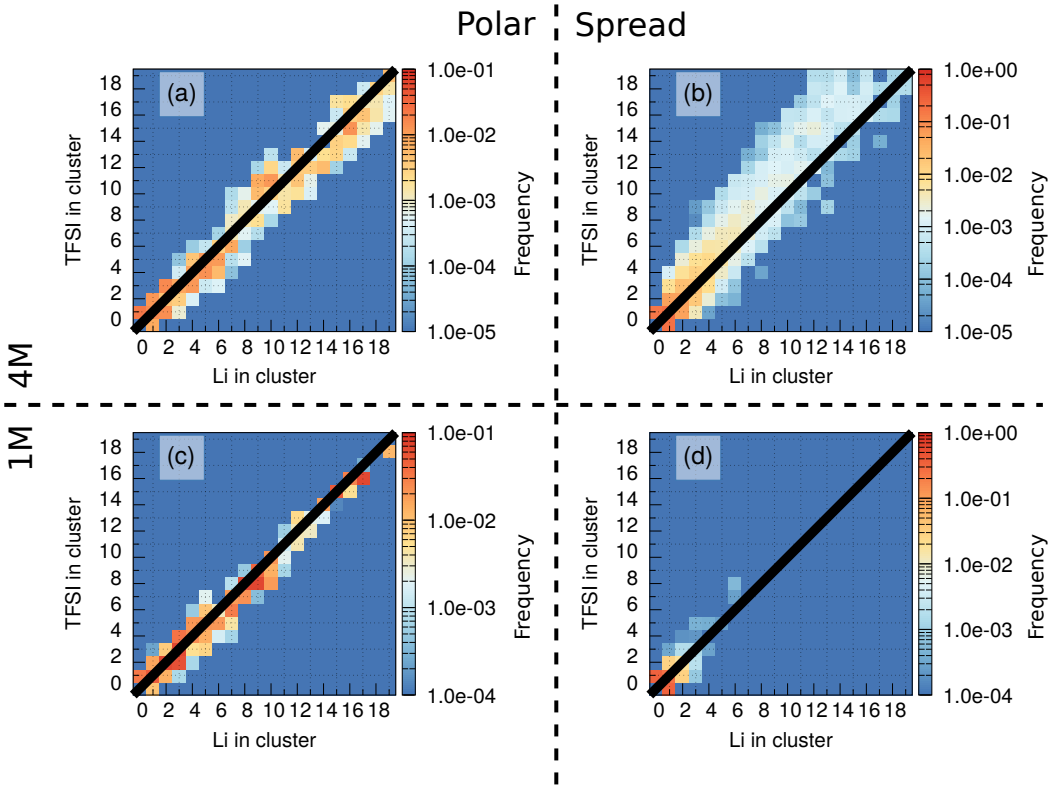


Figure 5.3.9: Cluster analysis once the point charges on the atoms composing the anion are modified according to Table 5.2.1. Top and bottom rows refer to the 4 M and 1 M, respectively. In the left column, the TFSI charges are modified so that the anion has a more polar configuration, while a more spread one is in the right column.

reliable method to determine the total and partial charges of the species involved in the simulation. On the other hand, they clearly show the importance of having an anion where the net charge is spread out as much as possible across all the atoms. This not only increases the cation mobility, but also decreases the agglomeration effect and the TFSI-LI coordinated movement.

5.4 Summary

With the use of a fully atomistic molecular dynamics model, aspects of Li coordination, ion-salt clustering and cooperative motion in the widely-used poly(ethylene)oxide

electrolyte were addressed. Three important points were found in the investigation of the Li-TFSI-PEO electrolyte.

First, the key role that the anion has in coordinating the Li cation in the system was highlighted. While this is true at both salt concentrations studied, this effect is weaker for the lower salt concentration case. On the other hand, it becomes increasingly important at practically relevant high salt concentration, resulting in the appearance of a new ensemble of cations under-coordinated by the oxygen atoms from the polymer chains. Also, the salt-coordinated Li ions also have weaker correlation with the motion of the PEO chains and are up to 40 % less mobile.

Detailed analysis further shows that the appearance of the aforementioned new ensemble of under-coordinated Li ions implies the formation of large cation-anion clusters. Such clusters show the tendency to have a larger number of anions compared to cations in their composition. This unexpected asymmetry in the clusters' composition could have a significant impact on overall transport properties of the electrolytes than the mere presence of evenly-populated clusters. The conduction of Li ions as part of negatively-charged clusters may counteract the motion of the more abundant positively charged isolated Li ions. Experimental characterization of the cluster population and detailed measurements of transference number as a function of salt concentration would be beneficial in understanding these effects.

Finally, restricting the movement of either the PEO chains or the anions has negative effects on the Li mobility. Both these modifications produce a negative impact regardless of the specific coordinating environment of Li and therefore should be avoided or minimized in any design of a PEO-based polymer electrolyte. It is also apparent that the dominant mechanism of transport even at high concentration is the segmental motion of PEO chains to which Li ions are attached for a long time, hopping only rarely and thus relying on the polymer reptation for its diffusion. Furthermore, having less polar anions has a two-fold positive effect. The first is that the mobility of Li ions increases significantly, especially for those that are TFSI-coordinated, and the second is that the clustering effect is reduced, indicating higher solubility.

6

Conclusions

From the medical and biomedical sectors to agriculture, space and automotive applications, polymers are omnipresent in our society thanks to their unique properties stemming from the immense freedom in the choice of monomers, the building blocks of polymers, as well as the insertion of (nano-)particles within the polymer matrix. The common thread among the applications presented in this dissertation is the need for a better molecular-level understanding of the strengths and weaknesses of the technological polymers currently utilised, not only to elucidate the physics, but also to help ameliorate present-day technologies. Whilst *ab initio* methods would be, in principle, more suited to describe the interatomic interactions, in practice, such approaches are unfeasible due to the limited time- and length-scales accessible using methods such as density functional theory (DFT). Instead, in this thesis I utilised classical molecular dynamics (MD) to highlight fundamental trends and to elucidate microscopic drivers of various properties in technological polymers. Thanks to parametrised analytical formulations for the potential energy surface of the systems*, MD computer simulations are able to overcome the time- and length-scales limitations of *ab initio* methods while retaining a molecular description of the polymer.

*Different analytical formulations of the potential energy surface determine the level of approximation of the system, which can range from a fine description of the interactions experienced by all the atoms in the system to effective many-atom interactions in approaches normally known as coarse-grained (CG).

I started this dissertation with chapter 2, where I presented the development of a chemically-inspired fully atomistic model with tunable cross-link density for hydrogenated nitrile butadiene rubber (HNBR), using the optimised potential for liquid simulation - all atom (OPLS-AA) force-field [127]. Elastomer seals made of HNBR are widely adopted in the oil and gas industry thanks to their resistance to fuels, heat, blistering and, in general, to the harsh conditions found at the bottom of an oil well. However, over time they cease to act as an impermeable membrane and sensitive equipments are under the threat of corrosion from the fluids permeating the seal. The development of a fully-atomistic model for HNBR is the first step towards an investigation on the solubility and diffusivity of gases through this polymer membrane, and the creation of a suitable model was the aim of this chapter. The model was tested by comparing to experiments the computed values for bulk properties, namely mass density, glass transition temperature (T_g) and bulk modulus. Despite the paucity of experimental data, the findings are in good agreement with the reported values as well as with the work of Khawaja on the precursor of HNBR: nitrile butadiene rubber (NBR).

I proceeded in chapter 3 with the investigation of the mechanical properties of polymers filled with spherical particles. Filler particles are normally included within the polymer matrix to enhance particular properties that are of interest for a specific application. All-atom models struggle to account for the insertion of multiple filler particles due to their size that, being in the order of tens or hundreds of nm, falls beyond the range of feasibility of fully-atomistic MD studies. As a result, I chose to trade chemical specificity of the model in exchange for the ability to investigate the mechanical response of polymer systems filled with hundreds of particles*, using a variant of the widely-adopted bead-spring CG model for polymer melts developed by Kremer and Grest [111]. I showed that qualitative differences exist in the stress-strain response of structures with different filler volume fraction (FVF). Furthermore, the nature of the polymer–filler network changes substantially for different filler loadings as well as during the straining of the systems. Three motifs corresponding to fillers in direct contact (BB = 0) fillers separated by one (BB = 1) and two (BB = 2) polymer chains are found

*Such compromise would have not be possible in chapter 2, where chemical specificity is central for diffusion and solubility studies [120].

composing the polymer–filler network, and this is linked to the observed differences in the mechanical response. The two main results showed that the appearance of a yield drop is related to the sudden depletion of BB $= 1$ in favour of BB $= 0, 2$, which have weaker energetic constraints as opposed to BB $= 1$. Second, for FVFs and strains exceeding 35 $\%$ and 100 $\%$, respectively, the increasing prevalence of BB $= 0$ weakens the stress-strain response, effectively signalling the existence of an optimal FVF.

In chapter 4 I investigated the potency of filler particles as universal glue for polymers. Gluing soft matter together without the use of ad-hoc designs proved to be a challenging task to tackle, and only recently a solution based on the use of nanoparticles (NPs) has been proposed and studied. However, an understanding of the interplay between quantities of central importance, such as strength of the interaction with the polymer, size, and density of the NPs is missing. In this chapter, I investigated the mechanical response of polymer melt interfaces glued together via spherical particles using CG MD. I adapted the model utilised in chapter 3 to obtain two interfaces between polymer melts separated by spherical particles with controlled size, number, and strength of the interaction with the polymer. The main result is a a non-monotonous strengthening of the stress-strain response depending on the particle size and concentration at the interface. Particles smaller than the average mesh size of the polymer can relatively easily diffuse away from the interface into the bulk. On the other hand, particles exceeding the size of the mesh of the polymer are more constrained, and layering at the interfaces is observed, resulting in a weakening of the mechanical response for large concentrations. Moreover, a simple analytical model of the melt adhesive energy has been used to explain the observed trends.

Finally, in chapter 5 I focused on a particular polymer system used in battery technology, Li-bis(trifluoromethane)sulfonimide (TFSI) dissolved in poly(ethylene)oxide (PEO). The material inserted in between the electrodes, known as the electrolyte, plays a crucial role in the safety of the overall battery, which is one of the major concerns surrounding energy storage technologies. The safety issues associated with current electrolytes are deemed acceptable for small portable devices*, however, this

*Which still bears concrete risks, as shown recently by the accident happened to a product from a leading smartphone manufacturer.

consideration changes when dealing with high-energy batteries used in, for instance, the automotive sector. Li-salt doped polymers have the potential to mitigate most of the concerns associated with safety, but current Li-salt/polymer combinations lack the cationic conductivity required to make them a viable option. Among others, Li-TFSI dissolved in PEO shows great potential. Whilst technology relevant applications require high salt concentrations, most of the works performed at the molecular level focus on the dilute limit. In this chapter I adopted fully-atomistic MD simulations to investigate 1 M and 4 M salt concentrations of Li-TFSI in PEO. When considering a highly concentrated solution, a previously undetected ensemble of Li-TFSI clusters emerges where Li ions are significantly less coordinated by the polymer. The lithium atoms trapped in such clusters have an up to 40 % loss in mobility. Moreover, the clusters formed by lithium atoms and TFSI anions have the tendency to be asymmetrical in nature, with the anions in greater number than cations, which may contribute to the low transference number of this material.

In summary, MD computer simulations are a useful tool to develop better fundamental understanding and elucidate trends in polymer physics. A characteristic of classic MD is the implementation of approximate descriptions of the potential energy landscape, from which both the strengths and weaknesses of the method stem. The use of a force-field limits the predictive power of MD investigations by removing the complex quantum mechanical degrees of freedom from the picture. At the same time, larger time- and length-scales are accessible, which is a vital condition due to the complex, and often amorphous, nature of polymers. In spite of the limitations associated with the method, MD simulations complement experiment by providing a molecular picture and mechanistic understanding otherwise difficult, if not impossible, to obtain.

6.1 Future efforts

The goal of chapter 2 was to provide an HNBR model – with chemical specificity and obtained from a NBR structure via hydrogenation and cross-link of the unsaturated double bonds – suitable to be used to investigate solubility and diffusion properties. By applying the solution-diffusion theory, this HNBR model has been used to study the

permeation of small molecules such as He, CO_2 and water through nitrile rubber [85]. A possible extension would involve studying larger diffusing molecules, such as small hydrocarbons. The study of solubility in [85] assumed no polymer relaxation during the procedure used to compute the property. While this is justifiable for small molecules [131], even small hydrocarbons would require an iterative procedure in which polymer relaxation steps are taken into account.

Another possible fruitful extension could focus on the role of filler particles on the diffusion of gases through a polymer membrane. Whether the polymer–filler interface would facilitate or hinder the diffusion of different gas molecules is unclear. Whilst a distribution of NPs dispersed within a polymer matrix is beyond the reach of fully-atomistic MD simulations, it is possible to design an atomistic simulation where only the interface of a filler particle and the polymer is investigated. This investigation would be likely to suffer from the use of an off the shelf force-field since the parameters used in the analytical formulation of a force-field are normally fitted to the bulk, without any knowledge on how an interface would behave. On the other hand, I believe this study bears great potential. First, the understanding of the precise interactions between different diffusing gas molecules and the filler–polymer interface is inherently interesting. Second, the findings could be utilised as design ideas for sink-holes NPs capable of trapping the diffusing molecules, posing an interesting solution to the problem of the permeability of elastomer seals.

Whilst some of the phenomena observed in the filled polymers studied in chapter 3 were confined at relatively high FVFs, such filler loadings are not unusual in industrial applications [92]. As a result, some of the findings could be experimentally verified. For instance, tears are found on the polymer seals brought back to surface from the bottom of the oil well. According to simulations, clusters of multiple filler particles weaken the mechanical response of the polymer nano-composite. It would be interesting to see, for example, whether experimental characterisation of the torn surface of the seal shows an enhanced concentration of NPs compared to the bulk of the seal.

Finally, the work on polymer melts adhesives presented in chapter 4 has several natural extensions. First, the shape of the inserted particles could be investigated. The findings showed the importance of the NPs organisation at the interface between the two

interfaces of the polymer melt. Different shapes of the deposited particles might self-organise in more efficient ways, resulting in increased adhesive energy and, therefore, mechanically stronger structures. Second, the work could be extended to polymer gels. In a polymer gel, a cross-linked polymer network is swollen by some fluid, resulting in a system with density close to that of the fluid, but exhibiting solid-like properties thanks to the immersed polymer. If the fluid is water, a so-called hydrogel is obtained. Thanks to the similarities with natural tissue, hydrogels are used in the medical and biomedical field for applications ranging from scaffolds in tissue engineering [273], to cell cultures [274], and biosensors [275]. NPs are experimentally proven as a viable option for gluing hydrogels [69], but a fundamental understanding of such reinforcement would be beneficial for future designs. Third, the design of the NPs could be altered. When used for medical applications, the diffusion of NPs from the interface to the bulk might lead to unwanted side-effects such as poisoning. As observed in chapter 4, the use of large NPs can prevent this at the expense of the mechanical reinforcement. A possible solution to this problem might come from the use of something more like star polymers, for which an example is sketched in Figure 6.1.1. An additional potential benefit of using a star polymer design is the ability to strengthen interfaces between two networks that differ in nature. For instance, different polymer chains can be attached to the central NP. The vast freedom in the choice of the polymer chains can be used to target different features of two polymer networks, such as chemistry and mesh size.

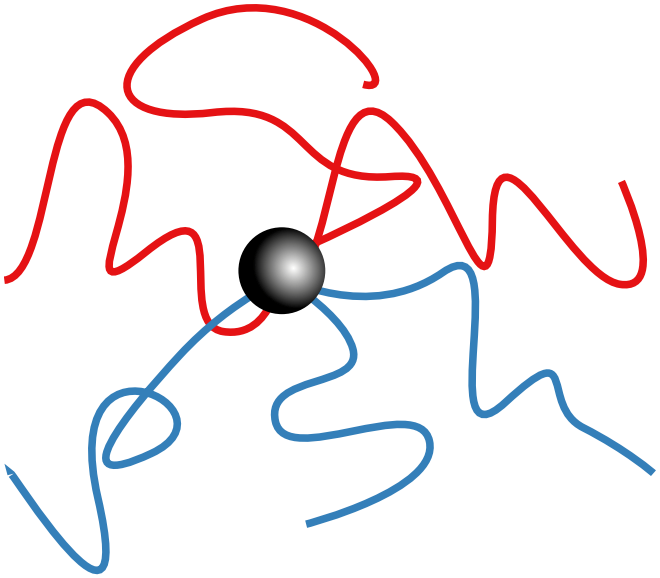


Figure 6.1.1: Sketch of a possible design for a polymer adhesive using a star polymer. At the centre, a small NP is attached to six polymer chains. The use of different (blue and red) polymer chains could be leveraged to glue together networks with different characteristics, for instance, chemistry or mesh size.

Bibliography

[1] PC Painter and MM Coleman. Fundamentals of polymer science: an introductory text. 1997.

[2] NG McCrum, CP Buckley, and CB Bucknall. *Principles of polymer engineering*. Oxford University Press, USA, 1997.

[3] F Laoutid, L Bonnaud, M Alexandre, JM Lopez-Cuesta, and PH Dubois. New prospects in flame retardant polymer materials: From fundamentals to nanocomposites. *Mater. Sci. Eng. R Reports*, 63(3):100–125, 2009. ISSN 0927796X.

[4] D Porter, E Metcalfe, and MJK Thomas. Nanocomposite fire retardants - a review. *Fire Mater.*, 24(1):45–52, 2000. ISSN 03080501. doi: 10.1002/(SICI)1099-1018(200001/02)24:1<45::AID-FAM719>3.0.CO;2-S.

[5] JM Yeh, CP Chin, and S Chang. Enhanced corrosion protection coatings prepared from soluble electronically conductive polypyrrole-clay nanocomposite materials. *J. Appl. Polym. Sci.*, 88(14):3264–3272, 2003. ISSN 00218995. doi: 10.1002/app.12146.

[6] JM Yeh, CL Chen, YC Chen, CY Ma, KR Lee, Y Wei, and S Li. Enhancement of corrosion protection effect of poly(o-ethoxyaniline) via the formation of poly(o-ethoxyaniline)–clay nanocomposite materials. *Polymer (Guildf).*, 43(9): 2729–2736, 2002. ISSN 00323861. doi: 10.1016/S0032-3861(02)00005-8.

[7] S Boutaleb, F Zaïri, A Mesbah, M Naït-Abdelaziz, JM Gloaguen, T Boukharouba, and JM Lefebvre. Micromechanics-based modelling of stiffness and yield stress for silica/polymer nanocomposites. *Int. J. Solids Struct.*, 46(7-8):1716–1726, 2009. ISSN 00207683. doi: 10.1016/j.ijsolstr.2008.12.011.

[8] P Podsiadlo, AK Kaushik, EM Arruda, AM Waas, BS Shim, J Xu, H Nandivada, BG Pumplin, J Lahann, A Ramamoorthy, and NA Kotov. Ultrastrong and stiff layered polymer nanocomposites. *Science*, 318(October):1–4, 2007. ISSN 0036-8075. doi: 10.1126/science.1143176.

[9] JR Potts, DR Dreyer, CW Bielawski, and RS Ruoff. Graphene-based polymer nanocomposites. *Polymer*, 52(1):5–25, 2011. ISSN 00323861. doi: 10.1016/j.polymer.2010.11.042.

[10] BJ Ash, LS Schadler, and RW Siegel. Glass transition behavior of alumina/polymethylmethacrylate nanocomposites. *Mater. Lett.*, 55(1-2):83–87,

2002. ISSN 0167577X. doi: 10.1016/S0167-577X(01)00626-7.

[11] D Fragiadakis, P Pissis, and L Bokobza. Glass transition and molecular dynamics in poly(dimethylsiloxane)/silica nanocomposites. *Polymer*, 46(16):6001–6008, 2005. ISSN 00323861. doi: 10.1016/j.polymer.2005.05.080.

[12] P Rittigstein, RD Priestley, LJ Broadbelt, and JM Torkelson. Model polymer nanocomposites provide an understanding of confinement effects in real nanocomposites. *Nat. Mater.*, 6(April):278–282, 2007. ISSN 1476-1122. doi: 10.1038/nmat1870.

[13] S Ramakrishna, J Mayer, E Wintermantel, and KW Leong. Biomedical applications of polymer-composite materials: a review. *Composites science and technology*, 61(9):1189–1224, 2001.

[14] A Lendlein and R Langer. Biodegradable, elastic shape-memory polymers for potential biomedical applications. *Science*, 296(5573):1673–1676, 2002.

[15] F Abbasi, H Mirzadeh, and AA Katbab. Modification of polysiloxane polymers for biomedical applications: a review. *Polymer International*, 50(12):1279–1287, 2001.

[16] HY Cheung, KT Lau, TP Lu, and D Hui. A critical review on polymer-based bio-engineered materials for scaffold development. *Composites Part B: Engineering*, 38(3):291–300, 2007.

[17] KB Prater. Solid polymer fuel cells for transport and stationary applications. *Journal of Power Sources*, 61(1-2):105–109, 1996.

[18] L Carrette, KA Friedrich, and U1 Stimming. Fuel cells–fundamentals and applications. *Fuel cells*, 1(1):5–39, 2001.

[19] HP Dhar. On solid polymer fuel cells. *Journal of Electroanalytical Chemistry*, 357 (1-2):237–250, 1993.

[20] CM Cardona, W Li, AE Kaifer, D Stockdale, and GC Bazan. Electrochemical considerations for determining absolute frontier orbital energy levels of conjugated polymers for solar cell applications. *Advanced materials*, 23(20): 2367–2371, 2011.

[21] S Günes, H Neugebauer, and NS Sariciftci. Conjugated polymer-based organic solar cells. *Chemical reviews*, 107(4):1324–1338, 2007.

[22] WU Huynh, JJ Dittmer, and AP Alivisatos. Hybrid nanorod-polymer solar cells. *science*, 295(5564):2425–2427, 2002.

[23] LC Hollaway and JG Teng. *Strengthening and rehabilitation of civil infrastructures*

using fibre-reinforced polymer (FRP) composites. Elsevier, 2008.

[24] LC Hollaway. A review of the present and future utilisation of frp composites in the civil infrastructure with reference to their important in-service properties. *Construction and Building Materials*, 24(12):2419–2445, 2010.

[25] JG Teng, T Yu, and D Fernando. Strengthening of steel structures with fiber-reinforced polymer composites. *Journal of Constructional Steel Research*, 78: 131–143, 2012.

[26] JK Borchardt. Reinforced plastics help preserve historic buildings. *Reinforced Plastics*, 47(11):30–32, 2003.

[27] RF Muraca and JS Whittick. Polymers for spacecraft applications. *NASA CR-89557*, 99, 1967.

[28] Y Liu, H Du, L Liu, and J Leng. Shape memory polymers and their composites in aerospace applications: a review. *Smart Materials and Structures*, 23(2):023001, 2014.

[29] R Chandra and R Rustgi. Biodegradable polymers. *Progress in polymer science*, 23 (7):1273–1335, 1998.

[30] P Chen, W Zhang, W Luo, and Y Fang. Synthesis of superabsorbent polymers by irradiation and their applications in agriculture. *Journal of Applied Polymer Science*, 93(4):1748–1755, 2004.

[31] J Holbery and D Houston. Natural-fiber-reinforced polymer composites in automotive applications. *JOM Journal of the Minerals, Metals and Materials Society*, 58(11):80–86, 2006.

[32] JM Garces, DJ Moll, J Bicerano, R Fibiger, and DG McLeod. Polymeric nanocomposites for automotive applications. *Advanced Materials*, 12(23): 1835–1839, 2000.

[33] A Ciesielski. *An introduction to rubber technology*. iSmithers Rapra Publishing, 1999.

[34] RF Mitchell. *Petroleum engineering handbook: drilling engineering & elektronische ressource*. Soc. of Petroleum Engineers, 2006.

[35] C Avant, S Daungkaew, BK Behera, S Danpanich, W Laprabang, ID Santo, G Heath, K Osman, ZA Khan, and J Russell. Testing the limits in extreme well conditions. *Oilfield Rev*, 24:4–19, 2012.

[36] B. hughes, annual report. http://phx.corporate-ir.net/. Accessed: 2016-12.

[37] BJ Briscoe, T Savvas, and CT Kelly. "explosive decompression failure" of rubbers:

a review of the origins of pneumatic stress induced rupture in elastomers. *Rubber chemistry and technology*, 67(3):384–416, 1994.

[38] A Stevenson and G Morgan. Fracture of elastomers by gas decompression. *Rubber Chemistry and Technology*, 68(2):197–211, 1995.

[39] AN Gent and DA Tompkins. Nucleation and growth of gas bubbles in elastomers. *Journal of applied physics*, 40(6):2520–2525, 1969.

[40] MJ Jellison, DR Hall, DC Howard, HT Hall Jr, RC Long, RB Chandler, and DS Pixton. Telemetry drill pipe: enabling technology for the downhole internet. In *SPE/IADC drilling conference*. Society of Petroleum Engineers, 2003.

[41] Baker hughes, a GE company. https://www.bhge.com/. Accessed: 2017-12.

[42] H Akamatu, H Inokuchi, and Y Matsunaga. Electrical conductivity of the perylene–bromine complex. *Nature*, 173(4395):168–169, 1954.

[43] Y Okamoto and W Brenner. Polymers, 1964.

[44] J Ferraris, DO Cowan, VT Walatka, and JH Perlstein. Electron transfer in a new highly conducting donor-acceptor complex. *Journal of the American Chemical Society*, 95(3):948–949, 1973.

[45] K Kaneto, K Yoshino, and Y Inuishi. Electrical properties of conducting polymer, poly-thiophene, prepared by electrochemical polymerization. *Japanese Journal of Applied Physics*, 21(9A):L567, 1982.

[46] M Murakami, H Yasujima, Y Yumoto, S Mizogami, and S Yoshimura. Electrical and structural properties of a new conducting polymer: Pyrolytic poly (p-phenylene-1, 3, 4-oxadiazole). *Solid state communications*, 45(12):1085–1088, 1983.

[47] J Stejskal and RG Gilbert. Polyaniline. preparation of a conducting polymer. *Pure and Applied Chemistry*, 74(5):857–867, 2002.

[48] Chabagno JM Armand MB and Duclot MJ. Second international meeting on solid electrolytes. In *Second International Meeting on Solid Electrolytes*, pages 20–22, 1978.

[49] P Vashishta, JN Mundy, and G Shenoy. Fast ion transport in solids: electrodes and electrolytes. 1979.

[50] SS Zhang. A review on the separators of liquid electrolyte li-ion batteries. *Journal of Power Sources*, 164(1):351–364, 2007.

[51] M Armand and JM Tarascon. Building better batteries. *Nature*, 451(7179): 652–657, 2008. ISSN 0028-0836. doi: 10.1038/451652a.

[52] TE Springer, TA Zawodzinski, and S Gottesfeld. Polymer electrolyte fuel cell model. *Journal of the Electrochemical Society*, 138(8):2334–2342, 1991.

[53] JM Tarascon and M Armand. Issues and challenges facing rechargeable lithium batteries. *Nature*, 414(6861):359–367, 2001.

[54] B Smitha, S Sridhar, and AA Khan. Solid polymer electrolyte membranes for fuel cell applications — a review. *Journal of membrane science*, 259(1):10–26, 2005.

[55] FM Gray. *Solid polymer electrolytes - fundamentals and technological applications*. VCH New York, 1991.

[56] B Scrosati. *Applications of electroactive polymers*, volume 75. Springer, 1993.

[57] FM Gray. *Polymer electrolytes*. Royal Society of Chemistry, 1997.

[58] JR McCallum and CA Vincent. Polymer electrolytes review-i, 1987.

[59] Tesla model s. https://www.tesla.com/. Accessed: 2017-12.

[60] M Tatsumisago, F Mizuno, and A Hayashi. All-solid-state lithium secondary batteries using sulfide-based glass–ceramic electrolytes. *Journal of power sources*, 159(1):193–199, 2006.

[61] T Minami, A Hayashi, and M Tatsumisago. Recent progress of glass and glass-ceramics as solid electrolytes for lithium secondary batteries. *Solid State Ionics*, 177(26):2715–2720, 2006.

[62] K Minami, A Hayashi, S Ujiie, and M Tatsumisago. Structure and properties of li_2s–p_2s_5–p_2s_3 glass and glass–ceramic electrolytes. *Journal of Power Sources*, 189 (1):651–654, 2009.

[63] JW Fergus. Ceramic and polymeric solid electrolytes for lithium-ion batteries. *Journal of Power Sources*, 195(15):4554–4569, 2010.

[64] WH Meyer. Polymer electrolytes for lithium-ion batteries. *Advanced materials*, 10 (6):439–448, 1998.

[65] DH Zang and W Lader. Polyisocyanate-acrylate polymer adhesives, 1970. US Patent 3,532,652.

[66] AJ Kinloch. *Adhesion and adhesives: science and technology*. Springer Science & Business Media, 2012.

[67] Y Ahn, Y Jang, N Selvapalam, G Yun, and K Kim. Supramolecular velcro for reversible underwater adhesion. *Angewandte Chemie*, 125(11):3222–3226, 2013.

[68] N Holten-Andersen, MJ Harrington, H Birkedal, BP Lee, PB Messersmith, KYC Lee, and JH Waite. ph-induced metal-ligand cross-links inspired by mussel yield self-healing polymer networks with near-covalent elastic moduli. *Proceedings of the*

National Academy of Sciences, 108(7):2651–2655, 2011. doi: 10.1073/pnas.1015862108. URL http://www.pnas.org/content/108/7/2651.abstract.

[69] S Rose, A Prevoteau, P Elziere, D Hourdet, A Marcellan, and L Leibler. Nanoparticle solutions as adhesives for gels and biological tissues. *Nature*, 505 (7483):382, 2014.

[70] JH Kim, H Kim, Y Choi, DS Lee, J Kim, and GR Yi. Colloidal mesoporous silica nanoparticles as strong adhesives for hydrogels and biological tissues. *ACS applied materials & interfaces*, 9(37):31469–31477, 2017.

[71] JF Dobson and T Gould. Calculation of dispersion energies. *Journal of Physics: Condensed Matter*, 24(7):073201, 2012.

[72] J Klimeš and A Michaelides. Perspective: Advances and challenges in treating van der waals dispersion forces in density functional theory. *The Journal of chemical physics*, 137(12):120901, 2012.

[73] A Tkatchenko and M Scheffler. Accurate molecular van der waals interactions from ground-state electron density and free-atom reference data. *Physical review letters*, 102(7):073005, 2009.

[74] S Grimme, J Antony, S Ehrlich, and H Krieg. A consistent and accurate ab initio parametrization of density functional dispersion correction (dft-d) for the 94 elements h-pu. *The Journal of chemical physics*, 132(15):154104, 2010.

[75] PL Silvestrelli. Van der waals interactions in dft made easy by wannier functions. *Physical review letters*, 100(5):053002, 2008.

[76] L Andrinopoulos, NDM Hine, and AA Mostofi. Calculating dispersion interactions using maximally localized wannier functions. *The Journal of chemical physics*, 135(15):154105, 2011.

[77] D Frenkel and B Smit. *Understanding molecular simulation: from algorithms to applications*, volume 1. Academic press, 2001.

[78] MP Allen and DJ Tildesley. *Computer simulation of liquids*. Oxford university press.

[79] DC Rapaport, RL Blumberg, SR McKay, and W Christian. The art of molecular dynamics simulation. *Computers in Physics*, 10(5):456–456, 1996.

[80] M Karplus and JA McCammon. Molecular dynamics simulations of biomolecules. *Nature Structural & Molecular Biology*, 9(9):646–652, 2002.

[81] BJ Alder, DM Gass, and TE Wainwright. Studies in molecular dynamics. viii. the transport coefficients for a hard-sphere fluid. *The Journal of Chemical Physics*, 53

(10):3813–3826, 1970.

[82] IE Fermi, P Pasta, S Ulam, and M Tsingou. Studies of the nonlinear problems. Technical report, Los Alamos Scientific Lab., N. Mex., 1955.

[83] AK Rappe and WA Goddard III. Charge equilibration for molecular dynamics simulations. *The Journal of Physical Chemistry*, 95(8):3358–3363, 1991.

[84] SJ Weiner, PA Kollman, DA Case, UC Singh, C Ghio, G Alagona, S Profeta, and P Weiner. A new force field for molecular mechanical simulation of nucleic acids and proteins. *Journal of the American Chemical Society*, 106(3):765–784, 1984.

[85] M Khawaja. Modelling the permeability of nitrile rubber. 2016.

[86] B Kopey. Development of drilling technics from ancient ages to modern times. In *12th IFToMM World Congress, Besançon, France*, 2007.

[87] Webplotdigitizer (github). https://github.com/ankitrohatgi/WebPlotDigitizer. Accessed: 2017-11.

[88] Bentonite powder. http://www.reade.com/. Accessed: 2017-11.

[89] V Mahto and VP Sharma. Rheological study of a water based oil well drilling fluid. *Journal of Petroleum Science and Engineering*, 45(1):123–128, 2004.

[90] JP Nguyen. *Drilling: oil and gas field development techniques*. Éditions Technip, 1996.

[91] JW Hosterman. Bentonite and fuller's earth resources of the united states. Technical report, 1985.

[92] Baker hughes - personal communication.

[93] Standard terminology relating to rubber. http://enterprise.astm.org/. Accessed: 2017-11.

[94] CE Grethlein, BD Craig, and RA Lane. Elastomeric seals 101-a brief tutorial. *The AMPTIAC Quarterly, New York*, 8:10, 2004.

[95] D Chandler. Introduction to modern statistical mechanics. *A basic statistical mechanics textbook emphasizing fluids, phase transitions and reactions, written in the age of computer simulations*.

[96] M Doi. *Introduction to polymer physics*. Oxford university press, 1996.

[97] LH Sperling. *Introduction to physical polymer science*. John Wiley & Sons, 2005.

[98] T Eduard and K Erich. Rubber like masses from butadiene hydrocarbons and polymerizable nitriles, 1934. US Patent 1,973,000.

[99] H Wang, L Yang, and GL Rempel. Homogeneous hydrogenation art of nitrile

butadiene rubber: a review. *Polymer Reviews*, 53(2):192–239, 2013.

[100] D Mackey and AH Jorgensen. Nitrile rubber. *Kirk-Othmer Encyclopedia of Chemical Technology*, 2001.

[101] International institute of synthetic rubber producers - nbr. http://www.iisrp.com/, . Accessed: 2014-08.

[102] NK Singha, S Bhattacharjee, and S Sivaram. Hydrogenation of diene elastomers, their properties and applications: a critical review. *Rubber chemistry and technology*, 70(3):309–367, 1997.

[103] MB Bastrzyk, CC Daniels, JJ Oswald, PH Dunlap Jr, and BM Steinetz. Material properties of three candidate elastomers for space seals applications. 2010.

[104] K Nagdi. *Rubber as an engineering material: guideline for users*. Hanser Verlag, 1993.

[105] AK Bhowmick. *Rubber products manufacturing technology*. CRC Press, 1994.

[106] JL Graham, RC Striebich, KJ Myers, DK Minus, and WE Harrison. Swelling of nitrile rubber by selected aromatics blended in a synthetic jet fuel. *Energy & fuels*, 20(2):759–765, 2006.

[107] PC Painter and MM Coleman. *Fundamentals of polymer science: an introductory text*. Technomic, 1994.

[108] International institute of synthetic rubber producers - hnbr. http://iisrp.com/, . Accessed: 2014-08.

[109] T Yamada, JL Graham, and DK Minus. Density functional theory investigation of the interaction between nitrile rubber and fuel species. *Energy & Fuels*, 23(1): 443–450, 2008.

[110] DR Alfonso and AV Cugini. Ab initio study of interaction of a model nitrile polymer with various model fuel molecules. *Prepr. Pap.-Am. Chem. Soc., Div. Fuel Chem*, 48(2):508, 2003.

[111] K Kremer and GS Grest. Dynamics of entangled linear polymer melts: A molecular-dynamics simulation. *The Journal of Chemical Physics*, 92(8): 5057–5086, 1990.

[112] HR Warner Jr. Kinetic theory and rheology of dilute suspensions of finitely extendible dumbbells. *Industrial & Engineering Chemistry Fundamentals*, 11(3): 379–387, 1972.

[113] G Milano and F Müller-Plathe. Mapping atomistic simulations to mesoscopic models: A systematic coarse-graining procedure for vinyl polymer chains. *The Journal of Physical Chemistry B*, 109(39):18609–18619, 2005.

[114] D Fritz, VA Harmandaris, K Kremer, and NFA van der Vegt. Coarse-grained polymer melts based on isolated atomistic chains: Simulation of polystyrene of different tacticities. *Macromolecules*, 42(19):7579–7588, 2009.

[115] VA Harmandaris, NP Adhikari, NFA van der Vegt, and K Kremer. Hierarchical modeling of polystyrene: From atomistic to coarse-grained simulations. *Macromolecules*, 39(19):6708–6719, 2006.

[116] HJ Qian, P Carbone, X Chen, HA Karimi-Varzaneh, CC Liew, and F Müller-Plathe. Temperature-transferable coarse-grained potentials for ethylbenzene, polystyrene, and their mixtures. *Macromolecules*, 41(24): 9919–9929, 2008.

[117] G Rossi, L Monticelli, SR Puisto, I Vattulainen, and T Ala-Nissila. Coarse-graining polymers with the martini force-field: polystyrene as a benchmark case. *Soft Matter*, 7(2):698–708, 2011.

[118] Q Sun and R Faller. Crossover from unentangled to entangled dynamics in a systematically coarse-grained polystyrene melt. *Macromolecules*, 39(2):812–820, 2006.

[119] HA Karimi-Varzaneh, NFA van der Vegt, F Müller-Plathe, and P Carbone. How good are coarse-grained polymer models? a comparison for atactic polystyrene. *ChemPhysChem*, 13(15):3428–3439, 2012.

[120] M Khawaja, AP Sutton, and AA Mostofi. Molecular simulation of gas solubility in nitrile butadiene rubber. *The Journal of Physical Chemistry B*, 121(1):287–297, 2016.

[121] E Kucukpinar and P Doruker. Molecular simulations of gas transport in nitrile rubber and styrene butadiene rubber. *Polymer*, 47:7835–7845, 2006. ISSN 00323861. doi: 10.1016/j.polymer.2006.08.062.

[122] M Song, X Zhao, Y Li, S Hu, L Zhang, and S Wu. Molecular dynamics simulations and microscopic analysis of the damping performance of hindered phenol ao-60/nitrile-butadiene rubber composites. *RSC Advances*, 4(13):6719–6729, 2014.

[123] M Song, X Zhao, Y Li, TW Chan, L Zhang, and S Wu. Effect of acrylonitrile content on compatibility and damping properties of hindered phenol ao-60/nitrile-butadiene rubber composites: molecular dynamics simulation. *RSC Advances*, 4(89):48472–48479, 2014.

[124] B Qiao, X Zhao, D Yue, L Zhang, and S Wu. A combined experiment and molecular dynamics simulation study of hydrogen bonds and free volume in

nitrile-butadiene rubber/hindered phenol damping mixtures. *Journal of Materials Chemistry*, 22(24):12339–12348, 2012.

[125] H Sun, P Ren, and JR Fried. The compass force field: parameterization and validation for phosphazenes. *Computational and Theoretical Polymer Science*, 8(1): 229–246, 1998.

[126] Biovia materials studio. http://accelrys.com/. Accessed: 2016-12.

[127] WL Jorgensen, DS Maxwell, and J Tirado-Rives. Development and testing of the opls all-atom force field on conformational energetics and properties of organic liquids. *J. Am. Chem. Soc*, 118(45):11225–11236, 1996.

[128] WJ Roff and JR Scott. *Fibres, films, plastics and rubbers: a handbook of common polymers*. Elsevier, 2013.

[129] AK Bhowmick and H Stephens. *Handbook of elastomers*. CRC Press, 2000.

[130] M Doi and SF Edwards. *The theory of polymer dynamics*, volume 73. oxford university press, 1988.

[131] F Müller-Plathe. Permeation of polymers — a computational approach. *Acta Polymerica*, 45(4):259–293, 1994.

[132] DN Theodorou and UW Suter. Detailed molecular structure of a vinyl polymer glass. *Macromolecules*, 18(7):1467–1478, 1985.

[133] N Molinari, M Khawaja, AP Sutton, and AA Mostofi. Molecular model for HNBR with tunable cross-link density. *J. Phys. Chem. B*, page acs.jpcb.6b07841, 2016. ISSN 1520-6106. doi: 10.1021/acs.jpcb.6b07841.

[134] G Severe and JL White. Physical properties and blend miscibility of hydrogenated acrylonitrile-butadiene rubber. *Journal of applied polymer science*, 78(8): 1521–1529, 2000.

[135] DC Doherty, BN Holmes, P Leung, and RB Ross. Polymerization molecular dynamics simulations. i. cross-linked atomistic models for poly (methacrylate) networks. *Computational and Theoretical Polymer Science*, 8(1-2):169–178, 1998.

[136] B Arab, A Shokuhfar, and S Ebrahimi-Nejad. Glass transition temperature of cross-linked epoxy polymers: a molecular dynamics study. In *Proceedings of the International Conference Nanomaterials: Applications and Properties*, number 1, no. 1, pages 01NDLCN11–01NDLCN11. Sumy State University Publishing, 2012.

[137] DR Rottach, JG Curro, J Budzien, GS Grest, C Svaneborg, and R Everaers. Molecular dynamics simulations of polymer networks undergoing sequential cross-linking and scission reactions. *Macromolecules*, 40(1):131–139, 2007.

[138] E Bitzek, P Koskinen, F Gähler, M Moseler, and P Gumbsch. Structural relaxation made simple. *Physical review letters*, 97(17):170201, 2006.

[139] E Kucukpinar and P Doruker. Molecular simulations of small gas diffusion and solubility in copolymers of styrene. *Polymer*, 44(12):3607–3620, 2003.

[140] S Plimpton. Fast parallel algorithms for short-range molecular dynamics, 1995. ISSN 00219991.

[141] BG Willoughby. A structural analysis of nitrile rubbers—the 13c resonance technique. *Polymer testing*, 8(1):45–70, 1988.

[142] AE Robinson, JV Marra, and LO Amberg. Ethylene-propylene rubber vulcanization with aralkyl peroxide and coagents. *Industrial & Engineering Chemistry Product Research and Development*, 1(2):78–82, 1962.

[143] WG Hoover. Canonical dynamics: equilibrium phase-space distributions. *Physical review A*, 31(3):1695, 1985.

[144] S Nosé. A unified formulation of the constant temperature molecular dynamics methods. *The Journal of chemical physics*, 81(1):511–519, 1984.

[145] HC Andersen. Molecular dynamics simulations at constant pressure and/or temperature. *The Journal of chemical physics*, 72(4):2384–2393, 1980.

[146] WG Hoover. Constant-pressure equations of motion. *Physical Review A*, 34(3): 2499, 1986.

[147] L Verlet. Computer" experiments" on classical fluids. i. thermodynamical properties of lennard-jones molecules. *Physical review*, 159(1):98, 1967.

[148] WC Swope, HC Andersen, PH Berens, and KR Wilson. A computer simulation method for the calculation of equilibrium constants for the formation of physical clusters of molecules: application to small water clusters. *The Journal of Chemical Physics*, 76(1):637–649, 1982.

[149] JP Ryckaert, G Ciccotti, and HJC Berendsen. Numerical integration of the cartesian equations of motion of a system with constraints: molecular dynamics of n-alkanes. *Journal of Computational Physics*, 23(3):327–341, 1977.

[150] Arlanxeo - performance elastomer. http://baypren.com/, . Accessed: 2017-11.

[151] Therban - hnbr brochure. http://therban.com/, . Accessed: 2016-12.

[152] WJ Roff, JR Scott, and J Pacitti. Handbook of common polymers. *Fibers, Films, Plastics and Rubbers," CRC Press, 688p*, 1971.

[153] RC Klingender. *Handbook of specialty elastomers*. CRC Press, 2008.

[154] Qingchun Fan and Chaobo Xiao. Effects of crosslinking density on structure and

properties of interpenetrating polymer networks from polyurethane and nitroguar gum. *Polymer Composites*, 29(7):758–767, 2008.

[155] AA Askadskii. Influence of crosslinking density on the properties of polymer networks. *Polymer science USSR*, 32(10):2061–2069, 1990.

[156] FD Murnaghan. The compressibility of media under extreme pressures. *Proceedings of the National Academy of Sciences*, 30(9):244–247, 1944.

[157] F Birch. Finite elastic strain of cubic crystals. *Physical Review*, 71(11):809, 1947.

[158] PS Ku. Equations of state of organic high polymers. Technical report, GENERAL ELECTRIC CO PHILADELPHIA PA MISSILE AND SPACE DIV, 1968.

[159] JE Mark. *Physical properties of polymers handbook*, volume 1076. Springer, 2007.

[160] JM Arguello and A Santos. Hardness and compression resistance of natural rubber and synthetic rubber mixtures. In *Journal of Physics: Conference Series*, volume 687, page 012088. IOP Publishing, 2016.

[161] RW Warfield and FR Barnet. Elastic constants of bulk polymers. Technical report, NAVAL ORDNANCE LAB WHITE OAK MD, 1972.

[162] Inc. Bangs Laboratories. Material properties of polystyrene and poly(methyl methacrylate) (pmma) microspheres. Technical report, 2015.

[163] R Kono. The dynamic bulk viscosity of polystyrene and polymethyl methacrylate. *Journal of the Physical Society of Japan*, 15(4):718–725, 1960.

[164] PG Debenedetti and FH Stillinger. Supercooled liquids and the glass transition. *Nature*, 410(6825):259–267, 2001.

[165] CA Angell, KL Ngai, GB McKenna, PF McMillan, and SW Martin. Relaxation in glassforming liquids and amorphous solids. *Journal of Applied Physics*, 88(6): 3113–3157, 2000.

[166] MI Ojovan. Glass formation in amorphous sio_2 as a percolation phase transition in a system of network defects. *JETP letters*, 79(12):632–634, 2004.

[167] R Feynman. Report of the presidential commission on the space shuttle challenger accident. 1986.

[168] J Han, RH Gee, and RH Boyd. Glass transition temperatures of polymers from molecular dynamics simulations. *Macromolecules*, 27(26):7781–7784, 1994.

[169] A Simperler, A Kornherr, R Chopra, PA Bonnet, W Jones, WDS Motherwell, and G Zifferer. Glass transition temperature of glucose, sucrose, and trehalose: an experimental and in silico study. *The Journal of Physical Chemistry B*, 110(39): 19678–19684, 2006.

[170] Therban advanced technology. the new low molecular weight hnbr. http://www.plastverarbeiter.de/. Accessed: 2016-12.

[171] J Brandrup, EH Immergut, EA Grulke, A Abe, and DR Bloch. *Polymer handbook*, volume 7. Wiley New York etc, 1989.

[172] A Soldera. Comparison between the glass transition temperatures of the two pmma tacticities: a molecular dynamics simulation point of view. In *Macromolecular Symposia*, volume 133, pages 21–32. Wiley Online Library, 1998.

[173] MLD Ediger, CA Angell, and SR Nagel. Supercooled liquids and glasses. *The journal of physical chemistry*, 100(31):13200–13212, 1996.

[174] DR Burfield. Polymer glass transition temperatures. *Journal of Chemical Education*, 64(10):875, 1987. doi: 10.1021/ed064p875. URL http://dx.doi.org/10.1021/ed064p875.

[175] AM Bueche. Filler reinforcement of silicone rubber. *Journal of Polymer Science Part A: Polymer Chemistry*, 25(109):139–149, 1957.

[176] Polymer nanocomposites market by type (carbon nanotubes, nanoclays, metal oxide, ceramics), application (construction, automotive, electrical & electronics, packaging) - global opportunity analysis and industry forecast, 2014-2022.

[177] LS Schadler, LC Brinson, and WG Sawyer. Polymer nanocomposites: a small part of the story. *JOM Journal of the Minerals, Metals and Materials Society*, 59(3): 53–60, 2007.

[178] LS Schadler. *Polymer-Based and Polymer-Filled Nanocomposites*. Wiley Online Library, 2003.

[179] MZ Rong, MQ Zhang, and WH Ruan. Surface modification of nanoscale fillers for improving properties of polymer nanocomposites: a review. *Materials science and technology*, 22(7):787–796, 2006.

[180] L Huang, X Yang, X Jia, and D Cao. Fracture mechanism of amorphous polymers at strain fields. *Phys. Chem. Chem. Phys.*, 16(45):24892–8, 2014. ISSN 1463-9084. doi: 10.1039/c4cp03120b.

[181] J Li, T Mulder, B Vorselaars, AV Lyulin, and MAJ Michels. Monte Carlo simulation of uniaxial tension of an amorphous polyethylene-like polymer glass. *Macromolecules*, 39(22):7774–7782, 2006. ISSN 00249297. doi: 10.1021/ma061042w.

[182] D Hossain, MA Tschopp, DK Ward, JL Bouvard, P Wang, and MF Horstemeyer. Molecular dynamics simulations of deformation mechanisms of amorphous polyethylene. *Polymer*, 51(25):6071–6083, nov 2010. ISSN 00323861. doi:

10.1016/j.polymer.2010.10.009.

[183] S Lee and GC Rutledge. Plastic deformation of semicrystalline polyethylene by molecular simulation. *Macromolecules*, 44(8):3096–3108, 2011. ISSN 00249297. doi: 10.1021/ma1026115.

[184] RS Hoy and MO Robbins. Strain hardening in polymer glasses: Limitations of network models. *Phys. Rev. Lett.*, 99(11):1–4, 2007. ISSN 00319007. doi: 10.1103/PhysRevLett.99.117801.

[185] RS Hoy and MO Robbins. Strain hardening of polymer glasses: Entanglements, energetics, and plasticity. *Phys. Rev. E*, 77(March):1–14, 2008. doi: 10.1103/PhysRevE.77.031801.

[186] RS Hoy and MO Robbins. Strain hardening in bidisperse polymer glasses: Separating the roles of chain orientation and interchain entanglement. *J. Chem. Phys.*, 131(24), 2009. ISSN 00219606. doi: 10.1063/1.3276800.

[187] RS Hoy and CS O'hern. Viscoplasticity and large-scale chain relaxation in glassy-polymeric strain hardening. *Phys. Rev. E - Stat. Nonlinear, Soft Matter Phys.*, 82(4):1–10, 2010. ISSN 15393755. doi: 10.1103/PhysRevE.82.041803.

[188] K Nayak, DJ Read, TCB McLeish, PJ Hine, and M Tassieri. A coarse-grained molecular model of strain-hardening for polymers in the marginally glassy state. *J. Polym. Sci. Part B Polym. Phys.*, 49(13):920–938, 2011. ISSN 08876266. doi: 10.1002/polb.22263.

[189] G Allegra, G Raos, and M Vacatello. Theories and simulations of polymer-based nanocomposites: From chain statistics to reinforcement. *Prog. Polym. Sci.*, 33: 683–731, 2008. ISSN 00796700. doi: 10.1016/j.progpolymsci.2008.02.003.

[190] J Liu, L Zhang, D Cao, J Shen, and Y Gao. Computational simulation of elastomer nanocomposites: current progress and future challenges. *Rubber Chem. Technol.*, 85(3):450–481, 2012. ISSN 0035-9475. doi: 10.5254/rct.12.87966.

[191] V Ganesan and A Jayaraman. Theory and simulation studies of effective interactions, phase behavior and morphology in polymer nanocomposites. *Soft Matter*, 10(1):13–38, 2014. ISSN 1744-6848. doi: 10.1039/c3sm51864g.

[192] A Karatrantos, N Clarke, and M Kröger. Modeling of polymer structure and conformations in polymer nanocomposites from atomistic to mesoscale: a review. *Polym. Rev.*, 3724(AUGUST):1–44, 2016. ISSN 1558-3724. doi: 10.1080/15583724.2015.1090450.

[193] PG De Gennes. Dynamics of entangled polymer solutions. i. the rouse model. *Macromolecules*, 9(4):587–593, 1976.

[194] PG De Gennes. *Scaling concepts in polymer physics*. Cornell university press, 1979.

[195] G Raos, M Moreno, and S Elli. Computational experiments on filled rubber viscoelasticity: What is the role of particle - Particle interactions? *Macromolecules*, 39(19):6744–6751, 2006. ISSN 00249297. doi: 10.1021/ma061008h.

[196] G Raos and M Casalegno. Nonequilibrium simulations of filled polymer networks: Searching for the origins of reinforcement and nonlinearity. *J. Chem. Phys.*, 134(5), 2011. ISSN 00219606. doi: 10.1063/1.3537971.

[197] J Shen, J Liu, Y Gao, X Li, and L Zhang. Elucidating and tuning the strain-induced non-linear behavior of polymer nanocomposites: a detailed molecular dynamics simulation study. *Soft Matter*, 10:5099–113, 2014. ISSN 1744-6848. doi: 10.1039/c4sm00233d.

[198] J Shen, J Liu, H Li, Y Gao, X Li, Y Wu, and L Zhang. Molecular dynamics simulations of the structural, mechanical and visco-elastic properties of polymer nanocomposites filled with grafted nanoparticles. *Phys. Chem. Chem. Phys.*, 17 (11):7196–207, 2015. ISSN 1463-9084. doi: 10.1039/c4cp05520a.

[199] J Liu, L Zhang, D Cao, and W Wang. Static, rheological and mechanical properties of polymer nanocomposites studied by computer modeling and simulation. *Phys. Chem. Chem. Phys.*, 11(48):11365–11384, 2009. ISSN 1463-9076. doi: 10.1039/b913511a.

[200] J Liu, S Wu, L Zhang, W Wang, and D Cao. Molecular dynamics simulation for insight into microscopic mechanism of polymer reinforcement. *Phys. Chem. Chem. Phys.*, 13(2):518–29, jan 2011. ISSN 1463-9084. doi: 10.1039/cocp00297f.

[201] J Liu, J Shen, Y Gao, H Zhou, Y Wu, and L Zhang. Detailed simulation of the role of functionalized polymer chains on the structural, dynamic and mechanical properties of polymer nanocomposites. *Soft Matter*, 10(44):8971–8984, 2014. ISSN 1744-683X. doi: 10.1039/C4SM02005G.

[202] JD Weeks, D Chandler, and HC Andersen. Role of repulsive forces in determining the equilibrium structure of simple liquids. *J. Chem. Phys.*, 54(12):5237–5247, 1971.

[203] William H, Andrew D, and Klaus S. VMD – Visual Molecular Dynamics. *Journal of Molecular Graphics*, 14:33–38, 1996.

[204] L Yang, DJ Srolovitz, and AF Yee. Extended ensemble molecular dynamics method for constant strain rate uniaxial deformation of polymer systems. *J. Chem. Phys.*, 107(11):4396, 1997. ISSN 00219606. doi: 10.1063/1.474781.

[205] J Gao and JH Weiner. Simulated polymer melt stress relaxation. II. Search for

entanglements. *J. Chem. Phys.*, 103(4):1621, 1995. ISSN 00219606. doi: 10.1063/1.469733.

[206] J Liu, S Wu, D Cao, and L Zhang. Effects of pressure on structure and dynamics of model elastomers: a molecular dynamics study. *The Journal of chemical physics*, 129 (15):154905, 2008.

[207] EA Appel and OA Scherman. Gluing gels: A nanoparticle solution. *Nature materials*, 13:231–232, 2014.

[208] PG De Gennes. *Scaling concepts in polymer physics*. Cornell university press, 1979.

[209] JH Kim, H Kim, Y Choi, DS Lee, J Kim, and GR Yi. Colloidal mesoporous silica nanoparticles as strong adhesives for hydrogels and biological tissues. *ACS applied materials & interfaces*, 9(37):31469–31477, 2017.

[210] Hallstar. Anti-tacks. Technical report. Accessed: 2018-01.

[211] Z Cao and AV Dobrynin. Nanoparticles as adhesives for soft polymeric materials. *Macromolecules*, 49(9):3586–3592, 2016.

[212] AN Gent, GR Hamed, and WJ Hung. Adhesion of elastomer layers to an interposed layer of filler particles. *The Journal of Adhesion*, 79(10):905–913, 2003.

[213] C Nah, J Jose, JH Ahn, YS Lee, and AN Gent. Adhesion of carbon black to elastomers. *Polymer Testing*, 31(2):248–253, 2012.

[214] S Angioletti-Uberti. Theory, simulations and the design of functionalized nanoparticles for biomedical applications: A soft matter perspective. *npj Computational Materials*, 3(1):48, 2017.

[215] The history of the electric car. https://energy.gov/. Accessed: 2017-10.

[216] TA Edison. Reversible galvanic battery., 1901. URL `https://www.google.com/patents/US678722`. US Patent 678,722.

[217] TA Edison. Reversible galvanic battery., 1902. URL `https://www.google.com/patents/US692507`. US Patent 692,507.

[218] Electric car evolution. https://cleantechnica.com/. Accessed: 2017-07.

[219] Electrical apparatus and supplies. https://www2.census.gov/. Accessed: 2017-07.

[220] F Clymer. *Henry's wonderful model T 1908-1927*. 1955.

[221] F Clymer. *Treasury of early American automobiles, 1877-1925*. McGraw-Hill, 1950.

[222] J Erjavec. *Hybrid, electric, and fuel-cell vehicles*. Cengage Learning, 2012.

[223] T Denton. *Electric and hybrid vehicles*. Taylor & Francis, 2016. ISBN 9781317552512. URL

https://books.google.co.uk/books?id=hFnlCwAAQBAJ.

[224] Inventory of u.s. greenhouse gas emissions and sinks: 1990–2015. https://www.epa.gov/. Accessed: 2017-11.

[225] S Dhar, F Albano, S Venkatesan, W Koetting, F Martin, and L Higley. Lead-acid battery with high power density and energy density, 2013. URL https://www.google.com/patents/US20130309550. US Patent App. 13/475,484.

[226] Electricity storage. https://iea-etsap.org/. Accessed: 2017-10.

[227] DE Sadava, DM Hillis, HC Heller, and M Berenbaum. *Life: the science of biology*, volume 2. Macmillan, 2009.

[228] SP Parker. *McGraw-Hill encyclopedia of science & technology*. McGraw-Hill Companies, 1997.

[229] Y Demirel. *Energy and energy types*, pages 27–70. Springer London, London, 2012. ISBN 978-1-4471-2372-9. doi: 10.1007/978-1-4471-2372-9_2.

[230] Energy density calculations of nuclear fuel. https://whatisnuclear.com/. Accessed: 2017-07.

[231] JD Huba. Nrl (naval research laboratory) plasma formulary, revised. *Naval Research Lab. Report*, 2016.

[232] Y Reynier, R Yazami, and B Fultz. Xrd evidence of macroscopic composition inhomogeneities in the graphite–lithium electrode. *Journal of power sources*, 165 (2):616–619, 2007.

[233] J Kohanoff, G Galli, and M Parrinello. Theoretical study of lic6. *Le Journal de Physique IV*, 1(C5):C5–351, 1991.

[234] Y Qi, H Guo, LG Hector, and A Timmons. Threefold increase in the young's modulus of graphite negative electrode during lithium intercalation. *Journal of The Electrochemical Society*, 157(5):A558–A566, 2010.

[235] D Larcher, S Beattie, M Morcrette, K Edstroem, JC Jumas, and JM Tarascon. Recent findings and prospects in the field of pure metals as negative electrodes for li-ion batteries. *Journal of Materials Chemistry*, 17(36):3759–3772, 2007.

[236] LY Beaulieu, KW Eberman, RL Turner, LJ Krause, and JR Dahn. Colossal reversible volume changes in lithium alloys. *Electrochemical and Solid-State Letters*, 4(9):A137–A140, 2001.

[237] A Timmons and JR Dahn. Isotropic volume expansion of particles of amorphous metallic alloys in composite negative electrodes for li-ion batteries. *Journal of The*

Electrochemical Society, 154(5):A444–A448, 2007.

[238] DE Fenton, JM Parker, and PV Wright. Complexes of alkali metal ions with poly (ethylene oxide). *polymer*, 14(11):589, 1973.

[239] H Yang, K Kwon, TM Devine, and JW Evans. Aluminum corrosion in lithium batteries an investigation using the electrochemical quartz crystal microbalance. *Journal of The Electrochemical Society*, 147(12):4399–4407, 2000.

[240] E Quartarone, P Mustarelli, and A Magistris. Peo-based composite polymer electrolytes. *Solid State Ionics*, 110(1):1–14, 1998.

[241] Z Gadjourova, YG Andreev, DP Tunstall, and PG Bruce. Ionic conductivity in crystalline polymer electrolytes. *Nature*, 412(6846):520–523, 2001.

[242] Z Xue, D He, and X Xie. Poly (ethylene oxide)-based electrolytes for lithium-ion batteries. *Journal of Materials Chemistry A*, 3(38):19218–19253, 2015.

[243] S Lascaud, M Perrier, A Vallee, S Besner, J Prud'Homme, and M Armand. Phase diagrams and conductivity behavior of poly (ethylene oxide)-molten salt rubbery electrolytes. *Macromolecules*, 27(25):7469–7477, 1994.

[244] MA Webb, Y Jung, DM Pesko, BM Savoie, U Yamamoto, GW Coates, NP Balsara, ZG Wang, and TF Miller. Systematic computational and experimental investigation of lithium-ion transport mechanisms in polyester-based polymer electrolytes. *ACS Cent. Sci.*, page 150710000100007, 2015. ISSN 2374-7943. doi: 10.1021/acscentsci.5b00195.

[245] O Borodin, R Douglas, GA Smith, F Trouw, and S Petrucci. MD Simulations and experimental study of structure, dynamics, and thermodynamics of poly(ethylene oxide) and its oligomers. *J. Phys. Chem. B*, 107(28):6813–6823, 2003. doi: Doi10.1021/Jp0275387.

[246] Y Duan, JW Halley, L Curtiss, and P Redfern. Mechanisms of lithium transport in amorphous polyethylene oxide. *J. Chem. Phys.*, 122(5), 2005. ISSN 00219606. doi: 10.1063/1.1839555.

[247] D Diddens, A Heuer, and O Borodin. Understanding the lithium transport within a rouse-based model for a PEO/LiTFSI polymer electrolyte. *Macromolecules*, 43 (4):2028–2036, 2010. ISSN 00249297. doi: 10.1021/ma901893h.

[248] S Neyertz and D Brown. Local structure and mobility of ions in polymer electrolytes: A molecular dynamics simulation study of the amorphous PEOxNaI system. *J. Chem. Phys.*, 104(10):3797, 1996. ISSN 00219606. doi: 10.1063/1.471033.

[249] F Müller-Plathe and WF van Gunsteren. Computer simulation of a polymer

electrolyte: Lithium iodide in amorphous poly(ethylene oxide). *J. Chem. Phys.*, 103(11):4745–4756, 1995. ISSN 00219606. doi: 10.1063/1.470611.

[250] O Borodin and GD Smith. Mechanism of ion transport in amorphous poly(ethylene oxide)/LiTFSI from molecular dynamics simulations. *Macromolecules*, 39(4):1620–1629, 2006. ISSN 0024-9297. doi: 10.1021/ma052277v.

[251] S Mogurampelly, O Borodin, and V Ganesan. Computer simulations of ion transport in polymer electrolyte membranes. *Annu. Rev. Chem. Biomol. Eng*, 7: 349–71, 2016. ISSN 1947-5438.

[252] M Joost, M Kunze, S Jeong, M Schönhoff, M Winter, and S Passerini. Ionic mobility in ternary polymer electrolytes for lithium-ion batteries. *Electrochim. Acta*, 86:330–338, 2012. ISSN 00134686. doi: 10.1016/j.electacta.2012.03.084.

[253] D Diddens and A Heuer. Simulation study of the lithium ion transport mechanism in ternary polymer electrolytes: the critical role of the segmental mobility. *J. Phys. Chem. B*, 118(4):1113–1125, 2014. ISSN 1520-5207. doi: 10.1021/jp409800r.

[254] TGA Youngs and C Hardacre. Application of static charge transfer within an ionic-liquid force field and its effect on structure and dynamics. *Chem. Phys. Chem.*, 9(11):1548–1558, 2008. ISSN 14394235. doi: 10.1002/cphc.200800200.

[255] AA Teran and NP Balsara. Thermodynamics of block copolymers with and without salt. *J. Phys. Chem. B*, 118(1):4–17, 2013.

[256] DR Wheeler and J Newman. Molecular dynamics simulations of multicomponent diffusion. 1. equilibrium method. *J. Phys. Chem. B*, 108(47):18353–18361, 2004.

[257] JP Hansen and IR McDonald. Self-diffusion and electrical conductance in a simple molten salt. *Journal of Physics C: Solid State Physics*, 7(21):L384, 1974.

[258] R Zwanzig. Elementary derivation of time-correlation formulas for transport coefficients. *The Journal of Chemical Physics*, 40(9):2527–2533, 1964.

[259] L Boltzmann. *Vorlesungen über gastheorie*, volume 1. JA Barth, 1896.

[260] D Brandell, P Priimägi, H Kasemägi, and A Aabloo. Branched polyethylene/poly(ethylene oxide) as a host matrix for Li-ion battery electrolytes: a molecular dynamics study. *Electrochim. Acta*, 57(1):228–236, 2011. ISSN 00134686. doi: 10.1016/j.electacta.2011.03.022.

[261] G Orädd, L Edman, and A Ferry. Diffusion: a comparison between liquid and solid polymer LiTFSI electrolytes. *Solid State Ionics*, 152-153:131–136, 2002. ISSN 01672738. doi: 10.1016/S0167-2738(02)00364-8.

[262] Y Aihara, S Arai, and K Hayamizu. Ionic conductivity, DSC and self diffusion coefficients of lithium, anion, polymer, and solvent of polymer gel electrolytes: the structure of the gels and the diffusion mechanism of the ions. *Electrochim. Acta*, 45 (8):1321–1326, 2000. ISSN 00134686. doi: 10.1016/S0013-4686(99)00339-4.

[263] CRA Catlow and GE Mills. Computer simulation of ionically conducting polymers. *Electrochim. Acta*, 40(13-14), 1995. ISSN 00134686. doi: 10.1016/0013-4686(95)00141-Z.

[264] GE Mills and C Richard A Catlow. Ionic clustering in polymer electrolytes. *J. Chem. Soc. Chem. Commun.*, (18):2037, 1994. ISSN 0022-4936. doi: 10.1039/c39940002037.

[265] VA Payne, M Forsyth, MA Ratner, DF Shriver, and SW De Leeuw. Highly concentrated salt-solutions - molecular-dynamics simulations of structure and transport. *J. Chem. Phys.*, 100(1994):5201–5210, 1994. ISSN 00219606. doi: 10.1063/1.467184.

[266] L Edman, MM Doeff, A Ferry, J Kerr, and LC Jonghe. Transport properties of the solid polymer electrolyte system P(EO)$_n$ LiTFSI. *J. Phys. Chem. B*, 104: 3476–3480, 2000. doi: 10.1021/jp993897z.

[267] S Feng, D Shi, F Liu, L Zheng, J Nie, W Feng, X Huang, M Armand, and Z Zhou. Single lithium-ion conducting polymer electrolytes based on poly (4-styrenesulfonyl)(trifluoromethanesulfonyl)imide anions. *Electrochimica Acta*, 93:254–263, 2013.

[268] Y Ma. The measurement of a complete set of transport properties for a concentrated solid polymer electrolyte solution. *J. Electrochem. Soc.*, 142(6): 1859–1868, 1995. ISSN 00134651. doi: 10.1149/1.2044206.

[269] A Ferry, MM Doeff, and LC De Jonghe. Transport property and raman spectroscopic studies of the polymer electrolyte system p(eo)$_n$-natfsi. *J. Electrochem. Soc.*, 145(5):1586–1592, 1998.

[270] MM Doeff and JS Reed. Li ion conductors based on laponite/poly(ethylene oxide) composites. *Solid State Ionics*, 113:109–115, 1998.

[271] DM Pesko, K Timachova, R Bhattacharya, MC Smith, I Villaluenga, J Newman, and NP Balsara. Negative transference numbers in poly (ethylene oxide)-based electrolytes. *Journal of The Electrochemical Society*, 164(11):E3569–E3575, 2017.

[272] D Devaux, R Bouchet, D Glé, and R Denoyel. Mechanism of ion transport in PEO/LiTFSI complexes: effect of temperature, molecular weight and end groups. *Solid State Ionics*, 227:119–127, 2012. ISSN 01672738. doi:

10.1016/j.ssi.2012.09.020.

[273] A Mellati, S Dai, J Bi, B Jin, and H Zhang. A biodegradable thermosensitive hydrogel with tuneable properties for mimicking three-dimensional microenvironments of stem cells. *Rsc Advances*, 4(109):63951–63961, 2014.

[274] DE Discher, P Janmey, and Y Wang. Tissue cells feel and respond to the stiffness of their substrate. *Science*, 310(5751):1139–1143, 2005.

[275] AK Yetisen, I Naydenova, F da Cruz Vasconcellos, J Blyth, and CR Lowe. Holographic sensors: three-dimensional analyte-sensitive nanostructures and their applications. *Chemical reviews*, 114(20):10654–10696, 2014.

A

The optimised potential for liquid simulation - all atom (OPLS-AA) force-field

The OPLS-AA force-field [127] was used to describe both the nitrile butadiene rubber (NBR) and hydrogenated nitrile butadiene rubber (HNBR) inter- and intra-molecular interactions [133]. Here the analytic formulation as well as the parameters used are reported.

Analytic form

The analytic formulation of the OPLS-AA force-field is reported in Equation A.1. The f_{ij} term is used to reduce the non-bonded interactions of atom i and j. If i and j are separated by one or two bonds $f_{ij} = 0$, by three bonds $f_{ij} = 1/2$ and for more than three $f_{ij} = 1$. The mixing rule for ε_{ij} and σ_{ij} is chosen to be geometric, i.e., $\varepsilon_{ij} = \sqrt{\varepsilon_{ii}\varepsilon_{jj}}$. The parameters used for NBR and HNBR are listed in Equation A.

$$
E = \left\{ \begin{aligned}
&\overbrace{\frac{1}{2}\sum_{\text{bonds}} k_b \left(r - r_0\right)^2}^{\text{Bond terms}} + \overbrace{\frac{1}{2}\sum_{\text{angles}} k_\theta \left(\theta - \theta_0\right)^2}^{\text{Angle terms}} + \\
&+ \overbrace{\frac{1}{2}\sum_{\text{dihedrals}} \sum_{n=1}^{4} K_n \left[1 - (-1)^n \cos(nz)\right]}^{\text{Dihedral terms}} + \\
&+ \overbrace{\sum_{i>j} \left\{ 4\varepsilon_{ij} \left[\left(\frac{\sigma_{ij}}{r_{ij}}\right)^{12} - \left(\frac{\sigma_{ij}}{r_{ij}}\right)^{6} \right] + \frac{q_i q_j e^2}{r_{ij}} \right\} f_{ij}}^{\text{LJ + Coulomb terms}} .
\end{aligned} \right. \tag{A.1}
$$

Element	Note	Type	Mass [g mol^{-1}]	σ [nm]	ε [kcal mol^{-1}]	q [e]
C (sp^3)	C in CH_3	CT	12.011	0.35	0.066	-0.18
C (sp^3)	C in CH_2	CT	12.011	0.35	0.066	-0.12
C (sp^3)	C in CH_2 next to CN	CT	12.011	0.33	0.066	-0.02
C (sp^3)	C in CH next to CN	CT	12.011	0.33	0.066	0.04
C (sp^2)	C in HC=CH	CM	12.011	0.355	0.076	-0.115
C (sp)	C in C≡N	CZ	12.011	0.33	0.066	0.46
N	N in C≡N	NZ	14.007	0.32	0.17	-0.56
H	H in $CH_{2,3}$	HC	1.008	0.25	0.03	0.06
H	H in HC=CH	HC	1.008	0.242	0.03	0.115
H	H in $CH_{1,2}$ next to CN	HC	1.008	0.25	0.015	0.06

Table A.0.1: OPLS-AA force-field atom types for NBR and HNBR

Bond	k_b [kcal mol^{-1} nm^{-2}]	r_0 [nm]
CT–CT	53 600	0.1529
CT–CM	63 400	0.151
CT–CZ	78 000	0.147
CT–HC	68 000	0.109
CM–CM	109 800	0.134
CM–HC	68 000	0.108
CZ–NZ	130 000	0.1157

Table A.0.2: OPLS-AA force-field bond types for NBR and HNBR

Angle	k_θ [kcal mol^{-1}]	θ_o [180/π]
CT–CT–CT	116.7	112.7
CT–CT–CM	126	111.1
CT–CT–CZ	116.7	112.7
CT–CT–HC	75	110.7
CT–CM–CM	140	124
CT–CZ–NZ	300	180
CT–CM–HC	70	117
CM–CT–HC	70	109.5
CM–CM–HC	70	120
CZ–CT–HC	70	108.5
HC–CT–HC	66	107.8

Table A.0.3: OPLS-AA force-field angle types for NBR and HNBR

Dihedral	K_1 [kcal mol^{-1}]	K_2 [kcal mol^{-1}]	K_3 [kcal mol^{-1}]	K_4 [kcal mol^{-1}]
CT-CM-CM-CT	0.0	14.0	0.0	0.0
CT-CM-CM-HC	0.0	14.0	0.0	0.0
CT-CT-CT-HC	-0.9	0.0	0.3	0.0
CT-CT-CT-CZ	0.0	0.0	0.0	0.0
CT-CT-CT-CT	0.7	-0.05	0.2	0.0
CM-CM-CT-HC	1.116	0.0	-0.372	0.0
CM-CT-CT-HC	-1.098	0.0	0.366	0.0
CM-CT-CT-CT	0.7	-0.05	0.2	0.0
CM-CM-CT-CT	3.058	0.405	-0.904	0.0
HC-CT-CM-HC	-0.954	0.0	0.318	0.0
HC-CM-CM-HC	0.0	14.0	0.0	0.0
HC-CM-CT-CT	0.0	0.0	0.0	0.0
HC-CT-CT-HC	-0.9	0.0	0.3	0.0
CT-CT-CZ-NZ	0.0	0.0	0.0	0.0
HC-CT-CT-CZ	-1.098	0.0	0.366	0.0
HC-CT-CZ-NZ	0.0	0.0	0.0	0.0
CZ-CT-CT-CM	0.0	0.0	0.0	0.0
CM-CT-CT-CM	0.0	0.0	0.0	0.0

Table A.0.4: OPLS-AA force-field dihedral types for NBR and HNBR

B

The PCFF+ functional form

Here the analytic formulation of the PCFF+ force-field is reported. In second-generation force-fields, the potential energy is split into three major contributions: bonded terms, cross-terms, and non-bonded terms. Bonded terms are shown in Equations B.1, B.2, B.3 and B.4 and they represents bonds, angles, dihedral and improper angles, respectively. Equations B.5, B.6, B.7, B.8, B.9 and B.10 are the cross-terms and include the interaction between bond stretching, bending and torsion. Finally, Equations B.11 and B.12

represent the Coulombic and van der Waals (vdW) energy, respectively.

$$E = \sum_{\text{bonds}} \left[k_{b_1}(r - r_0)^2 + k_{b_2}(r - r_0)^3 + k_{b_3}(r - r_0)^4\right] + \tag{B.1}$$

$$+ \sum_{\text{angles}} \left[k_{\theta_1}(\theta - \theta_0)^2 + k_{\theta_2}(\theta - \theta_0)^3 + k_{\theta_3}(\theta - \theta_0)^4\right] + \tag{B.2}$$

$$+ \sum_{\text{dihedrals}} \sum_{n=1}^{3} K_n \left[1 - \cos(n\varphi - \varphi_n^0)\right] + \tag{B.3}$$

$$+ \sum_{\text{improper}} K_x x^2 + \tag{B.4}$$

$$+ \sum_{\text{b}} \sum_{\text{b'}} F_{bb'}(r - r_0)(r' - r'_0) + \tag{B.5}$$

$$+ \sum_{\theta} \sum_{\theta'} F_{\theta\theta'}(\theta - \theta_0)(\theta' - \theta'_0) + \tag{B.6}$$

$$+ \sum \text{b} \sum_{\theta} F_{b\theta}(b - b_0)(\theta - \theta_0) + \tag{B.7}$$

$$+ \sum_{\text{b}} \sum_{\varphi} (b - b_0)\left[K_1 \cos(\varphi) + K_2 \cos(2\varphi) + K_3 \cos(3\varphi)\right] + \tag{B.8}$$

$$+ \sum_{\text{b'}} \sum_{\varphi} (b' - b'_0)\left[K_1 \cos(\varphi) + K_2 \cos(2\varphi) + K_3 \cos(3\varphi)\right] + \tag{B.9}$$

$$+ \sum_{\varphi} \sum_{\theta} \sum_{\theta'} K_{\varphi\theta\theta'} \cos(\varphi) \cos(\theta - \theta_0) \cos(\theta' - \theta'_0) + \tag{B.10}$$

$$+ \sum_{i>j} \frac{q_i q_j}{\varepsilon r_{ij}} + \tag{B.11}$$

$$+ \sum_{i>j} \left[\left(\frac{A_{ij}}{r_{ij}}\right)^9 - \left(\frac{B_{ij}}{r_{ij}}\right)^6\right]. \tag{B.12}$$

C

Additional persistence maps

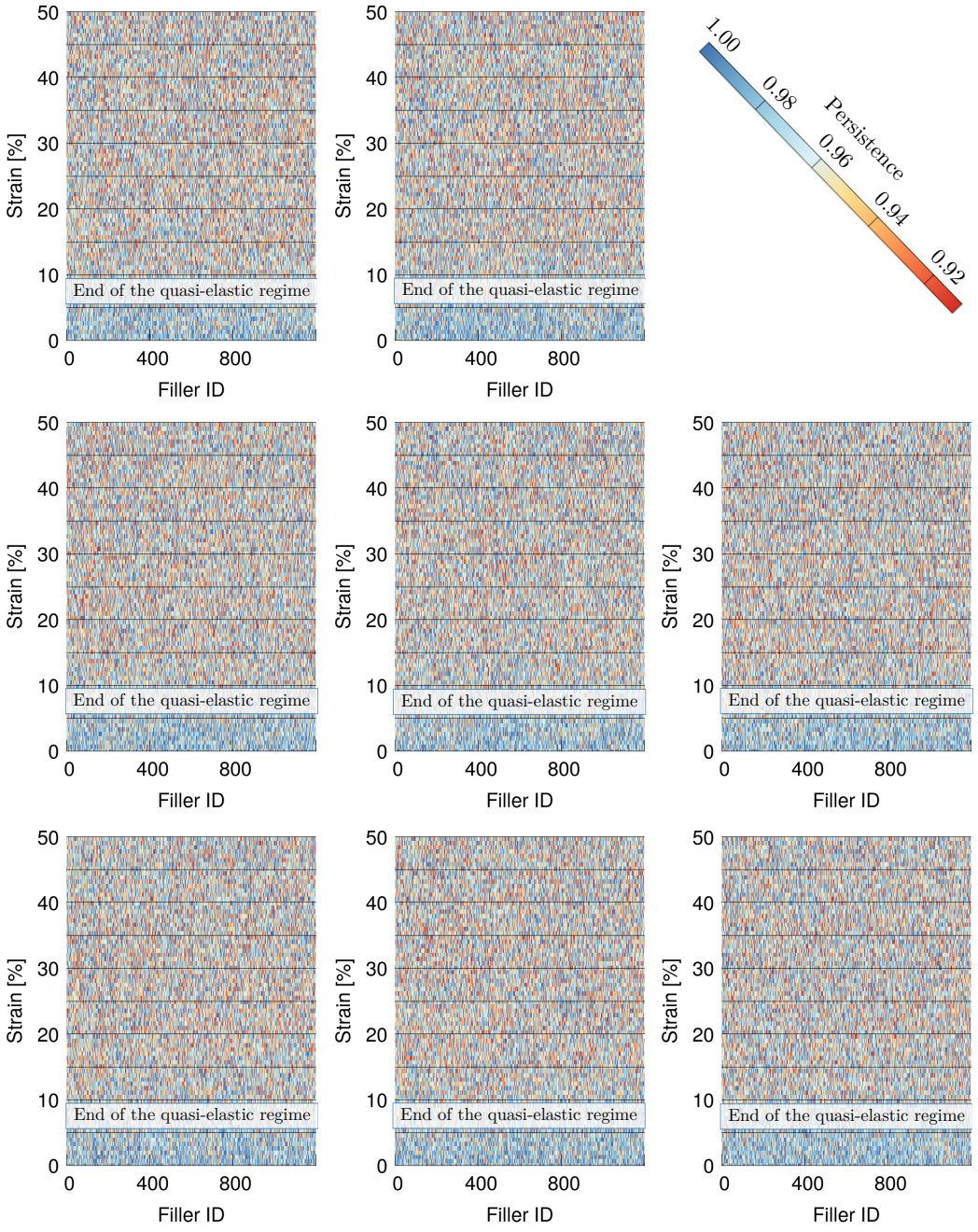
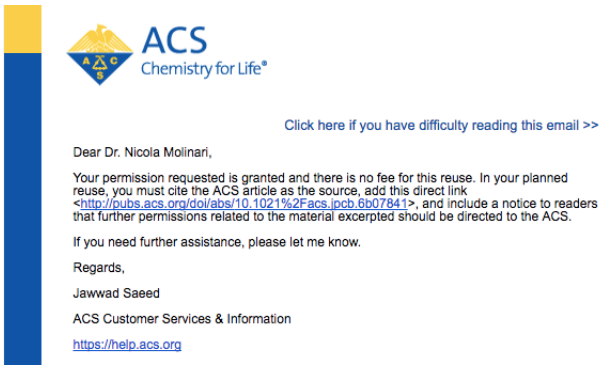


Figure C.0.1: Persistence of each of the 1200 fillers in all 47 % filler volume fraction (FVF) structures as a function of strain.

D

Re-use permissions

chapter 2. At the time of submission of the present dissertation, part of the content of this chapter constitute a publication in Journal of Physical Chemistry B, published by the American Chemical Society. The figures and text have been re-edited, nevertheless, the permission from the editor is shown in Figure D.0.1.


ACS Chemistry for Life®

Click here if you have difficulty reading this email >>

Dear Dr. Nicola Molinari,

Your permission requested is granted and there is no fee for this reuse. In your planned reuse, you must cite the ACS article as the source, add this direct link <http://pubs.acs.org/doi/abs/10.1021%2Facs.jpcb.6b07841>, and include a notice to readers that further permissions related to the material excerpted should be directed to the ACS.

If you need further assistance, please let me know.

Regards,

Jawwad Saeed

ACS Customer Services & Information

https://help.acs.org

Figure D.0.1: Publishing permission obtained from the American Chemical Society for chapter 2.

chapter 5. At the time of submission, this chapter was submitted for publication in Physical Chemistry and Chemical Physics, published by the Royal Society of Chemistry. From http://www.rsc.org [accessed: 2017-11-21]:
" **Author reusing their own work published by the Royal Society of Chemistry**
You do not need to request permission to reuse your own figures, diagrams, etc, that were originally published in a Royal Society of Chemistry publication. However, permission should be requested for use of the whole article or chapter except if reusing it in a thesis. If you are including an article or book chapter published by us in your thesis please ensure that your co-authors are aware of this."

Colophon

This thesis was typeset using LaTeX, originally developed by Leslie Lamport and based on Donald Knuth's TeX. The body text is set in 12 point Arno Pro, designed by Robert Slimbach in the style of book types from the Aldine Press in Venice, and issued by Adobe in 2007.